CHARACTERISATION OF THE CYCLIC SOFTENING PROPERTIES OF SOLDER

CHERYL SHARMANI SELVANAYAGAM

(B. Eng. (Hons.), NUS)

A THESIS SUBMITTED

FOR THE DEGREE OF MASTER OF ENGINEERING

DEPARTMENT OF MECHANICAL ENGINEERING

NATIONAL UNIVERSITY OF SINGAPORE

2011

ACKNOWLEDGEMENTS

First and foremost, I would like to thank my supervisor, Professor Victor Shim for the time and energy spent on supervising this work. His suggestions, insights and feedback have elevated the quality of this work and made me a better researcher and technical writer. I thank him, also, for the kind words of encouragement and patience throughout these four years.

I am grateful to Dr Wong Ee Hua and Simon Seah for introducing me to the issue of drop impact reliability of electronics. They have been valuable collaborators and I have learnt much from our technical discussions related to this work.

I would also like to thank the lab officers, Mr Alvin Goh and Mr Joe Low, and my fellow graduate students at Impact Mechanics Lab for their assistance and friendship.

Finally, I'd like to thank my family and friends who have been supportive throughout my graduate studies.

TABLE OF CONTENTS

Acknowledgements
Table of Contents
Summary
List of Tables
List of Figures
List of Symbols
Chapter 1: Introduction 1
1.1 Background 1
1.2 Objectives and Scope 2
1.3 Outline 3
Chapter 2: Literature Review 4
2.1 Drop Impact Testing 4
2.2 Computational Simulation of Drop Impact 6
2.3 Material Properties of Solder and Characterisation Methods 8
2.3.1 Strength and stiffness properties 8
2.3.2 Fatigue properties 11
Chapter 3: Materials and Methods 14
3.1 Introduction 14
3.2 Solder Alloys 14
3.2.1 Sample Preparation 15
3.2.2 Microstructure 17
3.3 Tests for Strength and Stiffness 18
3.3.1 Vickers Microhardness Test 18
3.3.2 Uniaxial Tension Tests 19
3.3.3 Uniaxial Compression Test 22
3.4 Fatigue testing 23
Chapter 4: Strength and Stiffness Properties 28
4.1 Introduction 28
4.2 Vickers Microhardness Test 28
4.2.1 Vickers Microhardness of Cast Ingots 29
4.2.2 Vickers Microhardness of Solder Joints 30

4.2.3 Comparison of Microhardness for Cast Ingots and Solder Joints........................... 31
4.3 Uniaxial tension tests... 32
4.3.1 True Stress-True Strain Curves 32
4.3.2 Material Properties Extracted from True Stress-True Strain Graphs...................... 34
4.4 Uniaxial compression tests 35
4.4.1 True Stress-True Strain Curves 35
4.4.2 Material Properties Extracted from True Stress-True Strain Graphs...................... 36
4.5 Comparison between Tensile and Compressive Data 37
4.6 Summary.. 37
Chapter 5: Fatigue Properties of Solder 39
5.1 Introduction... 39
5.2 General Characteristics of Cyclic Stress-strain Curves 39
5.2.1 Cyclic Softening of Solder 40
5.2.2 Effect of Test Conditions on Profile of Hysteresis Loops..................................... 41
5.3 The Bauschinger Effect 43
5.3.1 Comparison between β Determined at 0.2% and 0.4% Offset Yield Strength........ 45
5.3.2 Rate Dependence of β.. 46
5.3.3 Comparison of β for Different Solder Alloys... 47
5.4 S-N Curves.. 47
5.5 Summary.. 49
Chapter 6: Modelling of Fatigue Characteristics... 51
6.1 Introduction... 51
6.2 Theoretical Considerations in Implementing Hardening Behaviour in Abaqus 51
6.3 Modelling Methodology 52
6.4 Evaluation and Validation of Material Models 53
6.4.1 Determination of Isotropic Softening Material Constants Q and b 53
6.4.2 Determination of Kinematic Hardening Material Constants C_k and γ_k 54
6.4.3 Evaluation of Material Model 57
6.5 Modelling of Vibration of Printed Circuit Board.. 58
6.5.1 Details of Model 58
6.5.2 Results and Discussion... 60
Chapter 7: Conclusion 65
Bibliography... 67
Appendix A: Experimental Cyclic Stress-Strain Curves 71
Appendix B: Comparison between Experimental Stress-Strain Curves and FEM Simulation Results 78

SUMMARY

Drop impact failure of solder joints in portable electronic products is a concern for many manufacturers. Tests for evaluating the drop impact reliability are time-consuming and tedious to carry out. Failure during these tests means the entire design cycle needs to be repeated. A more efficient design process for portable electronics products would incorporate finite element modeling to optimize the design in terms of accommodating drop impacts without failure, so that fewer design cycles are necessary for a certain product. Reliable finite element modeling requires accurate material properties to be specified in simulations.

Failure during drop impact has been attributed to differential flexing between the die and board, induced by the impact pulse. In accommodating this differential flexing, the solder undergoes fatigue at a medium strain rate. Solder material exhibits strain softening under cyclic loading and hence, this behaviour needs to be incorporated into finite element modelling to correctly simulate the response of solder interconnections under impact-induced vibration.

The primary objective of this study is to characterise the cyclic softening behaviour of electronic solder through a series of fatigue tests, and then to implement these material properties of solder into a finite element model.

Three solder alloys – SAC305, Sn100C and eutectic SnPb were selected for this study. Special attention was paid to sample preparation to ensure similarity of microstructure between the solder specimens and solder joints.

Uniaxial tension and compression tests were conducted to evaluate the Young's modulus and yield strength of the materials. The tensile and compressive material properties were found to be similar. SAC305 is the stiffest alloy in terms of microhardness, Young's modulus and flow stress; Sn100C and SnPb are generally softer, with SnPb having the lowest microhardness and Young's modulus. Sn100C has the lowest yield strength and flow stress.

Characterization of fatigue properties was carried out at three strain amplitudes and two strain rates. Peak stresses in solder decrease gradually initially, then more sharply once a crack is initiated. It was found that the solder materials studied undergo isotropic softening and kinematic hardening. Both lead-free and eutectic tin-lead solders exhibit cyclic softening, while strain hardening in lead-free solder is more pronounced than that in SnPb solder.

The S-N curves of the solder alloys indicate a longer fatigue life, in terms of number of cycles to failure, for higher strain rates. However, with regard to time to failure, samples loaded at lower strain rates last longer. Sn100C has the longest life, followed by SAC305 and SnPb, for both strain rates examined.

Cyclic stress-strain curves were further analysed to extract isotropic softening and kinematic hardening material parameters. The use of these parameters was demonstrated via simulations of solder joints in a vibrating board, and a comparison of elastic-plastic and elastic-cyclic-softening material properties undertaken. A significant difference in stress values, ranging from 15-30%, for results based on the two different material models was observed, indicating that the cyclic softening behaviour of solder is significant and should be taken into account in finite element modelling of solder joints.

LIST OF TABLES

Table 2.1 Melting points and homologous temperatures of various solders 9

Table 2.2 Stiffness and strength of eutectic tin-lead solder and SAC305 [19] 10

Table 2.3 Summary of strength and stiffness data available for solder 10

Table 2.4 Summary of fatigue test data on solder available (α & θ are constants from Eq. 2.6) 13

Table 3.1 Manufacturers of solder bars used 15

Table 3.2 Mould and water temperatures used for casting (Assuming t = 2s) 16

Table 3.3 Test Matrix for Microhardness Tests 19

Table 3.4 Test Matrix for Uniaxial Tension Tests 21

Table 3.5 Test Matrix for Uniaxial Compressive Test 23

Table 3.6 Test matrix for fatigue tests 24

Table 3.7 Percentage non-uniformity of stress in the gauge length for various sample dimensions 25

Table 3.8 Material properties of SAC305 used in FEM modelling 25

Table 4.1 Percentage difference in microhardness between the cast ingot and solder joint for each solder alloy 32

Table 4.2 Young’s modulus of SAC305, SnPb & Sn100C, obtained from uniaxial tension tests 34

Table 4.3 Offset Yield Strength of SAC305, SnPb & SN100C, obtained from uniaxial tension tests 34

Table 4.4 Flow Stress of SAC305, SnPb & SN100C, obtained from uniaxial tension tests 35

Table 4.5 Young’s modulus of SAC305, SnPb & Sn100C, obtained from uniaxial compression tests 36

Table 4.6 Offset Yield Strength of SAC305, SnPb & Sn100C, obtained from uniaxial compression tests 36

Table 4.7 Flow Stress of SAC305, SnPb & Sn100C, obtained from uniaxial compression tests 36

Table 4.8 Comparison of tensile and compressive material properties 37

Table 4.9 Solder alloys ranked from highest (1) to lowest (3) for each material property 38

Table 5.1 Comparison of slopes and R-squared values for β vs strain in SnPb and SAC305 46

Table 5.2 Coffin-Manson constants for SnPb and SAC305 49

Table 6.1 Values of Q and b for various solder alloys and test conditions 54

Table 6.2 Values for C_k and γ_k for various solder alloys and test conditions 57

Table 6.3 Dimensions of components in finite element model 60

Table 6.4 Properties for each material model used for SAC305 60

Table 6.5 Stress components (MPa) from simulations based on three material models. Percentage difference between values based on elastic-plastic behaviour and elastic-cyclic-softening material properties are also listed 63

LIST OF FIGURES

Figure 2.1 Schematic diagram of JEDEC drop test setup 5

Figure 3.1 Fine microstructure of SAC305 solder ball 15

Figure 3.2 Solder in its various forms – (a) Solder bars (b) Cast ingots 16

Figure 3.3 Microstructure of SAC305 using (a) Casting Parameters A, (b) Casting Parameters B and (c) Casting Parameters C at the same scale 17

Figure 3.4 Microstructure of (a) SAC305, (b) SAC305 solder joint (c) SnPb (d) SnPb solder joint and (e) Sn100C at the same scale 18

Figure 3.5 Tensile test setup 20

Figure 3.6 True stress-true strain curves of SAC305, with and without strain gauges, from extensometer measurements 21

Figure 3.7 Compression Test Setup 23

Figure 3.8 Uniform stress in gauge section of test sample 26

Figure 3.9 Machined dog-bone samples 26

Figure 3.10 (a) Raw strain data with erroneous increasing mean strain; (b) Corrected strain data 27

Figure 3.11 Optical micrographs showing damage in strain gauges 27

Figure 4.1 Average microhardness and standard deviation from ten indentations on SAC305, SnPb and Sn100C in cast ingot form 29

Figure 4.2 Microindentation on cast ingot of solder alloy (a) SAC305, (b) Sn100C and (c) SnPb at the same scale 30

Figure 4.3 Average microhardness and standard deviation from ten indentations on SAC305, SnPb and SAC101 in solder joint form 30

Figure 4.4 Microindentation on solder joints of (a) SAC305, (b) SAC101 and (c) SnPb at the same scale 31

Figure 4.5 Average microhardness and standard deviation from ten indentations on SAC and SnPb in cast ingot and solder joint form, Sn100C in cast ingot form and SAC101 in solder joint form 32

Figure 4.6 True stress-strain curves for SAC305, SnPb & Sn100C, obtained from uniaxial tension tests 33

Figure 4.7 Scanning electron micrograph of fracture surfaces of (a) SAC305 (b) Sn100C (c) SnPb at the same scale 33

Figure 4.8 True stress-strain curves for SAC305, SnPb & SN100C, obtained from uniaxial compression tests 35

Figure 5.1 (a) Stress-strain curves for SnPb at strain rate of 0.27/s and strain of 0.027 (b) Stress-strain curves for SAC305 at strain rate of 0.14/s and strain of 0.02 40

Figure 5.2 Variation of Stress with Logarithm of Number of Cycles for SAC305 41

Figure 5.3 Initial stress-strain cycles for SnPb and SAC305 at strain rate of 0.01 /s 42

Figure 5.4 Initial stress-strain cycles for SnPb and SAC305 at strain of 0.02 42

Figure 5.5 Stress-strain curve depicting the Bauschinger effect, where the yield strength in compression is smaller than that in tension 44

Figure 5.6 Variation of β with strain for SnPb and SAC305, corresponding to yield points determined at 0.2% and 0.4% offset 45

Figure 5.7 Variation of β with strain at two strain rates, for SnPb and SAC305 46

Figure 5.8 Variation of β with strain amplitude imposed for three solder alloys at two strain rates 47

Figure 5.9 Plot of strain amplitude imposed against logarithm of number of cycles at failure, showing that failure defined by the 'knee' occurs sooner than that defined by a 25% decrease in stress 48

Figure 5.10 S-N curves for three solder alloys tested at two strain rates – 0.01/s and 0.1/s 48

Figure 6.1 Flow chart of modelling methodology to determine material constants and assess improvement in accuracy with hardening properties incorporated 53

Figure 6.2 Curve-fitting to determine constants Q and b 54

Figure 6.3 (a) First cycle and half cycle of stable hysteresis loop (b) Half cycle and offset half cycle at yield point of 30 MPa (c) Offset half cycles at yield points of 20, 30 and 40 MPa 56

Figure 6.4 Single beam element model for determination of material model parameters 56

Figure 6.5 Comparison of experimental stress-strain curves with simulations 57

Figure 6.6 Comparison of experimental stress-strain curves with simulations for selected loading cycles 58

Figure 6.7 (a) Finite element model of quarter of printed circuit board with component (b) Magnified view of component, showing solder joints (c) Submodel of critical corner joint 59

Figure 6.8 Boundary and loading conditions applied to model with d=0.3mm and ω=188.5 rad/s 60

Figure 6.9 Board strain near critical joint, from simulation 61

Figure 6.10 von Mises stress in models with elastic-plastic material properties - (a) solder joints of global model and (b) submodel of the critical joint.. 62

Figure 6.11 von Mises stress in models based on elastic-cyclic-softening material properties - (a) solder joints of global model and (b) submodel of the critical joint. 62

Figure 6.12 Evolution of peeling stress with time and loading cycles for models with elastic-perfectly-plastic and elastic-strain-hardening material properties 63

LIST OF SYMBOLS

A_i instantaneous area

A_o original cross-sectional area of the gauge length

B material constant associated with isotropic softening model

C_k material constant associated with kinematic hardening model

D_f Number of drops to failure

E Young's Modulus

F applied force

I_Z second moment of area of the cross-section about the z-axis

L_e equivalent length of the column

L_i instantaneous gauge length

L_o original gauge length

ΔL extension of the sample

N number of backstresses

P axial force on column

Q material constant associated with isotropic softening model

T thickness of column

t_c time taken for heat to dissipate from molten solder

W width of column

α_k k^{th} backstress

β scalar parameter defining the extent of kinematic hardening

ε engineering strain

$\dot{\varepsilon}$ strain rate

ε_{pl} plastic strain

ε_i instantaneous strain

γ_k material constant associated with kinematic hardening model

σ engineering stress

σ_f maximum flow stress in tension

σ_o initial yield stress

σ_i instantaneous stress

σ_{y1} yield stress in tension

σ_{y2} yield stress in compression

Chapter 1
INTRODUCTION

1.1 BACKGROUND

Drop impact failure of solder joints in portable electronic products is a concern for many manufacturers. This is largely due to two reasons - miniaturization of portable electronic products, which inevitably results in miniaturization of the solder joints in these products and the introduction of the Restriction of Hazardous Substances (RoHS) legislative calling for the use of lead-free solder. Smaller joints are more susceptible to failure as cracks need to propagate through a smaller length for complete failure of the joint. Lead-free solder joints are less robust than eutectic tin-lead ones. Tin-based lead-free solder joints form the intermetallic compound (IMC) Cu_6Sn_5, which is brittle at the strain rates experienced by joints during drop impact [1].

Although there are test standards available for evaluating the drop impact reliability of printed circuit boards (PCB), these are time-consuming and tedious to carry out. Failure during these tests means the entire design cycle needs to be repeated. A more efficient design process for portable electronics products would incorporate finite element modeling to optimize the design in terms of accommodating drop impacts without failure, so that fewer design cycles are necessary for a certain product. Reliable finite element modeling requires accurate material properties to be

specified in simulations. Such data may have been available with eutectic tin-lead solder. Lead-free solder, being relatively new, has not yet been thoroughly characterized.

Failure during drop impact has been attributed to differential flexing between the die and board, induced by the impact pulse. In accommodating this differential flexing, the solder undergoes fatigue at a medium strain rate (1/s to 50/s). Solder material exhibits strain softening under cyclic loading. A material is said to undergo strain softening if the stress in it reduces as the plastic strain increases. This behaviour needs to be incorporated into finite element modelling to correctly simulate the response of solder interconnections under impact-induced vibration.

1.2 OBJECTIVES AND SCOPE

The primary objective of this study is to characterise the cyclic softening behaviour of electronic solder through a series of fatigue tests, and then to implement these material properties of solder into a finite element model.

Three solder alloys – SnAg3.0Cu0.5 (SAC305), SnCu0.7Ni0.05+Ge (Sn100C) and eutectic SnPb were selected for this study. As the microstructure in solder joints can be vastly different from that in bulk solder bars, special attention was paid to sample preparation to ensure similarity of microstructure between the solder specimens and solder joints. This was verified via microhardness tests. In addition, uniaxial tension and compression tests were also conducted to evaluate the Young's modulus and yield strength of the materials.

Fatigue characterisation was carried out at three strain amplitudes (0.01, 0.015, 0.02) and two strain rates (0.01, 0.1/s). Isotropic softening and kinematic hardening material parameters were then extracted from the resulting cyclic stress-strain curves. These material parameters were used in finite element modelling for estimation of stresses. This is demonstrated by simulation of a printed circuit board subjected to vibration at 30Hz, whereby the solder joint material was modelled using the stress-softening model parameters.

1.3 OUTLINE

This report consists of seven chapters. Chapter 2 presents a literature review on trends in drop impact testing and simulation. Material properties of solder determined through various characterisation methods are also explored. Chapter 3 outlines the details of various characterisation tests that have been conducted. This includes descriptions of the tests, experimental setup, as well as sample design and preparation. Chapter 4 presents the results obtained from microhardness, uniaxial tension and compression tests. The Young's modulus, yield strength and flow stress, extracted from the stress-strain curves, are compared with values from literature. The following chapter presents cyclic stress-strain curves obtained from fatigue characterisation tests. Chapter 6 outlines the method by which isotropic softening and kinematic hardening material parameters are extracted from experimental cyclic stress-strain curves. These material parameters are also incorporated into the simulation of a vibrating board.

Chapter 2

LITERATURE REVIEW

This review first considers various methods to test and assess the drop impact reliability of boards and how these tests are modeled using finite element analysis. The material properties used in these models and methods to characterise them are also reviewed.

2.1 DROP IMPACT TESTING

With the increase in usage of portable electronics devices such as mobile phones, digital cameras and personal digital assistants (PDAs), failure of such devices through accidental drop impact has become more prevalent than the failure of solder joints from temperature cycling. To reduce the occurrence of failure from impact, drop impact testing is carried out at various levels – at product level, board level and even at chip level. The following section focuses on board-level drop tests.

Board-level testing is carried out on printed circuit boards (PCBs) without any product casing surrounding it. Consider a PCB that is mounted onto a plastic product casing via screws located at different positions; upon drop impact, failure occurs as a result of the impact force generating differential flexing between the board and the chip [2, 3]. It is possible that board-level drop impact testing can replicate this failure mode and provide an estimate of the component lifetime

that is generally obtained through product level testing. The main difference board and product level testing is the effect of product orientation at impact and the possibility of multiple impacts from product drop tests.

The most common method of board level testing follows the Joint Electonic Device Engineering Council (JEDEC) standard JESD22-B111[4]. This standard specifies the test board dimensions, layout and location of components. The experimental setup consists of a drop tower with a special base plate for mounting the board (Fig 2.1); the board is attached to the base plate standoffs using 4 screws – one at each corner of the board. The base plate is then raised to a predetermined height and released to fall freely, such that the resulting shock pulse on the component induces a peak acceleration of 1500g and pulse width of 0.5ms.

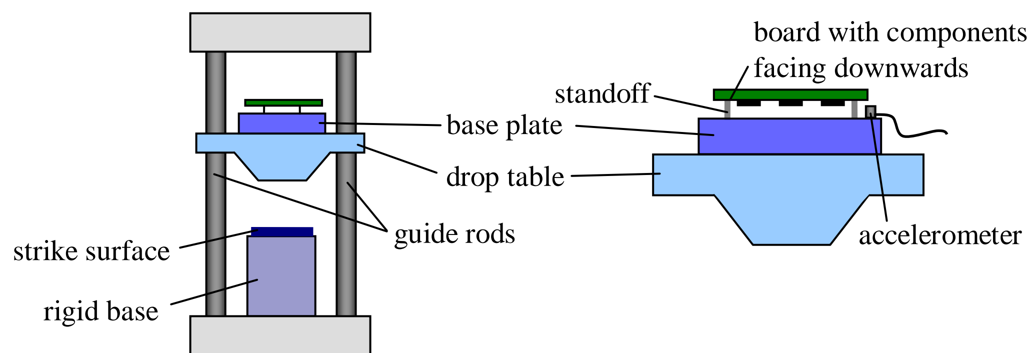

Figure 2.1 Schematic diagram of JEDEC drop test setup

Although widely used, there are several drawbacks with the JEDEC test. Firstly, it is time-consuming; each board has to be individually mounted and tested to a maximum of 30 drops. There has also been some criticism that the test does not correlate well with product-level drop tests for several reasons. These include the variable orientation of product-level test samples at impact, strain responses of the board that vary from one test to another and different mounting locations of the boards. Poor reproducibility is also a concern, as it is difficult to generate a clean half sine pulse [3].

Several researchers have looked into different methods of board-level drop-impact testing [5]. Instead of dropping the board onto a hard surface to induce flexure, some of these methods utilise an impactor which induces bending of the boards[6, 7] while Seah et al. [8] developed a tester to apply high frequency sinusoidal cyclic bending directly to the board. Vibration testing of boards at the lowest natural frequncy was also found to reproduce failure modes found in drop testing [9]. This is because during drop tests, printed circuit boards flex at their lowest natural frequencies, which can be induced by vibration testing. Another approach is the use of a 'self-cancelling' pulse, through careful selection of the pulse width to match the natural frequency of the system. This results in a single cycle of flexure in the board, after which the pulse dies down [10].

2.2 COMPUTATIONAL SIMULATION OF DROP IMPACT

Several methods have been used to simulate drop impact - free-fall of a drop table, the input-G method and excitation of sample supports. Of these three methods, the free-fall of a drop table is the most tedious. It requires the entire test setup up to be modeled, so that the drop table falling under gravity induces flexure of the board. When the input acceleration pulse is not known, this method is necessary to model drop testing.

The input-G method was first carried out by Tee et. al. [11-13]. As the name suggests, this method involves application of a measured acceleration pulse, or G-level, to the mounting holes of the board. None of the other supporting structures such as the standoffs or the drop table need to be modelled. This greatly reduces computational time.

The final method, the support excitation scheme, was developed by Yeh and Lai [14, 15]. Like the input-G method, it involves modelling only the test board. Instead of applying an acceleration pulse, body forces are applied to the board. The body force is the mass matrix of the board multiplied by the acceleration pulse.

Drop impact modelling is generally undertaken for the purpose of life prediction [16]. This is done by carrying out drop impact experiments, then correlating a certain parameter from the modelling results, such as accumulated plastic strain or plastic work, to the number of drops to failure. The results are then curve-fitted to obtain the constants of a power law

$$D_f = A(\varepsilon_{pl})^B \quad \textbf{(2.1)}$$

where D_f is the number of drops to failure, ε_{pl} the plastic strain and A and B are material constants.

Although predicted values can be within two times that of experimental data, the main shortcoming of this approach is that it can only be applied to solder materials which fail in the bulk. Luan et. al. [11] used a similar approach for bulk solder failures. For failure through the intermetallic compound (IMC), a stress-based criterion is used, whereby the accumulated plastic strain in Eq. (2.1) is replaced by peeling stress.

Other researchers have considered aspects of drop impact, such as strain-rate dependence [17] and hardening of solder [18], to predict the effects of these parameters. For example, using assumed values for the rate-dependent properties of solder, Luan et. al. [17] was able to conclude that rate dependence is more important for softer solders such as tin-lead, than hard SAC405 solders. Under high strain rates, SAC405 becomes stronger and exhibits greater elasticity before yielding. Yeh et. al. [18] compared the assumption of isotropic and kinematic hardening properties. With kinematic hardening, the yield surface translates in the direction of the applied force. As a result, with repetitive drop impacts, the maximum and residual stresses remain relatively constant, while plastic strains and plastic strain energies increase linearly. On the other hand, in isotropic hardening, the yield surface expands, and the maximum stress increases with the number of drops. The incremental plastic strain energy decreases.

The simulation results described highlight the importance of strain rate dependence and cyclic hardening of solder properties in drop impact modelling. These properties need to be

characterized through experiments, so that they can be used in drop impact modelling to improve the accuracy of results. The following section summarises the material properties of solder available from literature and characterization methods used to obtain them.

2.3 Material Properties of Solder and Characterisation Methods

As solder joints are generally small and non-prismatic, with diameters ranging from 300μm to 500μm, it is difficult to characterize their mechanical properties directly. Although some researchers have chosen to characterize the constitutive properties of solder at the joint-level, the majority have adopted the approach of testing bulk solder instead. The following section focuses on material properties obtained from bulk samples.

2.3.1 Strength and stiffness properties

Uniaxial testing of bulk solders of various compositions has been carried by many researchers to determine the Young's modulus, yield stress, ultimate tensile stress and elongation [19-22]. Many of these tests have been performed at various strain rates and temperatures [22]. In general, it has been found that solder strength is smaller at low strain rates and high temperatures. This sensitivity is most obvious for SnPb [22]; studies at relatively low strain rates (10^{-5} to 10^{-1}/s) have been carried out to characterize the creep behavior of solder. This is because of the high homologous temperature of solder, which causes creep during reliability tests involving temperature cycling, whereby a package sample is subjected to repeated cycles of extreme temperature ranging from 125˚C down to -40˚C. The homologous temperature is defined by

$$T_h = \frac{T}{T_m} \tag{2.2}$$

where T_h is the homologous temperature, T the temperature in Kelvin and T_m the melting point in Kelvin. Table 2.1 shows the melting points and homologous temperatures of various solders.

Table 2.1 Melting points and homologous temperatures of various solders

Solder	Melting Point (°C)	Homologous Temperature at 25°C
63Sn37Pb	183	0.65
Sn-3.0Ag0.5Cu	217	0.61
Sn-3.5Ag	221	0.60
Sn-0.7Cu	227	0.60

Tests at higher strain rates have also been carried out on solder [23-25]. The main aim has been to provide strain rate dependant properties for drop impact modeling. Siviour et. al. [24] performed experiments using a Split Hopkinson Pressure Bar (SHPB) setup with the aim of obtaining reliable high strain rate compressive mechanical data for use in finite element work. Besides the effect of strain rate on five types of solder (63Sn37Pb, Sn3.8Ag0.7Cu, Sn3.0Ag0.5Cu, Castin, Sn3.5Ag), they also investigated the effects of temperature and aging. Like Plumbridge et. al. [20], they showed that SnPb is more sensitive to strain rate compared to lead-free solders. The SHPB setup has also been modified to measure the tensile properties of solder at similar strain rates [23].

It is noted that the strain rates tested by Siviour et. al., ranging from 450/s to 2720/s, are now known to be far larger than what is experienced by a solder joint during drop impact, which induces strain rates from 1/s to 50/s [25]. This range of strain rates was determined through finite element analysis of a circuit board undergoing drop testing. The range of strain rates in drop impact has been characterized by Wong et. al [25]. They used a drop tower instrumented with a load cell to determine the mechanical properties of four solder materials - 63Sn37Pb, 96.5Sn3.0Ag0.5Cu, 96.5Sn3.5Ag and 98.9Sn1.0Ag0.1Cu, over the range of 50/s to 300/s. An

Instron microtester was then used to characterize the same materials at strain rates of 0.005/s to 12/s. They found that the flow stress can be related to strain rate through a power law

$$\sigma_f = A\dot{\varepsilon}^B \tag{2.3}$$

where σ_f is the flow stress, $\dot{\varepsilon}$ the strain rate, A a constant and B the rate sensitivity index. In addition, the rate sensitivity index is insensitive to the value of flow stress, resulting in:

$$\frac{\sigma_{f2}}{\sigma_{f1}} = \left(\frac{\dot{\varepsilon}_2}{\dot{\varepsilon}_1}\right)^B \tag{2.4}$$

Table 2.2 Stiffness and strength of eutectic tin-lead solder and SAC305 [19]

Material	Young's modulus (GPa)	0.2% offset yield strength (MPa)	Ultimate tensile strength (MPa)
63Sn37Pb	16-36	27-41	26-47
Sn-3.0Ag0.5Cu	40-50	25-35	35-45

Table 2.3 Summary of strength and stiffness data available for solder

Material	Test type	Test Machine	Temperature (°C)	Strain rate (s^{-1})
63Sn37Pb, Sn-3.5Ag Sn-0.5Cu [20]	Tensile	Instron Servohydraulic tester	-10 – 75	10^{-3}-10^{-1}
63Sn37Pb, Sn-3.5Ag, Sn-3.0Ag0.5Cu, Sn-3.8Ag0.7Cu, Castin [24]	Compressive	Split Hopkinson Pressure Bar	-40 – 60	500-3000
63Sn37Pb, Sn-3.5Ag, Sn-3.0Ag0.5Cu, Sn-1.0Ag0.1Cu [25]	Compressive	Instrumented drop tower & Instron microtester	25	0.005-300

2.3.2 Fatigue properties

There is considerable literature on the low cycle fatigue (LCF) properties of solder available, especially for eutectic tin-lead solder at low strain rates [26-30]. As a result of the low homologous temperature of solder, failure during temperature cycling has been found to be due to creep. The most comprehensive investigation has been carried out by Kanchanomai et. al [28, 31-33], whose aim was to understand thermomechanical fatigue by first studying isothermal fatigue. As the knife-edge of extensometers was found to cause premature failure of samples, the authors developed an experimental setup that employed a non-contact digital image measurement system. Using this setup, they characterized the low cycle fatigue behaviour of SnPb as a function of different plastic strain ranges and strain rates. Other solder alloys such as Sn96.5Ag3.5, Sn63Pb37, Pb95Sn5 were also studied. Fatigue life was defined as number of cycles corresponding to a 25% reduction of the maximum nominal stress, which is in line with the Society of Material Science, Japan (JSMS) standard for low cycle fatigue testing of solder materials. The American Society for Testing and Materials (ASTM) standard for strain controlled fatigue testing [34], which defines failure as a 50% reduction in maximum tensile load, cannot be used in this case, as solder is much softer than other metals. In solders, fatigue life based on 50% reduction in maximum tensile load is beyond the onset of acceleration of softening. They found that the data could be fitted by:

$$\Delta\sigma = A(\Delta\varepsilon_P)^{\beta} \tag{2.5}$$

where $\Delta\sigma$ is the stress range at half the fatigue life, $\Delta\varepsilon_P$ is the apparent plastic strain range obtained from the width of the hysteresis loop at zero stress, A is the cyclic strength coefficient, and β is the cyclic strain-hardening exponent. Some studies [35, 36] have found that LCF behavior follows the Coffin–Manson equation (Eq. 2.6) with a fatigue ductility exponent of 0.63.

$$\Delta\varepsilon_P N^{\alpha} = \theta \tag{2.6}$$

where N is the fatigue life (number of cycles to 50% decrease in load), α the fatigue ductility exponent, and θ the fatigue ductility coefficient.

Several other researchers [37-41] have studied various compositions of solder; these range from Kariya and Otsuka's work [38] on small percentages of certain elements such as bismuth, copper, zinc and indium in Sn-3.5Ag to Pang's low copper tin solder. They found that for a fatigue life similar to that of SnPb, the Bi content should be 2% or less, and the In content should be 5%. Although they managed to find certain changes in fatigue life associated with the presence of different elements, all of their tests were performed at relatively low strain rates.

Bonnaud et. al. [42] carried out similar tests with a different motivation. They noted that solder joints undergo cyclic loading when boards flex on drop impact. As a result, their tests were conducted at a higher strain rate of 1/s, which was determined from simulations, and a plastic strain range of ±0.01. Cyclic test results showed a mix of isotropic and kinematic hardening between the 1st and 2nd cycles, and softening for subsequent cycles. A cyclic loading material model should thus comprise a combination of two isotropic hardening rules (to take into account hardening and softening behaviour) and one kinematic hardening rule

A summary of fatigue data available is shown in Table 2.4; from this, it is clear that the focus of many researchers has been low cycle fatigue at creep strain rates, as this data is required to model thermomechanical fatigue that occurs during temperature cycling tests. During drop impact however, cyclic softening of solder joints is known to occur, and this takes place at higher strain rates, of $0.1s^{-1}$ to $10s^{-1}$.

Table 2.4 Summary of fatigue test data on solder available (α & θ are constants from Eq. 2.6)

Material	Strain (%)	Frequency (Hz)	Strain rate (s^{-1})	Comments
96.5Sn-3.5Ag 63Sn-37Pb 5Sn-95Pb [28]	0.5-2	0.1	0.002-0.008	Temperature range: 20 – 120°C At 20°C, 0.1Hz: 96.5Sn-3.5Ag α =0.70, θ =3.17 63Sn-37Pb α =0.54, θ =0.47 5Sn-95Pb α =0.84, θ =9.13
Sn-3.5Ag-Bi (2, 5, 10%) Sn-3.5Ag-Cu (1, 2%) Sn-3.5Ag-Zn (1, 2%) Sn-3.5Ag-In (2, 5%) 63Sn-37Pb [38]	0.3-3.5	0.0357- 0.42	0.005	At 20°C, 0.005s^{-1}: Sn-3.5Ag α =0.5, θ =0.9 Sn-3.5Ag-1Cu α =0.43, θ =0.45
63Sn-37Pb [39]	1 - 50	10^{-4} - 1		Temperature range: -40 – 150°C At 25°C, 1Hz α =0.86, θ =3.44
95.5Sn-3.8Ag-0.7Cu [40]	2-7.5	0.001-1	0.00008-0.3	Temperature range: -40 – 125°C At 25°C, 1Hz α =0.913, θ =26.3
99.3Sn-0.7Cu [39]	2-7.5	0.001-1		Temperature range: 25 – 125°C At 25°C, 1Hz α =0.973, θ =21.3
Lead-free solder (not specified) [42]	1	25	1	

Chapter 3

MATERIALS AND METHODS

3.1 INTRODUCTION

Characterisation of the fatigue properties of solder materials through cyclic uniaxial testing is the main focus of this work. However, besides this, several other experiments – uniaxial tension, compression and microhardness tests were also conducted to evaluate the Young's modulus, yield strength and microhardness of the materials. Much attention was paid to sample preparation to ensure that the microstructures of the samples tested were similar to that in typical solder joints.

The following section outlines the solder alloys selected for characterisation and the method of sample preparation. A detailed description of the test sample geometry, test setup and procedure for each of the four types of experiments carried out is also provided.

3.2 SOLDER ALLOYS

From the numerous lead-free solders available commercially as well as those being developed through research, two materials were selected. The first was Sn-3.0Ag-0.5Cu, otherwise known as SAC305. This material has been widely accepted as the lead-free replacement for eutectic tin-lead solder. The second was Sn100C, developed by Nihon Superior. This material is composed of

tin, copper and trace amounts of nickel and germanium, and was part of a research batch produced by the company. Finally, eutectic tin-lead solder was also tested for comparison with the lead-free solders. Solder bars made from the different alloys were purchased from several manufacturers, as shown in Table 3.1.

Table 3.1 Manufacturers of solder bars used

Solder	Composition	Manufacturer
Eutectic tin-lead	63Sn-37Pb	Asahi
SAC305	Sn-3.0Ag-0.5Cu	Kester
Sn100C	Sn-0.7Cu-0.05Ni-Ge	Nihon Superior

3.2.1 Sample Preparation

The diameters of commercially-available solder balls generally range between 300 to 1270 μm. As a result of their small size and therefore volume, the cooling rate in a solder joint during the cooling phase of a reflow cycle is relatively fast, in the range of 0.5 – 1.5 °C/s [43]. This results in the fine microstructure found in solder joints. Fig 3.1 shows the fine microstructure in a SAC305 alloy solder joint. If the material properties of a solder joint are determined using bulk solder samples (machined from solder bars), appropriate sample preparation needs to be carried out, so that the resulting microstructure is similar to that of the solder joint [19, 44]. In this work, all samples were carefully prepared through the re-melting of solder bars, followed by casting, then quenching, in order to achieve this.

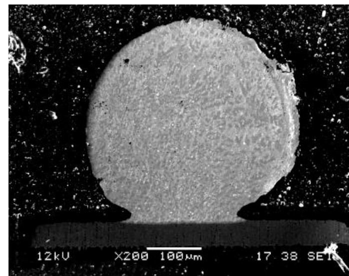

Figure 3.1 Fine microstructure of SAC305 solder ball

The procedure for sample preparation is as follows: first, the solder bar, as shown in Fig 3.2(a), is melted in a solder pot maintained at a temperature 150°C above the melting point. The molten solder is then poured into a heated stainless steel mould which is at a temperature, T_{mould}. The mould is then quenched in water at a temperature, T_{water} , of about 4°C. Once cooled, the cast ingot, shown in Fig 3.2(b), is then removed from the mould. Assuming that the heat from the molten solder takes a duration of t_c to be dissipated by the water, the approximate cooling rate can be estimated from $\frac{T_{mould}-T_{water}}{t_c}$. Three sets of mould and water temperatures were used, in order to determine the most suitable method of sample preparation. The temperatures of the mould and water, and the associated approximate cooling rates, are shown in Table 3.2. The estimated cooling rate for Casting Parameters A in Table 3.2 could not be determined, as the solder started to solidify upon contact with the mould surface.

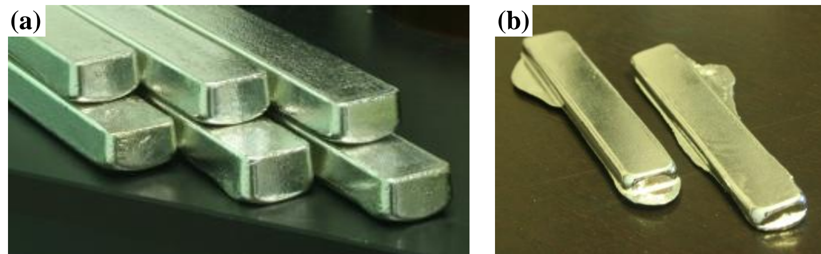

Figure 3.2 Solder in its various forms – (a) Solder bars (b) Cast ingots

Table 3.2 Mould and water temperatures used for casting (Assuming t = 2s)

	Casting Parameters A	Casting Parameters B	Casting Parameters C
Mould temperature (°C)	25	250	250
Water temperature (°C)	25	25	4
Estimated cooling rate (°C/s)	-	112.5	123

The ingots are potted and polished, so that their microstructures could be observed by scanning electron microscopy. First, the centre of the ingots, where the gauge length of the sample would be located when machined, are cut out using a hand saw, labelled, then potted in epoxy and left

overnight to harden. The samples are then ground using a sequence of grit papers of 180, 320, 600 and 1000 for no more than 2 minutes. Following this, the samples are polished using 6 μm, 3 μm and 1μm diamond suspension and microcloth. Finally, 0.05μm blue colloidal silica is used to etch the surface, so that the microstructure of the solder is visible. This final step needs to be carried out for about 3 minutes for lead-free solder and 1 minute for eutectic tin-lead solder. The microstructures of the samples are then examined using a scanning electron microscope at the same scale. The microstructures of the cast samples corresponding to the three casting parameters are shown in Fig 3.3 (the black phase is the tin-rich region while the white phase is the lead-rich region for eutectic tin-lead.). The finest microstructure is obtained using Casting Parameters C, as this yields the fastest cooling rate. Note that the microstructure in Fig 3.3 (c) is comparable to that of the solder joint shown in Fig 3.1. Casting Parameters C was used for the casting of all the samples tested in this study.

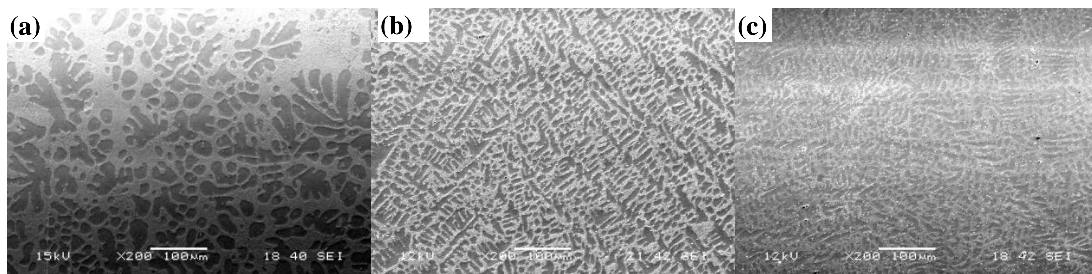

Figure 3.3 Microstructure of SAC305 using (a) Casting Parameters A, (b) Casting Parameters B and (c) Casting Parameters C at the same scale

3.2.2 Microstructure

The microstructures of two solder alloys – SAC305 and SnPb – in cast ingot form and as a solder joint, at the same scale, are shown in Fig 3.4 (a)-(d). As Sn100C solder balls were unavailable, only the microstructure of the cast ingot is shown in Fig 3.4 (e).

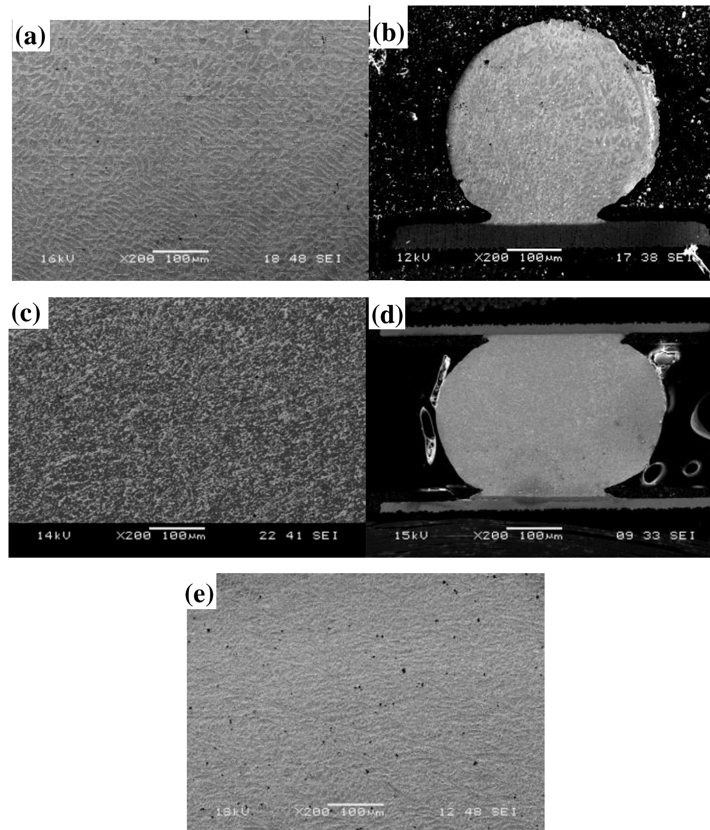

Figure 3.4 Microstructure of (a) SAC305, (b) SAC305 solder joint (c) SnPb (d) SnPb solder joint and (e) Sn100C at the same scale

3.3 TESTS FOR STRENGTH AND STIFFNESS

Three types of tests were carried out to determine the strength and stiffness properties of the solder – microhardness test, uniaxial tension test and uniaxial compression test.

3.3.1 Vickers Microhardness Test

Vickers microhardness tests were carried out using a Shimadzu Microhardness Tester HV-2. Cast samples and solder joints made of eutectic tin-lead and SAC305, as well as cast samples of Sn100C and SAC101 solder joints were tested. Similar microhardness values for cast samples and solder joints would indicate that their microstructures are similar. SAC101, a solder alloy with the composition closest to Sn100C was tested, because Sn100C solder balls were not available.

Cast samples and solder joints were first embedded in epoxy, then ground using 180, 320, 600 and 1000 grade grit paper, and polished to a mirror finish using 6 μm, 3 μm and 1μm diamond suspension and microcloth. Ten measurements were obtained from each sample. Each indentation was made via a load of 10g for 15s. This is the lowest force setting on the tester and was used because solder is relatively soft. A force larger than 10g could cause a pile up effect at the edge of the indentation, which would make it difficult to determine the indentation size, resulting in measurement errors. The tests carried out are summarised in Table 3.3.

Table 3.3 Test Matrix for Microhardness Tests

Materials	SAC305, SnPb, Sn100C (bulk cast samples)
	SAC305, SnPb, SAC101 (solder joints)
Indentation force and duration	10g for 15s
No. of repeats	10

3.3.2 Uniaxial tension tests

An Instron Microtester (Model: 8848) with a 1 kN load cell was used to carry out these tests. As the solder samples are much smaller and softer than typical metallic tensile test samples, the standard (large) grips could not be used. Besides difficulty in accurate positioning of the sample at the centre of the jaws, a correct amount of tightening of the jaw bolts was required – over-tightening of the jaw caused buckling of the sample, while insufficient tightening resulted in slippage. A new set of grips had to be designed and fabricated for this test. These grips were attached to the tester using 11-12mm collets. The new grips facilitate test preparation, as the gripping portion of the clamp is coaxial with the load cell and the moving arm, thus decreasing misalignment of the sample ends. The setup is shown in Fig 3.5.

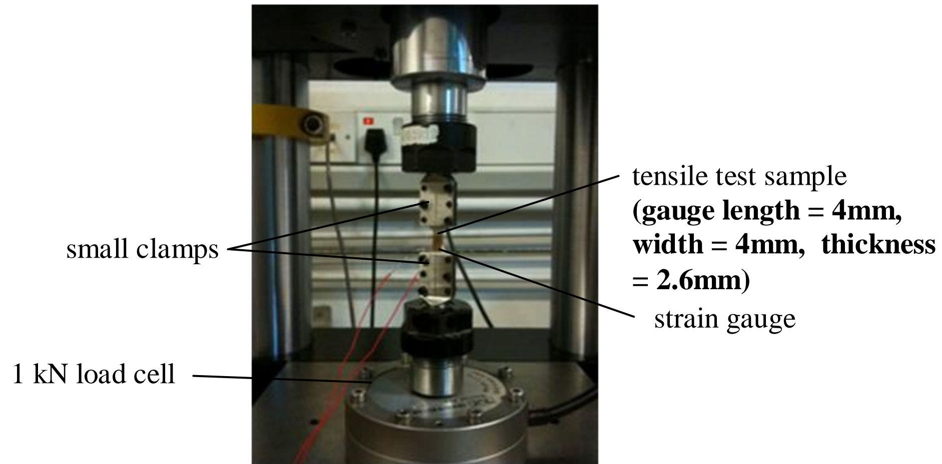

Figure 3.5 Tensile test setup

Strain gauges were attached to the sample using cyanoacrylate (CN) adhesive, to measure the true strain of the sample. This measurement is required for calculation of the Young's modulus. The gauges were connected to a Tokyo Sokki Kenkyujo dynamic strainmeter (Model: DC-92D) which was in turn linked to a Yokogawa Scopecorder (Model: DL750). The load and displacement readings from the Microtester were fed to the oscilloscope using the analogue output feature of the tester and two BNC cables, so that all the readings are obtained with respect to a common time base. As solder is a soft material with a Young's modulus in the range of 40-50 GPa [19], preliminary tests were carried out to ensure that the strain gauge did not stiffen the sample. This was done by performing uniaxial tests on dog-bone shaped solder samples, with and without a strain gauge attached. In both cases, an extensometer was used to measure the strain. The results obtained, shown in Fig 3.6, indicate that there is negligible difference in the stress-strain curves with and without strain gauges attached.

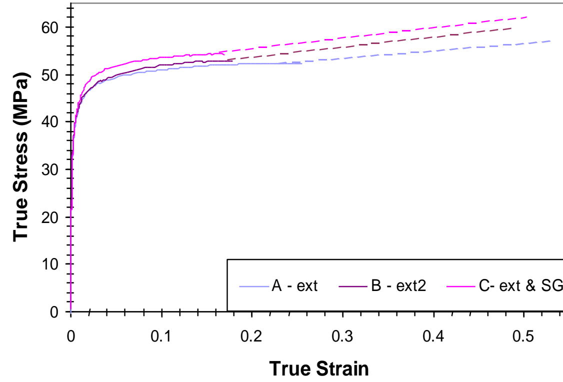

Figure 3.6 True stress-true strain curves of SAC305, with and without strain gauges (SG), from extensometer (ext) measurements.

All tests were carried out at a strain rate of 0.025/s, which corresponds to static test conditions, where there is no creep deformation. For each material, two samples were tested. The test matrix for the tensile tests is shown in Table 3.4.

Table 3.4 Test Matrix for Uniaxial Tension Tests

Materials	SAC305, SnPb, Sn100C
Strain rate	0.025/s
No. of repeats	2

The engineering stress, σ in the gauge length of the sample is defined by:

$$\sigma = \frac{F}{A_o} \quad \textbf{(3.1)}$$

where F is the applied force and A_o the original cross-sectional area of the gauge length.

The engineering strain ε in the sample is defined by

$$\varepsilon = \frac{\Delta L}{L_o} \quad \textbf{(3.2)}$$

where ΔL is the extension of the sample and L_o is the original length.

The true strain ε_t, i.e. the instantaneous strain, and is calculated from

$$\varepsilon_t = \int_{L_0}^{L_i} \frac{dl}{l} = \ln\left(\frac{L_i}{L_o}\right) \quad \textbf{(3.3)}$$

where L_i is the instantaneous length and L_o the original length.

The true stress σ_t is the instantaneous stress; assuming conservation of volume, is defined by

$$\sigma_t = \frac{F}{A_i} = \frac{FL_i}{A_o L_o} = \sigma(1+\varepsilon) \quad \textbf{(3.4)}$$

where A_o is the original area, A_i the instantaneous area, σ the engineering stress and ε the engineering strain.

Stress-strain curves for the different solder alloys were obtained using Eqns. (3.1) and (3.2), while true stress-true strain curves were obtained using Eqns. (3.3) and (3.4). For the elastic portion of the stress-strain curve, strain gauge readings were used instead of displacement data from the Microtester. At the peak load, necking starts to occur and true stress values can no longer be obtained from Eqn (3.4), as the stress state in the gauge length becomes triaxial. The fracture point on the true stress- true strain graph is obtained by dividing the fracture load by the fracture area of the sample . The true stress at fracture is given by Eqn (3.4) and the true strain at fracture is:

$$\varepsilon_t = \ln\left(\frac{A_o}{A_i}\right) \quad \textbf{(3.5)}$$

3.3.3 Uniaxial compression test

Uniaxial compression tests were also carried out using the Instron Microtester. Stiff metal plates were employed to apply compression. The compression test setup and test matrix are shown in Fig 3.7 and Table 3.5 respectively. Cylindrical samples, 4mm in diameter and height, were used. Similar sized samples were used by Wong et. al [25, 45] for tests to determine the compressive properties of solder. An aspect ratio (diameter/ height) of 1 was adopted to prevent buckling of

the samples during testing. These were carefully machined from the cast ingots, so that the top and bottom surfaces of the samples are parallel, and lubricant was also applied to these surfaces to reduce friction and barrelling of the sample. Barrelling would result in a triaxial stress state instead of a uniaxial one. The true strain and stress were then determined using Eqns (3.3) and (3.4).

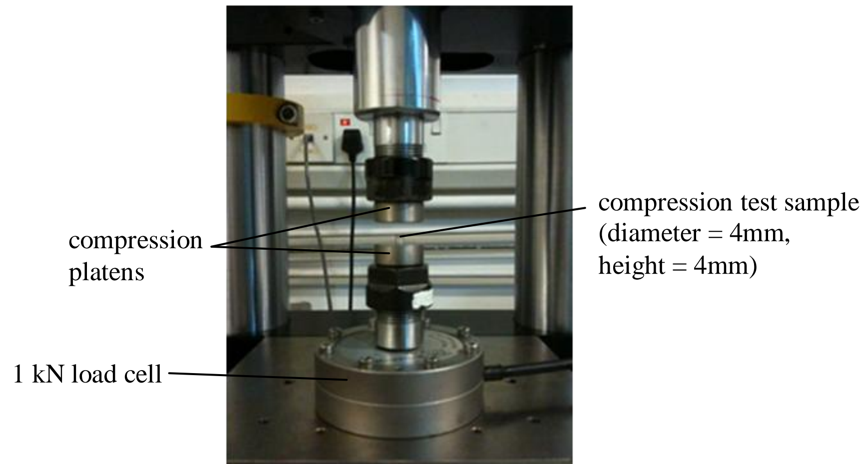

Figure 3.7 Compression Test Setup

Table 3.5 Test Matrix for Uniaxial Compressive Test

Materials	SAC305, SnPb, Sn100C
Strain rate	0.025/s
No. of repeats	2

3.4 FATIGUE TESTING

The test setup and procedure for fatigue tests are similar to that used for tensile tests. The only difference is that instead of applying a monotonic tensile load, a cyclic sine displacement profile is imposed. The test matrix for the fatigue tests is shown in Table 3.6.

The test sample geometry was carefully designed to avoid buckling during compression cycles in the fatigue tests. Strain amplitudes of 0.01 to 0.02, which are beyond the strain at yield, were

chosen so that cyclic softening can be characterised. Strain amplitudes larger than 0.025 resulted in buckling during the fatigue tests. Strain rates of 0.01 and $0.1s^{-1}$ were applied, as these are higher than the strain rate for creep, and most of the solder joint experiences strain rates in this range during drop tests.

Table 3.6 Test matrix for fatigue tests

Materials	SAC305, SnPb, Sn100C
Strain amplitude	0.01, 0.015, 0.02
Strain rate (s^{-1})	0.01, 0.1
No. of repeats	2

Designing test sample geometry

The ASTM standard (E606) for strain-controlled fatigue testing [34] states that for flat sheet fatigue samples with rectangular cross-sections, the length of the gauge section should be three times the thickness. It was found that solder samples of these dimensions undergo significant buckling during the compression cycle of fatigue tests, because solder is softer than most metals.

In order to determine the optimum aspect ratio for the sample, buckling analysis was carried out. Eqn (3.6) is the Euler buckling formula:

$$P = \frac{\pi^2 E I_z}{L_e^2} \quad \textbf{(3.6)}$$

where P is the axial force, E the Young's Modulus, I_Z the second moment of area of the cross-section about the z-axis, and L_e the equivalent length of the column, which is equal to $L/2$ for built-in ends.

Substituting $I_z = \left(\frac{wt^3}{12}\right)$ into Eqn. (3.6) yields,

$$P = \left(\frac{\pi^2 E}{3}\right)\left(\frac{wt^3}{L^2}\right) \quad \textbf{(3.7)}$$

where *w* is the width and *t* the thickness of the sample.

From the preceding expression, it is clear that the primary parameters affecting the critical buckling load are the length and thickness of the sample, which have respective exponents of 2 and 3 in Eqn (3.7). The modulus of the material and the width also affect the buckling force, but to a smaller extent. Assuming a modulus of 50 GPa, the critical axial force *P* for different sample geometries was calculated using Eqn (3.6) and tabulated in Table 3.7 for SAC305 solder. Finite element modelling of the proposed sample designs was carried out to determine the degree of non-uniformity in stress within the gauge length during uniaxial loading. The material properties used in the simulation are given in Table 3.8. Percentage uniformity is defined as the difference between the maximum and minimum stress in the gauge length as a percentage of the maximum stress, and the results are presented in Table 3.7. Dimensions corresponding to sample D3 were adopted for both fatigue and uniaxial tension tests. The stress contours in the gauge length of this sample are shown in Fig 3.8 and solder samples machined to these dimensions are shown in Fig 3.9.

Table 3.7 Percentage non-uniformity of stress in the gauge length for various sample dimensions

Sample	Length (mm)	Width (mm)	Thickness (mm)	P_{Cr} (kN)	% Non-uniformity
ASTM	6.0	4.0	2.0	146.2	5.28
D1	6.5	4.0	2.6	273.7	7.57
D2	5.2	4.0	2.6	427.7	6.88
D3	**4.0**	**4.0**	**2.6**	**722.8**	**8.56**

Table 3.8 Material properties of SAC305 used in FEM modelling

Material	Young's Modulus (GPa)	Poisson's Ratio	Plastic Properties
SAC305	50	0.3	36 MPa @ 0 ε_p 42 MPa @ 0.0035 ε_p 46 MPa @ 0.0115 ε_p 48 MPa @ 0.0185 ε_p

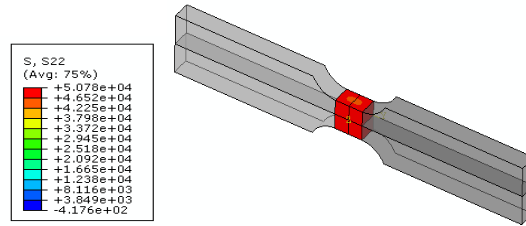

Figure 3.8 Uniform stress in gauge section of test sample

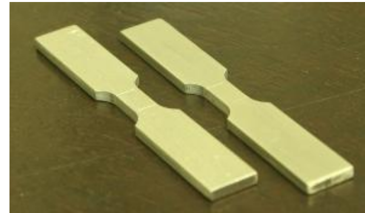

Figure 3.9 Machined dog-bone shaped samples

Correction of strain data

High yield strain gauges (Tokyo Sokki Kenkyujo, Model: YFLA-2) with a gauge size of 2mm by 1.8mm and a backing of 7.5mm by 4mm were used to measure strains during tests. According to the datasheet, the gauges have a strain limit of 15-20% elongation and a fatigue limit of 100 cycles. In addition, it states that there will be a change in apparent strain due to cyclic loading at large strains. Fig 3.10(a) shows the strain-time plot for a sample subjected to a constant displacement fatigue test. For such a test, the strain-time graph is expected to have zero mean strain. An increasing mean strain, shown in Fig. 3.10(a), was observed in all tests. This artefact in the strain reading is the result of damage accumulation in the strain gauge [46]. Inspection of the strain gauges after testing shows extensive damage (Fig 3.11). For dynamic tests, such as the ones carried out in this investigation, the peak-to-peak strain measurements are accurate. As a result, mean strain values were subtracted from the data to obtain corrected strain data; this is plotted in Fig 3.10(b).

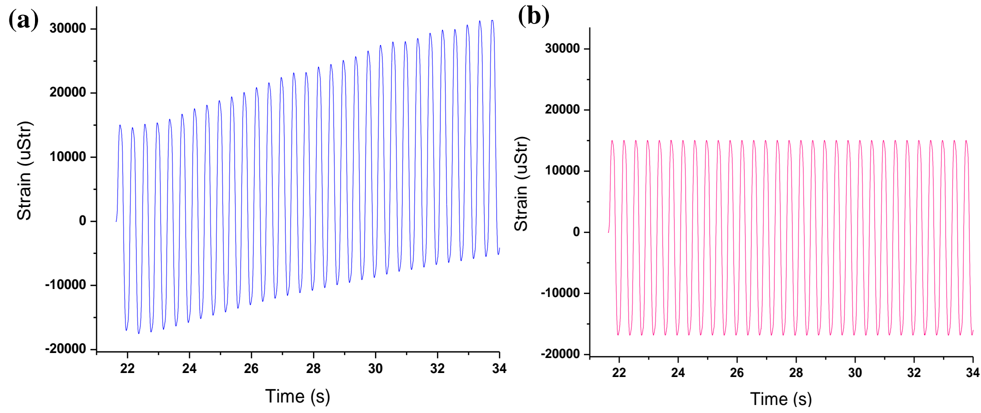

Figure 3.10 (a) Raw strain data with erroneous increasing mean strain; (b) Corrected strain data

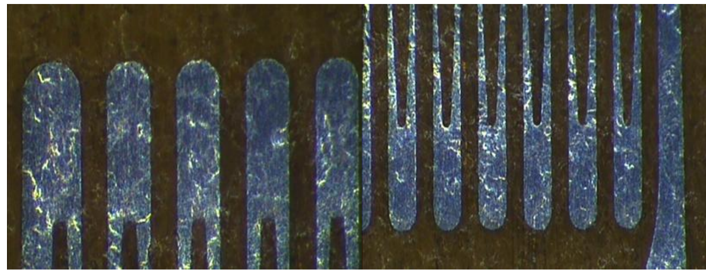

Figure 3.11 Optical micrographs showing damage in strain gauges

Chapter 4

STRENGTH & STIFFNESS PROPERTIES

4.1 INTRODUCTION

This chapter presents results obtained from three types of tests on solder alloys to determine their strength and stiffness properties – microhardness, uniaxial tension and uniaxial compression tests. Comparisons with data from literature are also made.

4.2 VICKERS MICROHARDNESS TEST

Similarity of the microstructures of cast ingots of solder material with samples from solder joints has been qualitatively established in Section 3.2.2, through scanning electron micrographs. The primary objective of these hardness tests was to quantitatively characterise the microstructures of the cast ingots and the solder joints in terms of microhardness values. This section first presents the microhardness of the cast ingots and solder joints separately. This is followed by a comparison of the microhardness values obtained for the same alloy in different forms.

4.2.1 Vickers Microhardness of Cast Ingots

The average Vickers microhardnesses and standard deviations of SAC305, SnPb and Sn100C in cast ingot form are shown in Fig 4.1.

From Fig 4.1, it is clear that both lead-free solder alloys, SAC305 and Sn100C, are harder than SnPb. This phenomenon is well-documented [47] and is attributed to the presence of lead, which is softer than tin.

The standard deviations of the microhardness values are relatively high for the three materials tested, ranging from 0.88 to 0.91. This is because solder is not a homogenous material; there are different phases of varying hardnesses present in it [48]. Depending on where the indenter makes contact, it could be deforming different phases of the material, resulting in a large standard deviation. Fig 4.2 shows indentations on cast ingots of the alloys. Inspection of these indentations indicates that the indentation size is inversely proportional to the hardness, with SAC305 having the smallest indentation.

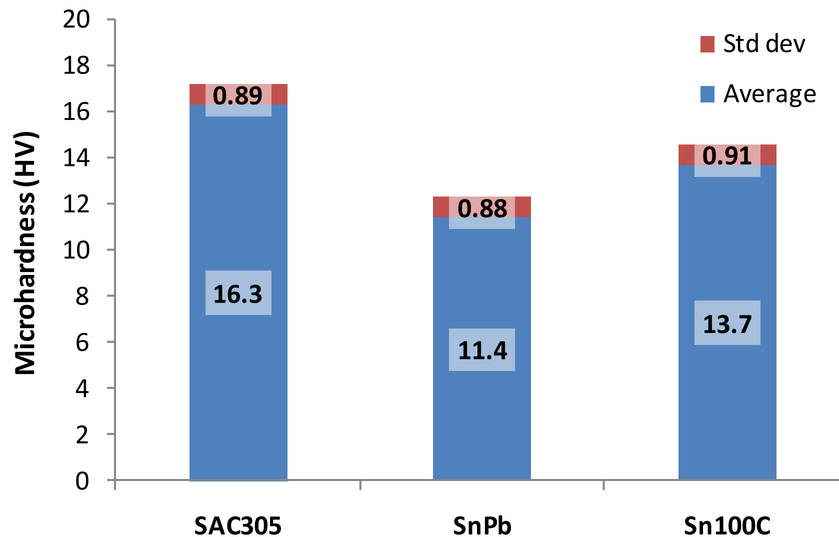

Figure 4.1 Average microhardness and standard deviation from ten indentations on SAC305, SnPb and Sn100C in cast ingot form

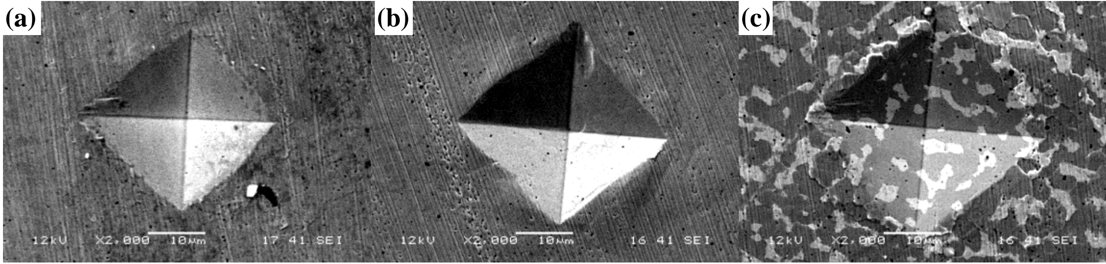

Figure 4.2 Microindentation on cast ingot of solder alloy (a) SAC305, (b) Sn100C and (c) SnPb at a common scale

4.2.2 Vickers Microhardness of Solder Joints

The average Vickers microhardnesses and standard deviations of SAC305, SnPb and SAC101 in solder joint form are shown in Fig 4.3 and scanning electron micrographs of the indentations on solder joints of these alloys are presented in Fig 4.4.

From Fig 4.3, the solder alloy SAC305 is harder than SnPb, and the hardness of SnPb and SAC101 are roughly similar. The standard deviation of the microhardness values for each alloy ranges from 0.44 to 0.90.

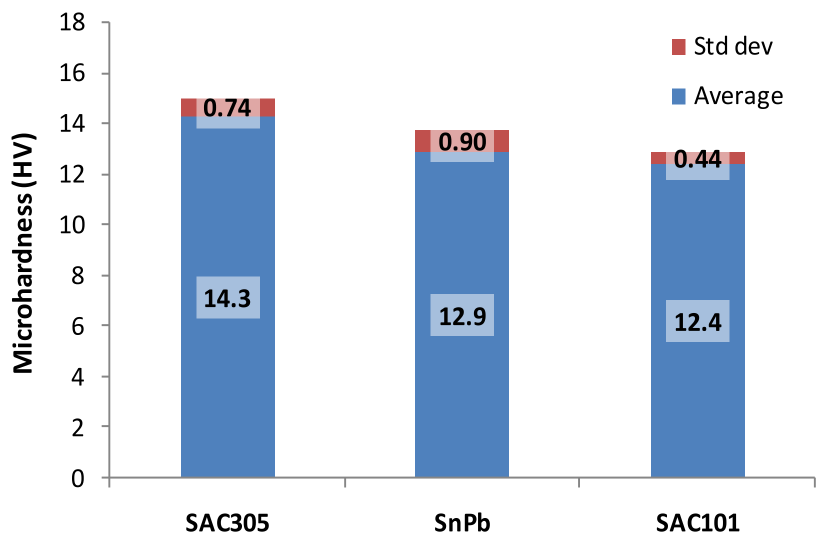

Figure 4.3 Average microhardness and standard deviation from ten indentations on SAC305, SnPb and SAC101 in solder joint form

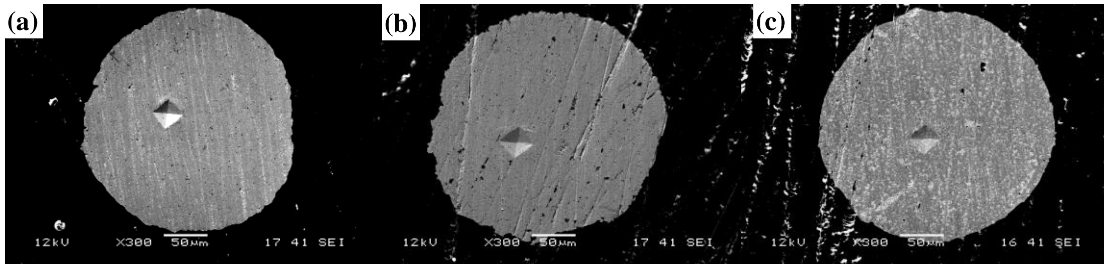

Figure 4.4 Microindentation on solder joints of (a) SAC305, (b) SAC101 and (c) SnPb at the same scale

4.2.3 Comparison of Microhardness for Cast Ingots and Solder Joints

The average Vickers microhardness and standard deviation of the solder alloys tested are presented in Fig 4.5 while the differences between cast ingot and solder joint microhardnesses as a percentage of solder joint microhardness are shown in Table 4.1.

It is observed that cast ingots of the lead-free solders have higher hardness values compared to their solder joint counterparts. For SnPb, however, the solder joints have a higher hardness value than the cast ingots. The difference in hardness values of the solder joints and cast ingots ranges between 10-15%, as shown in Table 4.1. This quantitative result, together with the qualitative comparison of the solder joint and cast ingot microstructures (Section 3.2.1), confirms that samples manufactured through re-melting, casting and quenching of solder bars possess microstructures similar to that of solder joints.

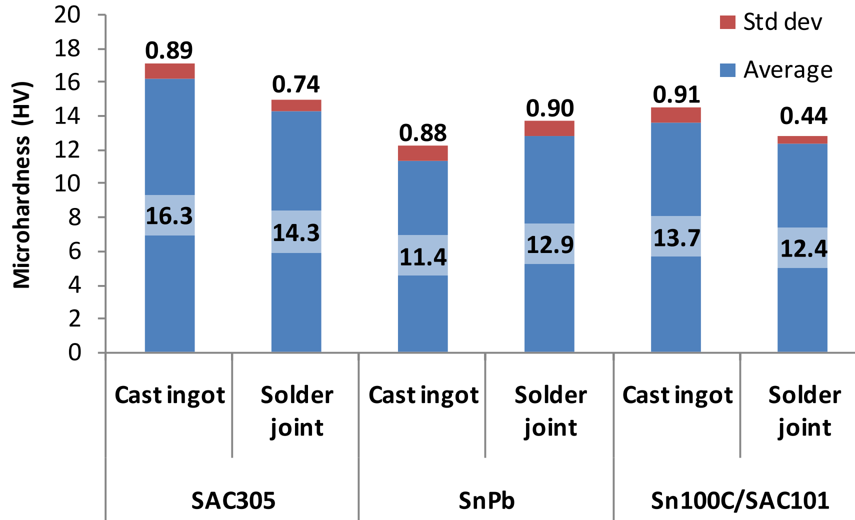

Figure 4.5 Average microhardness and standard deviation from ten indentations on SAC and SnPb in cast ingot and solder joint form, Sn100C in cast ingot form and SAC101 in solder joint form

Table 4.1 Percentage difference in microhardness between the cast ingot and solder joint for each solder alloy

Material	% difference
SAC305	14.0
SnPb	-11.3
Sn100C/SAC101	10.1

4.3 UNIAXIAL TENSION TESTS

The objective of this test was to determine the tensile Young's modulus, yield strength and flow stress of the three solder alloys.

4.3.1 True Stress-True Strain Curves

The true stress-true strain curves for SAC305, Sn100C and SnPb, obtained from uniaxial tension tests are shown in Fig 4.9. These were derived from the force-extension curves obtained experimentally using Eqns 3.1 to 3.4. The solid lines represent data obtained from the experiments before the onset of necking. Once the sample necks, the stress state in the gauge

length of the sample is no longer uniaxial and the measured data cannot be used to derive the uniaxial stress-strain curve. The dotted segments of the curves in Fig 4.9 are straight lines that connect the curve where necking commences to the fracture point. The stress corresponding to the fracture point is obtained by dividing the fracture load by the fracture area of the sample.

The fracture surfaces of samples were examined using a scanning electron microscope; these are shown in Fig 4.10. All the samples failed in a ductile manner, undergoing large elongations and exhibiting necking.

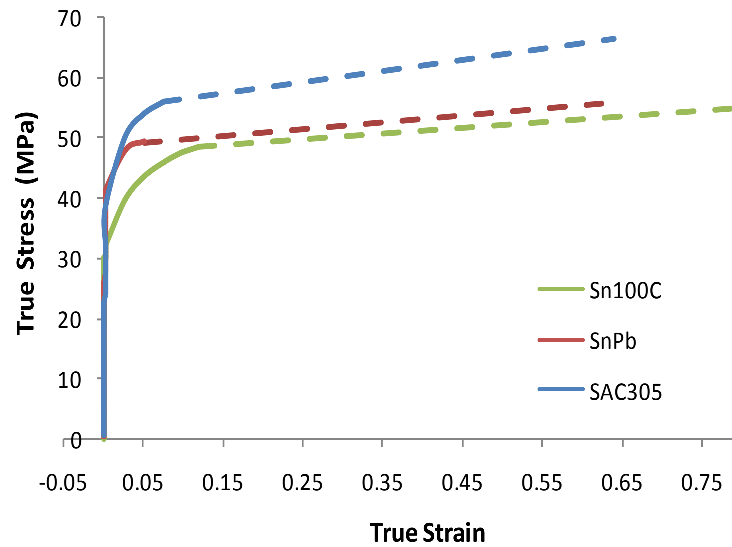

Figure 4.6 True stress-strain curves for SAC305, SnPb & Sn100C, obtained from uniaxial tension tests

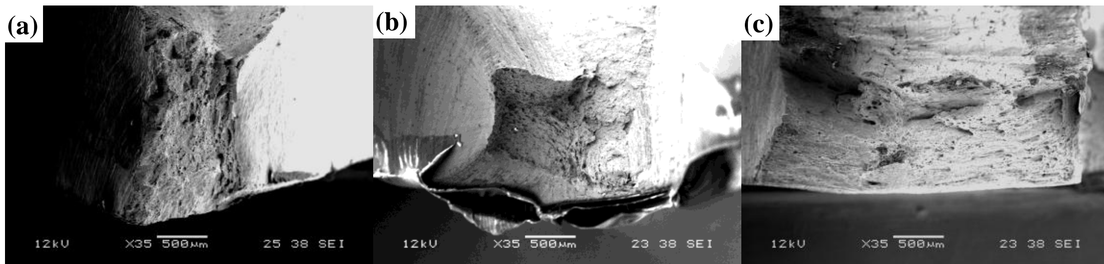

Figure 4.7 Scanning electron micrograph of fracture surfaces of (a) SAC305 (b) Sn100C (c) SnPb at the same scale.

4.3.2 Material Properties Extracted from True Stress-True Strain Graphs

The Young's moduli, offset yield strengths and flow stresses for the three alloys were extracted from the curves and tabulated in Tables 4.2, 4.3 and 4.4 respectively. These are compared with values obtained from literature, which are also included in the respective tables. In general, material properties obtained experimentally are slightly larger than or lie within the range of values obtained from literature.

Table 4.2 shows that SAC305 has the highest Young's Modulus, followed by Sn100C and SnPb. Due to the non-linear nature of the graphs, offset yield strengths corresponding to 0.2%, 0.5% and 1% strain were extracted. For a 0.2% offset, SnPb exhibits the highest yield strength, followed by SAC305 and Sn100C. Flow stresses corresponding to 1%, 5%, 10% and 20% strain were extracted from the curves to determine the degree of strain hardening. SAC305 exhibits the largest strain hardening, followed by Sn100C and SnPb.

Table 4.2 Young's modulus of SAC305, SnPb & Sn100C, obtained from uniaxial tension tests

	Young's Modulus, E (GPa)	
Solder Alloy	**Experimental**	**Literature** [19]
SAC305	54.8	40-50
SnPb	31.0	16-36
Sn100C	40.1	No data

Table 4.3 Offset Yield Strength of SAC305, SnPb & SN100C, obtained from uniaxial tension tests

	Offset Yield Point (MPa)			
	Experimental			**Literature** [19]
Solder Alloy	**0.2%**	**0.5%**	**1.0%**	**0.2%**
SAC305	39.0	41.0	44.0	25-35
SnPb	41.5	42.0	44.0	27 - 41
Sn100C	32.0	33.0	35.0	No data

Table 4.4 Flow Stress of SAC305, SnPb & SN100C, obtained from uniaxial tension tests

	Experimental				Literature [19]
	Flow stress (MPa)				Ultimate Tensile Strength (MPa)
Solder Alloy	1%	5%	10%	20%	
SAC305	43.0	54.0	56.5	58.0	26-47
SnPb	43.5	49.5	50.0	51.0	35-45
Sn100C	35.0	43.5	48.0	49.5	No data

4.4 UNIAXIAL COMPRESSION TESTS

The objective of these tests was to determine the compressive Young's modulus, yield strength and flow stress of the three solder alloys.

4.4.1 True Stress-True Strain Curves

The true stress-true strain curves for SAC305, Sn100C and SnPb, obtained from uniaxial compression tests, are shown in Fig 4.11. These were derived from experimental force-deformation curves using Eqns 3.1 to 3.4.

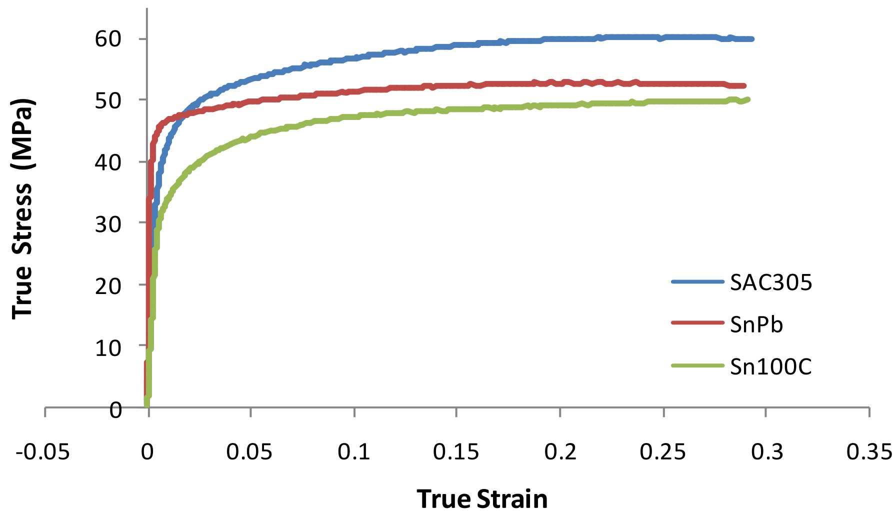

Figure 4.8 True stress-strain curves for SAC305, SnPb & SN100C, obtained from uniaxial compression tests

4.4.2 Material Properties Extracted from True Stress-True Strain Graphs

The Young's moduli, offset yield strengths and flow stresses are presented respectively in Tables 4.5, 4.6 and 4.7. These are compared with values obtained from literature, which are also included in the respective tables [19]. Like the material properties obtained from tension tests, material properties from compression test correlate well with that from literature.

From Table 4.5, it is noted that SAC305 has the highest Young's modulus, followed by Sn100C and SnPb. For a 0.2% offset, SnPb displays the highest yield strength, followed by SAC305 and Sn100C, while SAC305 exhibits the largest strain hardening, followed by Sn100C and SnPb.

Table 4.5 Young's modulus of SAC305, SnPb & Sn100C, obtained from uniaxial compression tests

	Young's Modulus, E (GPa)	
Solder Alloy	**Experimental**	**Literature** [19]
SAC305	48.7	40-50
SnPb	27.2	16-36
Sn100C	34.6	No data

Table 4.6 Offset Yield Strength of SAC305, SnPb & Sn100C, obtained from uniaxial compression tests

	Offset Yield Point (MPa)			
	Experimental			Literature [19]
Solder Alloy	**0.2%**	**0.5%**	**1.0%**	**0.2%**
SAC305	33.0	40.0	45.0	25-35
SnPb	43.0	46.0	47.0	27 - 41
Sn100C	29.0	33.0	36.0	No data

Table 4.7 Flow Stress of SAC305, SnPb & Sn100C, obtained from uniaxial compression tests

	Experimental				Literature [19]
	Flow stress (MPa)				Ultimate Tensile Strength (MPa)
Solder Alloy	**1%**	**5%**	**10%**	**20%**	
SAC305	42.5	53.0	56.5	60.0	26-47
SnPb	47.0	49.5	51.5	52.5	35-45
Sn100C	34.0	44.0	47.0	49.0	No data

4.5 COMPARISON BETWEEN TENSILE AND COMPRESSIVE DATA

Table 4.8 summarizes the Young's moduli, 0.2% offset yield strengths and flow stresses at 5% strain for each solder alloy, determined from uniaxial tension and compression tests. The 0.2% offset yield strength is used in this comparison, as the 0.5% offset yield strengths are similar to the flow stress at 1% strain, indicating that this point has exceeded yielding. The flow stress at 5% strain was used, as the ultimate tensile strength occurs at this strain for tension. There is reasonable agreement between the tensile and compressive properties of the solder alloys.

Table 4.8 Comparison of tensile and compressive material properties

	SAC305		SnPb		Sn100C	
	Tension	Compression	Tension	Compression	Tension	Compression
Young's Modulus, E (GPa)	54.8	48.7	31.0	27.2	40.1	34.6
0.2% Offset Yield Point (MPa)	39.0	33.0	41.5	43.0	32.0	29.0
Flow stress, 5% (MPa)	54.0	53.0	49.5	49.5	43.5	44.0

4.6 SUMMARY

Microhardness tests confirmed that the microstructure found in cast ingots was similar to that in solder joints within 15%.

The solder alloys characterized are ranked in terms of hardness and strength in Table 4.9, with the hardest and strongest being ranked 1. SAC305 is the stiffest alloy tested, in terms of microhardness, Young's modulus and flow stress. Sn100C and SnPb are generally softer, with SnPb having the lowest microhardness and Young's modulus. Sn100C has the lowest yield strength and flow stress.

Table 4.9 Solder alloys ranked from highest (1) to lowest (3) for each material property

	SAC305	Sn100C	SnPb
Microhardness	1	2	3
Young's Modulus	1	2	3
0.2% Offset Yield Strength	2	3	1
Flow stress, 5%	1	3	2

Chapter 5

FATIGUE PROPERTIES OF SOLDER

5.1 INTRODUCTION

This chapter presents the results and analysis of the fatigue characteristics of three solder alloys – SAC305, Sn100C and SnPb, subjected to cyclic loading at three strain amplitudes (0.01, 0.015, 0.02) and two strain rates (0.01, 0.1/s). In addition to comparisons between cyclic stress-strain curves, the Bauschinger effect in these solder alloys is also quantified in terms of a scalar parameter. S-N curves for the solder alloys tested are also presented.

5.2 GENERAL CHARACTERISTICS OF CYCLIC STRESS-STRAIN CURVES

Typical cyclic stress-strain curves for eutectic tin-lead solder and lead-free SAC305 solder tested at large strain amplitudes and strain rates are shown in Figs 5.1(a) and (b) respectively. A typical curve for Sn100C solder is not included, as its characteristics are similar to that of SAC305. Plotting of the stress-strain responses cycles at intervals of 20 or 50, instead of every cycle facilitates clearer visualization. The interval selected depends on the fatigue life of the sample – a larger interval is used for samples with longer lives. Fig 5.1 shows that both solder alloys undergo

cyclic softening, characterised by a decrease in the maximum flow stress as the number of test cycles increases. This phenomenon is further discussed in Section 5.2.1.

Besides cyclic softening, the lead free alloys – SAC305 and Sn100C – exhibit strain hardening. This is more pronounced at higher strain rates. SnPb does not strain harden noticeably at either strain rate. The strain hardening of solder and changes in the hysteresis loop for different strain amplitudes and strain rates will be considered in Section 5.2.2.

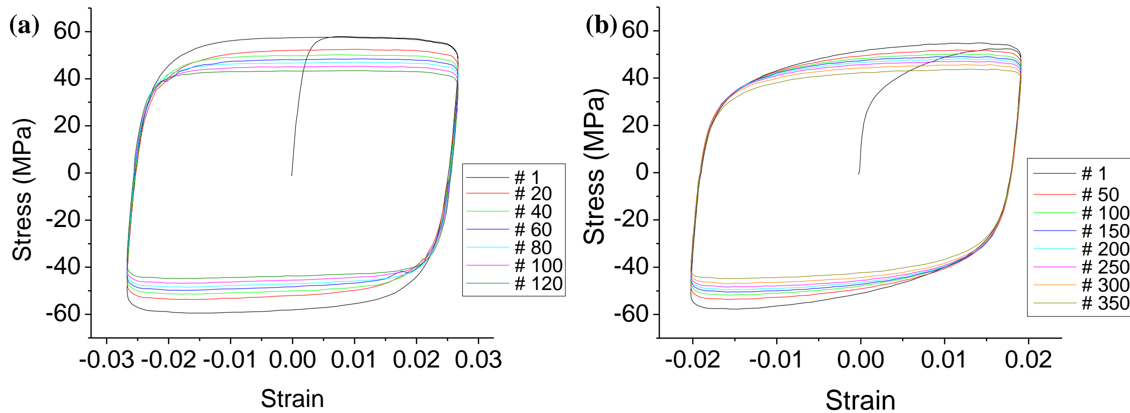

Figure 5.1 (a) Stress-strain curves for SnPb at strain rate of 0.27/s and strain of 0.027 (b) Stress-strain curves for SAC305 at strain rate of 0.14/s and strain of 0.02

5.2.1 Cyclic Softening of Solder

Fig. 5.2 shows how the maximum stress amplitude changes throughout a displacement-controlled fatigue test for SAC305. For the first few cycles, the stress amplitude is almost constant, and subsequently, there is a gradual decrease. This stress decrease constitutes most of the response in the life of the sample. When the material starts to fail through propagation of a fatigue crack, the decrease in stress is sharper [49]. According to ASTM standard E606 [34], failure is defined as the point where there is a 50% decrease of stress in the sample. This criterion is not appropriate for solder, as solder is much softer than other metals and is considered to have failed before that stage of strength decrease. In his work to characterise the fatigue properties of various solder alloys, Kanchanomai [28, 31-33, 50-52] defined failure to be where there is a 25% drop in stress.

It is apparent from Fig 5.2 that a 25% decrease in stress occurs after the significant change in slope, where the stress starts to decrease sharply. In this study, failure is considered to correspond to the 'knee' of the logarithmic curve relating stress amplitude with the number of cycles, because fatigue cracks start to propagate at that point.

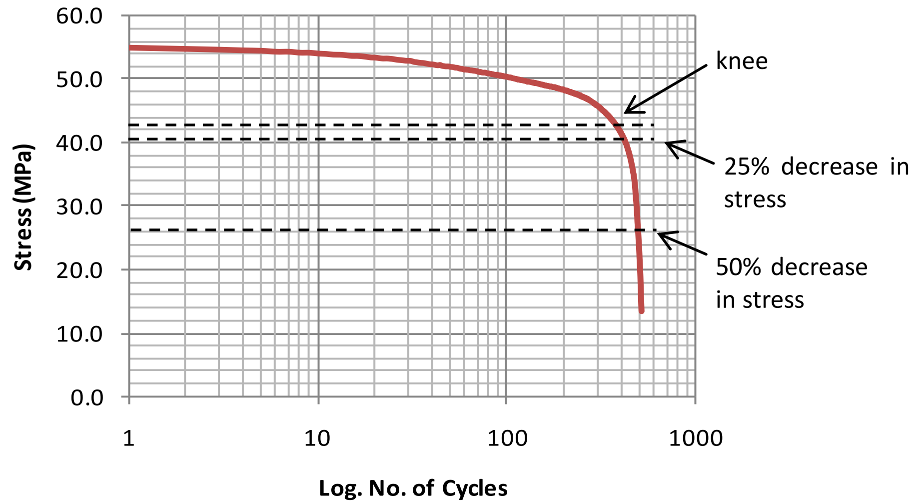

Figure 5.2 Variation of Stress with Logarithm of Number of Cycles for SAC305

5.2.2 Effect of Test Conditions on Profile of Hysteresis Loops

As discussed in the previous section, the first few cycles of a cyclic test are the most stable, with the maximum stress amplitude remaining constant. The first few test cycles carried out on SnPb and SAC305 samples at a low strain rate and various strain amplitudes are plotted in Fig 5.3. The different colors for the graphs indicate the different strain amplitudes. Similar plots for tests carried out at a strain amplitude of about 0.02 and different strain rates are presented in Fig 5.4. These are used for comparison of the effect of varying the strain and strain rate respectively.

At a strain rate of 0.01/s, SnPb exhibits significantly less strain hardening than SAC305, as shown in Fig 5.3. Consequently, for SnPb, as the strain amplitude imposed increases, the hysteresis loops merely enlarge in the horizontal direction without noticeable vertical expansion. SAC305, on the other hand, undergoes a fair amount of strain hardening, resulting in hysteresis loops which enlarge along both axes as the strain applied is increased.

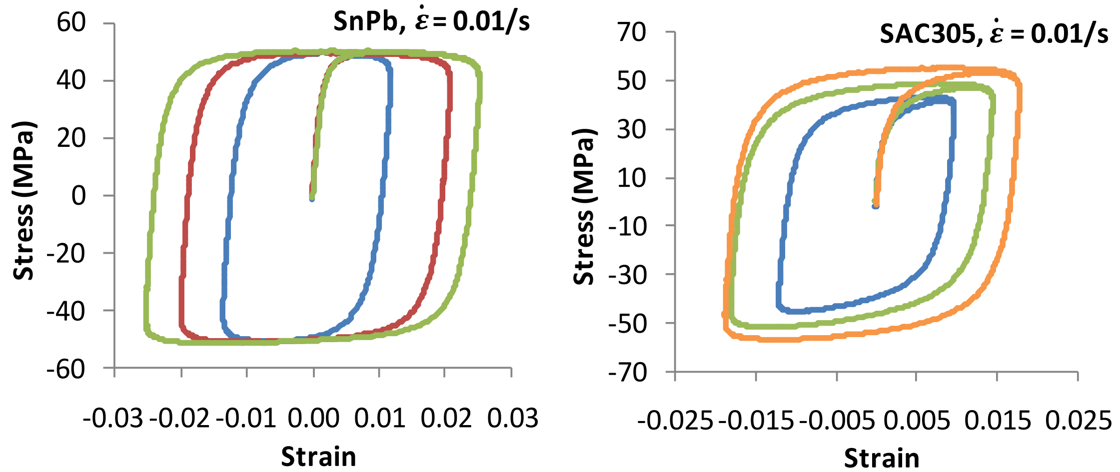

Figure 5.3 Initial stress-strain cycles for SnPb and SAC305 at strain rate of 0.01 /s

A change in the strain rate from 0.01/s to 0.1/s increases the flow stress for SnPb, as shown in Fig 5.4. For SAC305, greater strain hardening is observed for a higher strain rate of 0.1/s. There is no significant change in flow stress for SAC305.

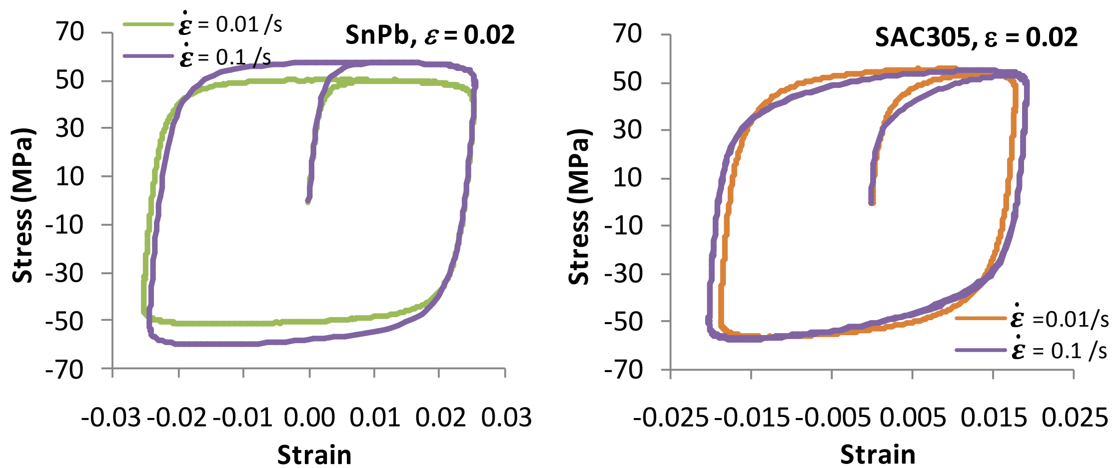

Figure 5.4 Initial stress-strain cycles for SnPb and SAC305 at strain of 0.02

5.3 THE BAUSCHINGER EFFECT

As discussed in Section 4.5, solder is an isotropic material which has the same yield strength in tension and compression. Consequently, under monotonic loading, the yield surface in the π-plane of a three-dimensional principal stress space is a circle with its center at the origin. Under fatigue loading, however, it is apparent that the loading history changes the size of the yield circle and shifts its centre. To characterize these effects, two strain-hardening descriptions – kinematic hardening and isotropic hardening – are employed.

When a material is loaded beyond its yield point in tension, subsequently unloaded, then reloaded in compression, its yield strength in compression tends to be lower than that in tension. This is known as the Bauschinger effect and is shown schematically in Fig. 5.5, where $\sigma_{y2} < \sigma_{y1}$. This is related to kinematic hardening, which involves translation of the yield envelope with respect to the stress origin, as a result of previous loading. In contrast, isotropic hardening or softening causes an increase or decrease in size of the yield envelope respectively, without any translation with respect to the stress origin. Isotropic softening is used to characterise the cyclic softening portion of the cyclic stress-strain curves.

The extent of the Bauschinger effect or kinematic hardening of a material, can be quantified using scalar parameters based on the ratio of the yield strengths in tension and compression. One such parameter is evaluated for the materials tested and presented in the following section.

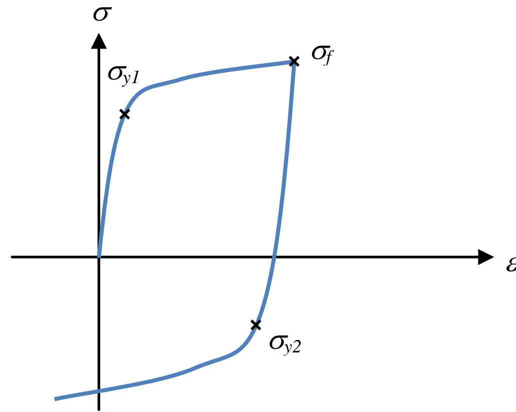

Figure 5.5 Stress-strain curve depicting the Bauschinger effect, where the yield strength in compression is smaller than that in tension. σ_{y2} is the yield point in tension, σ_{y2} the yield points in compression and σ_f the maximum flow stress in tension.

In order to characterise the extent of isotropic and kinematic hardening, the Talypov equation [53] is used.

$$\beta = \frac{\sigma_f - |\sigma_{y2}|}{\sigma_f} = 1 - \frac{|\sigma_{y2}|}{\sigma_f} \tag{5.1}$$

where β is a scalar parameter defining the extent of kinematic hardening, σ_{y2} is the yield stress in compression and σ_f the maximum flow stress in tension. This equation normalizes the difference between the flow stress in tension and the magnitude of the yield stress in compression with respect to the flow stress.

For a material that undergoes purely isotropic hardening,

$$\sigma_{y2} = -\sigma_f \tag{5.2}$$

As a result, $\beta = 0$

Conversely, if the material undergoes purely kinematic hardening,

$$\sigma_{y2} = \sigma_f - 2\sigma_{y1} \tag{5.3}$$

As a result,

$$\beta = 2\left(1 - \frac{\sigma_{y1}}{\sigma_f}\right) \tag{5.4}$$

where σ_{y1} is the yield stress in tension.

5.3.1 Comparison between β determined at 0.2% and 0.4% offset yield strength

To obtain an appropriate value for β, the yield strength in Eqn 5.1 must be determined accurately. As the experimental stress-strain curves are non-linear (Figs 5.3 and 5.4), β was evaluated and plotted for two offset yield strengths – 0.2% and 0.4%. The values for β for SAC305 and SnPb are plotted against strain amplitude in Fig 5.6. In general, as the strain imposed increases, β increases. This indicates that the kinematic hardening component increases with applied strain. The values of β for SAC305 are larger than that for SnPb, indicating that SAC305 undergoes greater kinematic hardening than SnPb. Use of a 0.4% offset yield point results in a lower value of β than determining β from a 0.2% offset. The spread in data is also smaller with a 0.4% offset yield point, and a clearer trend can be discerned. For the remaining plots of β in this chapter, the 0.4% offset yield point is used.

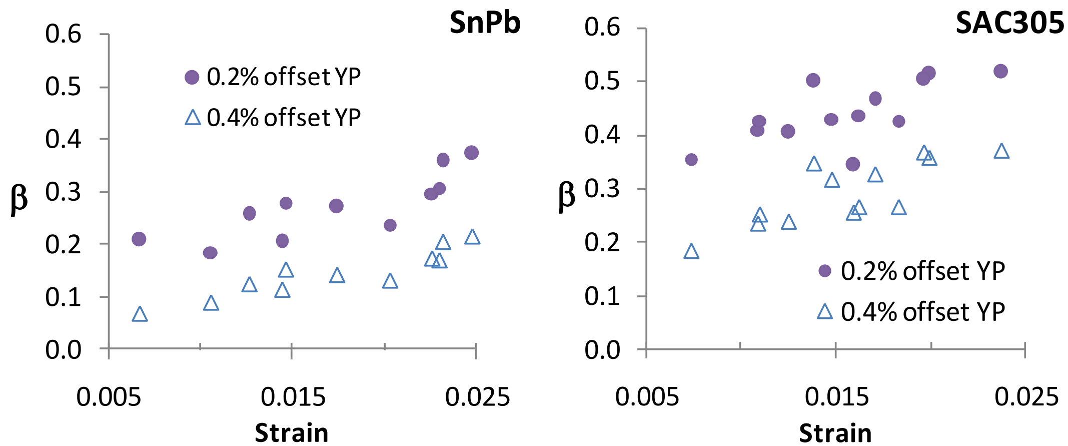

Figure 5.6 Variation of β with strain for SnPb and SAC305, corresponding to yield points determined at 0.2% and 0.4% offset for all test conditions

5.3.2 Rate dependence of β

In Figure 5.7, the values for β for SAC305 and SnPb are plotted as functions of strain amplitude imposed for two strain rates. When fitted by a straight line, the slopes and R^2 correlation values obtained for these graphs are shown in Table 5.1. The slope indicates how dependant the β value or extent of kinematic hardening is on strain, while the R^2 value quantifies how good the fit to the straight line is (the higher the value, the better the fit). At both strain rates, SAC305 has larger slopes. Furthermore, for both materials, an increase in slope is observed as the strain rate is increased. This indicates that the hardening properties of both materials are rate-dependant.

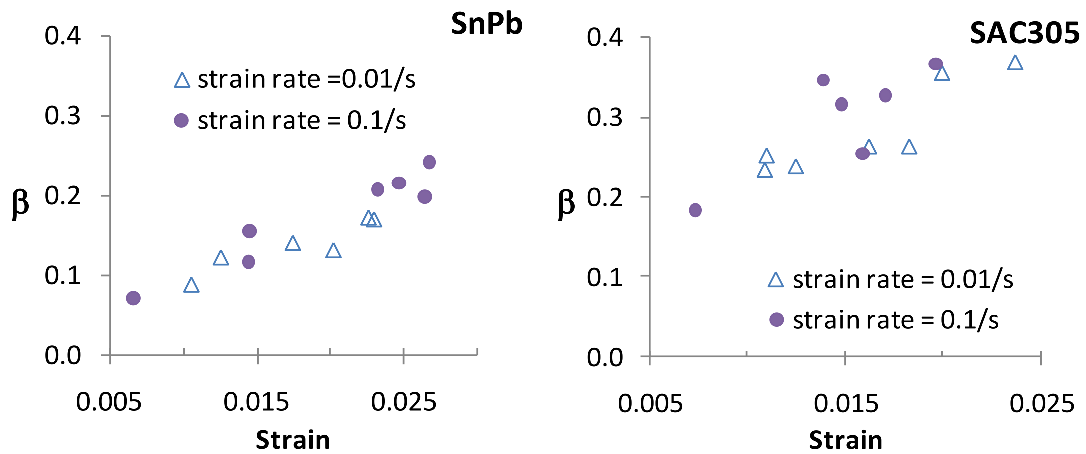

Figure 5.7 Variation of β with strain at two strain rates, for SnPb and SAC305 for all test conditions

Table 5.1 Comparison of slopes and R-squared values for β vs strain in SnPb and SAC305

Solder Alloy	**SnPb**		**SAC305**	
	Slope	R-squared	Slope	R-squared
$\dot{\varepsilon}$=0.01/s	5.6	0.84	10.2	0.80
$\dot{\varepsilon}$=0.1/s	7.6	0.92	13.5	0.67

5.3.3 Comparison of β for different solder alloys

The values of β for SAC305, SnPb and Sn100C are plotted against strain amplitude in Fig 5.8, for two strain rates. It is evident that Sn100C and SAC305 have larger β values compared to SnPb, as the lead free solder alloys undergo greater kinematic hardening.

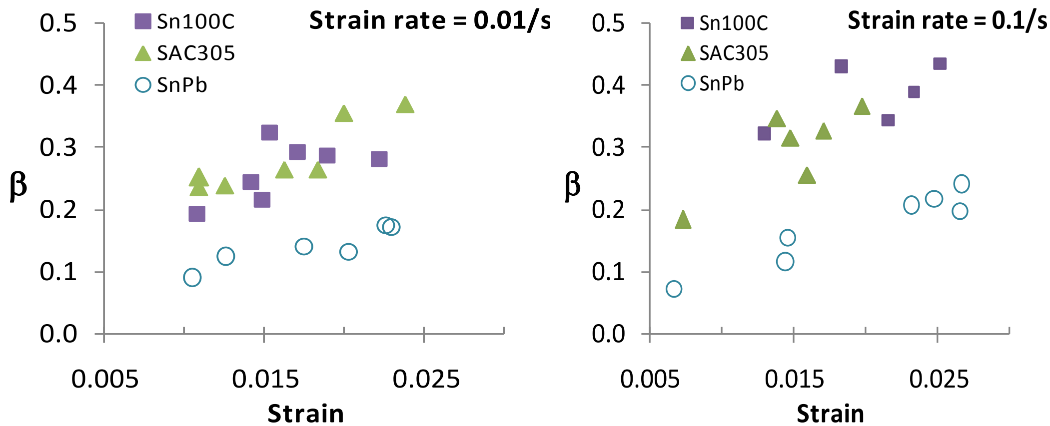

Figure 5.8 Variation of β with strain amplitude imposed for three solder alloys at two strain rates

5.4 S-N Curves

As mentioned in Section 5.2.1, failure is defined as the point where the stress in a sample begins to decrease rapidly, i.e. where a 'knee' occurs, as shown in Fig 5.2. Kanchanomai [28, 31-33, 50-52], on the other hand, defined failure as corresponding to a 25% decrease in stress. Fig 5.9 shows a comparison of these two definitions in an S-N plot for SAC305 at two strain rates. For both strain rates, defining failure as corresponding to the 'knee' results in a more conservative lifetime, as expected.

The S-N curve at two strain rates for each solder alloy is shown in Fig 5.10. Solder exhibits behavior typical of metallic materials, failing earlier for cyclic loading at a higher strain amplitude. All three solder alloys show an extension in fatigue life (number of cycles to failure) at higher strain rates. Similar results were obtained by Kanchanomai [31] for SnPb. This was

attributed to a change in the failure mechanism from cavitation due to grain boundary sliding, to cavitation with no grain boundary sliding. Note that in terms of time to failure, samples tested at higher strain rates failed earlier. A comparison shows that Sn100C has the longest life, followed by SAC305 and SnPb.

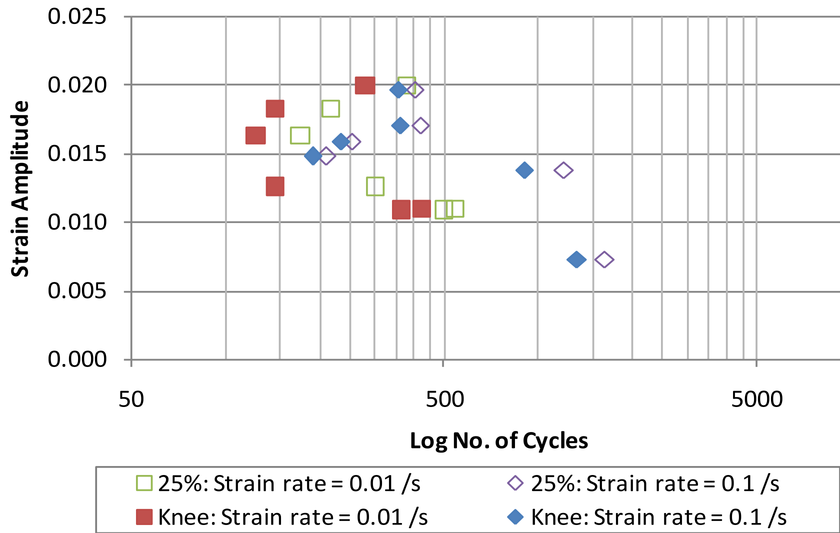

Figure 5.9 Plot of strain amplitude imposed against logarithm of number of cycles at failure, showing that failure defined by the 'knee' occurs sooner than that defined by a 25% decrease in stress

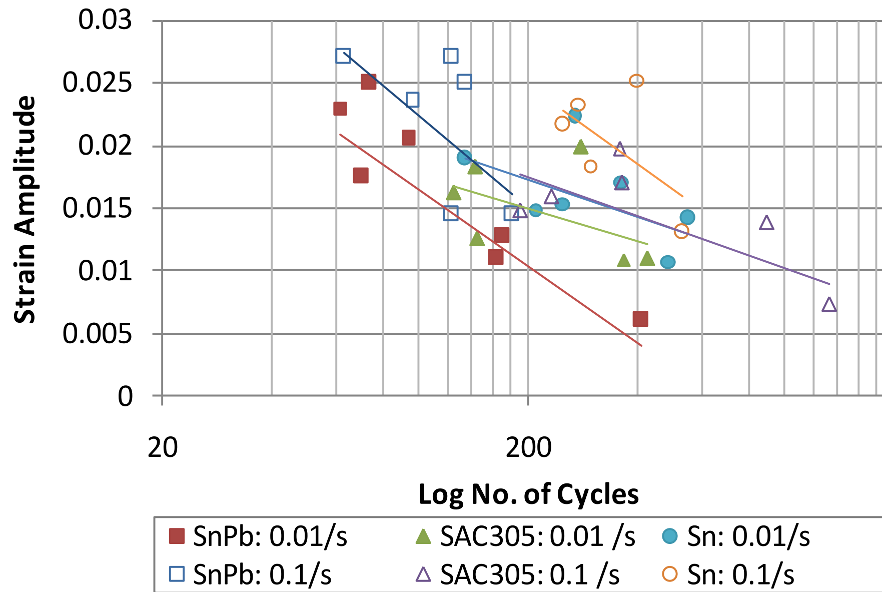

Figure 5.10 S-N curves for three solder alloys tested at two strain rates – 0.01/s and 0.1/s

The Coffin-Manson law describes low cycle fatigue behavior by

$$\Delta\varepsilon_p N_f^{\alpha} = \theta \tag{5.5}$$

The constants α and θ for SnPb and SAC305 are presented in Table 5.2. There is reasonable agreement between the constants determined for SnPb at 0.01/s and values obtained from literature. For both SnPb and SAC305, the constants are strain rate dependant [28].

Table 5.2 Coffin-Manson constants for SnPb and SAC305

	Strain Rate/s	α	θ
SnPb [28]	0.001	0.63-0.68	0.63-0.85
SnPb	0.01	0.70	0.79
	0.1	0.42	0.30
SAC305 [50]	0.002 – 0.008	0.73	3.7
SAC305	0.01	0.13	0.061
	0.1	0.28	0.14

5.5 SUMMARY

Uniaxial fatigue tests carried out on three solder alloys show that both lead-free and eutectic tin-lead solders undergo cyclic softening as shown in the cyclic stress-strain curves, where the hysteresis curves progressively decrease in size with the number of cycles. Strain hardening in lead-free solder is more pronounced than that in SnPb solder. This is evident for SAC305, as the hysteresis loops enlarge along both axes with an increase in imposed strain. For SnPb, the hysteresis loops enlarge only along the horizontal direction. The profile and size of the hysteresis curve change in different ways for lead-free solder alloys and SnPb.

To quantify the extent to which kinematic hardening causes changes in the hysteresis loops, as described above, a scalar kinematic-hardening parameter β, corresponding to a 0.4% offset yield

point was used. From this, it was found that the extent of kinematic hardening in solder increases with the cyclic strain amplitude applied. It was also ascertained that the hardening properties of solder are rate-dependant. In addition, Sn100C and SAC305 exhibit a larger degree of kinematic hardening than SnPb.

Finally, the S-N curves of the solder alloys indicate a longer fatigue life, in terms of number of cycles to failure, at higher strain rates. However, with regard to time to failure, samples subjected to lower strain rates last longer. Sn100C has the longest life, followed by SAC305 and SnPb, for both strain rates examined. This is because the time taken for one cycle varies with strain rate.

Chapter 6

MODELLING OF FATIGUE CHARACTERISTICS

6.1 INTRODUCTION

This chapter presents a method for extracting the isotropic softening and kinematic hardening material parameters from experimental cyclic stress-strain curves, such as those presented in Section 5.2. These material parameters can be used in finite element modelling for estimation of stresses. In addition, simulation of a printed circuit board subjected to vibration at 30Hz, in which the solder joint material is modelled using the stress-softening parameters, is demonstrated.

6.2 THEORETICAL CONSIDERATIONS IN IMPLEMENTING HARDENING BEHAVIOUR IN ABAQUS

The commercial finite element software, ABAQUS (Version 6.8 EF1) was used to analyse solder joint stresses in a vibrating printed circuit board. Hence, the material models available that incorporate hardening were assessed for suitability to model solder. There are two kinematic hardening models in ABAQUS – linear kinematic hardening and nonlinear isotropic-kinematic

hardening. The nonlinear isotropic-kinematic hardening model was chosen for its ability to yield better predictions of material behavior [54].

In this model, isotropic hardening is described by

$$\sigma = \sigma_0 + Q\left(1 - e^{-b\varepsilon^{pl}}\right) \quad \textbf{(6.1)}$$

where σ is the instantaneous stress, σ_0 the initial yield stress, ε^{pl} the plastic strain, and Q and b are material constants. Q and b describe how the stress increases or decreases. When Q is negative, Eqn. 6.1 describes isotropic softening.

Kinematic hardening is defined by

$$\dot{\boldsymbol{\alpha}}_{\boldsymbol{k}} = \boldsymbol{C}_{\boldsymbol{k}}\, \dot{\bar{\boldsymbol{\varepsilon}}}^{\boldsymbol{pl}} \frac{\mathbf{1}}{\boldsymbol{\sigma}_{\mathbf{0}}}(\boldsymbol{\sigma} - \boldsymbol{\alpha}) - \boldsymbol{\gamma}_{\boldsymbol{k}}\boldsymbol{\alpha}_{\boldsymbol{k}}\dot{\bar{\boldsymbol{\varepsilon}}}^{\boldsymbol{pl}} \quad \textbf{(6.2)}$$

and

$$\alpha = \sum_{k=1}^{N} \alpha_k \quad \textbf{(6.3)}$$

where $\dot{\boldsymbol{\alpha}}_{\boldsymbol{k}}$ is the rate of change of the backstress, α_k is the kth backstress, and C_k and γ_k are material constants; $\dot{\bar{\boldsymbol{\varepsilon}}}^{\boldsymbol{pl}}$ is the plastic strain rate, σ_0 is the instantaneous stress and N the number of backstresses. Note that for each backstress, there are two material constants.

6.3 MODELLING METHODOLOGY

The methodology used to model the cyclic softening of solder is illustrated in Fig 6.1. The two strain hardening characteristics – isotropic softening and kinematic hardening are modelled separately. The isotropic softening material constants Q and b are first determined through fitting of experimental data. Next, the kinematic hardening constants C_k and γ_k are calculated using ABAQUS. Finally, all four material constants (Q, b, C_k and γ_k) which describe the hardening properties are specified as inputs for simulation of printed circuit board vibration. Models with

and without hardening properties can then be compared to assess whether there is a change in maximum stress when hardening properties are present.

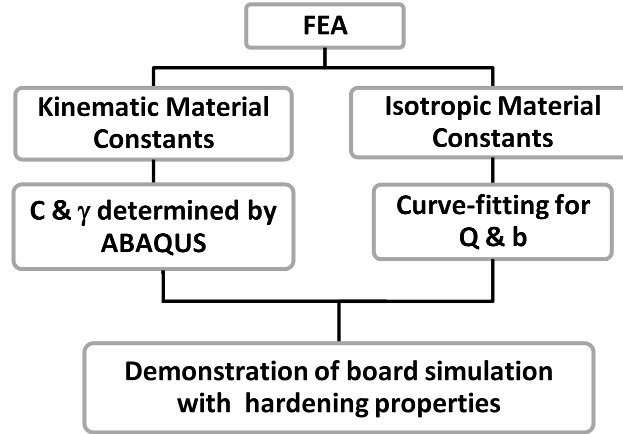

Figure 6.1 Flow chart of modelling methodology to determine material constants and assess improvement in accuracy with hardening properties incorporated

6.4 EVALUATION AND VALIDATION OF MATERIAL MODELS

6.4.1 Determination of Isotropic Softening Material Constants *Q* and *b*

To determine the material constants *Q* and *b*, fitting of an equation similar in form to Eqn 6.1 is used.

$$y = A\left(1 - e^{-bx}\right) \quad \textbf{(6.4)}$$

where *A* and *b* are constants.

Rearrangement of Eqn 6.1, which describes the isotropic behaviour of solder, yields:

$$\sigma - \sigma_0 = Q\left(1 - e^{-b\varepsilon^{pl}}\right) \quad \textbf{(6.5)}$$

This has a form similar to the equation to be fitted. Experimental data was plotted in terms of (σ - σ_0) as a function of ε^{pl}, as shown in Fig. 6.2. The data was then fitted by Eqn. 6.4. Only the data corresponding to points before failure at the 'knee' of the graphs were used (defined by the solid

line). The material properties Q and b are represented respectively by the constants A and b. Figure 6.2 shows a typical fit of experimental data by Eqn. 6.3; the values of Q and b extracted for each material for given test conditions are presented in Table 6.1.

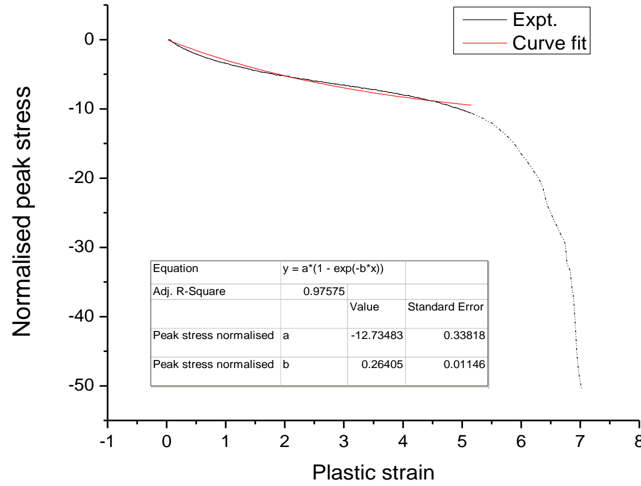

Figure 6.2 Curve-fitting to determine constants *Q* and *b*

Table 6.1 Values of *Q* and *b* for various solder alloys and test conditions

	Strain rate = 0.01 s^{-1}						Strain rate = 0.1 s^{-1}					
	Low Strain		Med. Strain		High Strain		Low Strain		Med. Strain		High Strain	
	Q	***b***	***Q***	***b***	***Q***	***b***	***Q***	***b***	***Q***	***b***	***Q***	***b***
SAC305	-5.7	0.25	-4.0	0.44	-8.0	0.31	-4.3	0.10	-12.7	0.26	-9.6	0.18
SnPb	-9.5	0.57	-10.2	0.49	-8.5	0.68	-12.9	0.59	-13.0	0.40	-15.1	0.36
Sn100C	-15.9	0.07	-7.4	0.11	-10.2	0.16	-11.1	0.13	-8.4	0.22	-11.0	0.10

6.4.2 Determination of Kinematic Hardening Material Constants C_k and γ_k

ABAQUS is able to calculate the material constants C_k and γ_k when provided with the following information – elastic modulus, Poisson's ratio, experimental data points from uniaxial cyclic tests and number of backstresses.

In most fatigue tests, hysteresis is significant at the beginning, and then stabilizes after a certain number of cycles. The stabilized curve defines most of the sample life. Subsequently, a crack

initiates and propagates, causing the stress to decrease and the sample to fail [49]. In such cases, the stabilized loop is usually used for analysis of hardening.

With solder, however, the first few cycles have relatively stable hysteresis loops, which become progressively smaller and smaller initially due to isotropic softening, and later because of crack propagation. To determine the hardening constants, data from the initially stable hysteresis loops were used. A typical stabilized stress-strain curve with a tensile portion termed a 'half cycle', marked by a dashed line, is shown in Fig 6.3 (a). ABAQUS requires data corresponding to a horizontally displaced half cycle, starting from the yield point where the plastic strain is zero, to serve as an input. This is illustrated in Fig 6.3 (b). However, because of the non-linear nature of the stress-strain data, the yield point of the material is difficult to determine.

Correct identification of the yield point is essential for accurate determination of the hardening constants. The yield point of the input material data was varied so that three sets of kinematic hardening parameters can be obtained. Figure 6.3(c) shows the input material data for different yield points.

The solder specimen is modelled by a single beam element, as shown in Fig 6.4, and elastic material properties such as the elastic modulus and Poisson's ratio are defined. Isotropic material hardening parameters, listed in Table 6.1, are also provided as inputs. One set of kinematic material hardening properties, corresponding to a particular yield point, are also specified. To simulate a displacement-controlled uniaxial fatigue test, one end of the beam element was fixed while the other end was subjected to cyclic displacement similar in amplitude and displacement to that in experiments. The resulting stress-strain curve is then extracted. This process is repeated using the other two sets of kinematic hardening material properties. Figure 6.5 shows the experimental stress-strain curves and simulation results based on the kinematic hardening properties corresponding to the three different yield points. It is concluded that the curve corresponding to a yield point of 35 MPa has the best fit with the experimental curve. The C_k and

α values obtained for this case are presented in Table 6.2. This procedure was repeated for all the alloys tested, at their respective test conditions.

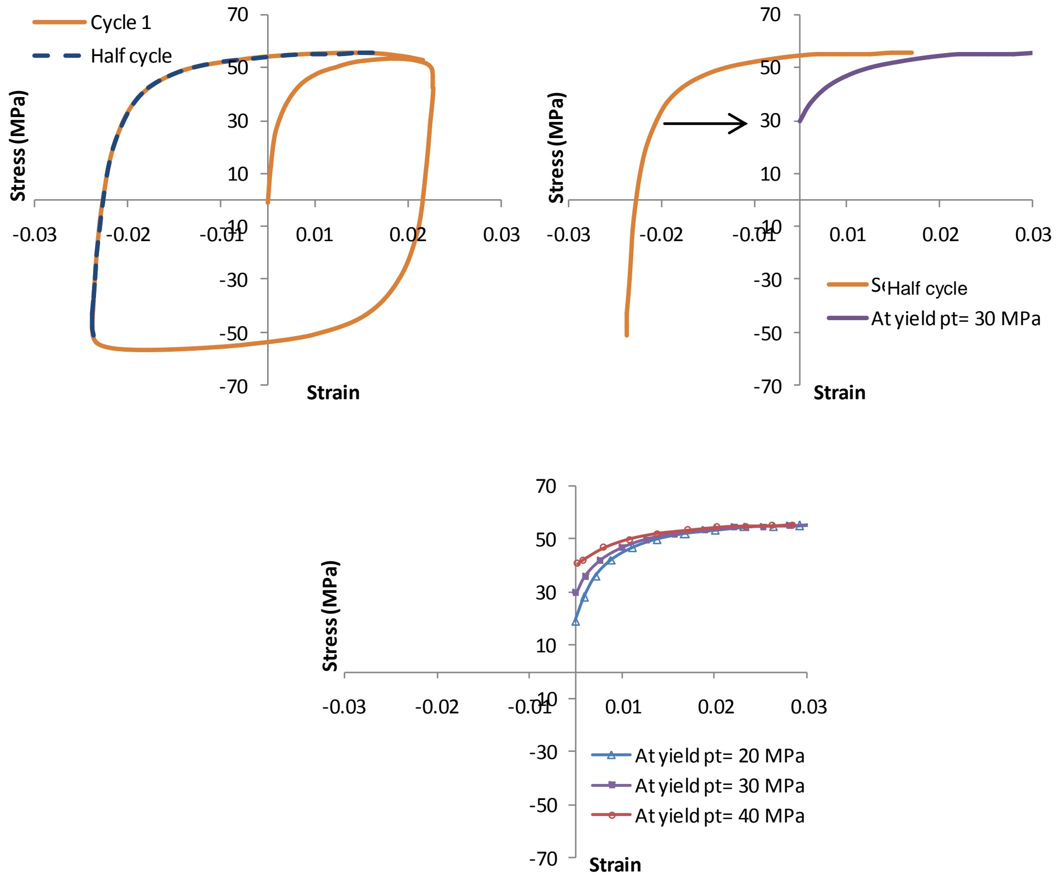

Figure 6.3 (a) First cycle and half cycle of stable hysteresis loop (b) Half cycle and offset half cycle at yield point of 30 MPa (c) Offset half cycles at yield points of 20, 30 and 40 MPa

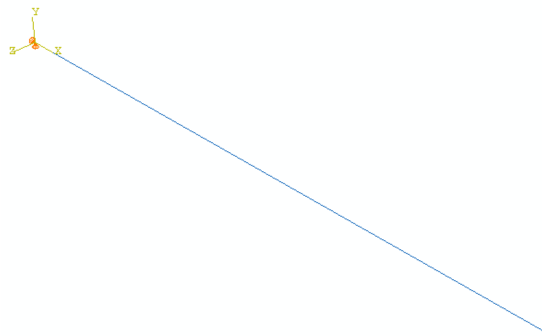

Figure 6.4 Single beam element model for determination of material model parameters

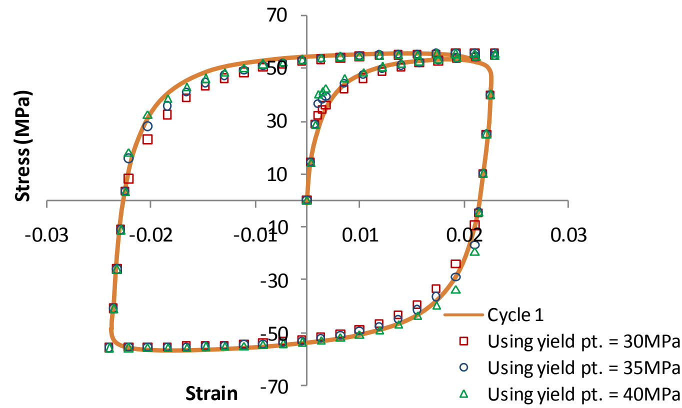

Figure 6.5 Comparison of experimental stress-strain curves with simulations

Table 6.2 Values for C_k and γ_k for various solder alloys and test conditions

Solder Alloy	Strain rate (s^{-1})	Low Strain					Med Strain					High Strain				
		σ_y	α_1		α_2		σ_y	α_1		α_2		σ_y	α_1		α_2	
			C_1	γ_1	C_2	γ_2		C_1	γ_1	C_2	γ_2		C_1	γ_1	C_2	γ_2
SAC305	**0.01**	30	3007	230	1777	3899	30	1472	1001	2655	186	35	3989	218	1621	1800
	0.1	30	815	143	1619	137	35	2772	157	1363	3049	35	843	118	1474	115
SnPb	**0.01**	40	782	768	2407	280	40	1312	232	1423	426	40	663	155	1969	368
	0.1	40	2051	455	1837	217	40	1647	167	2850	429	40	887	150	2695	258
Sn100C	**0.01**	25	3206	867	1014	94	30	1210	131	2411	836	30	1646	506	642	70
	0.1	30	1068	558	1025	68	30	869	62	2804	16139	30	1219	191	344	27

6.4.3 Evaluation of material model

In addition to a comparison involving just the first loading cycle, predictions of the material model were also compared with experimental results to the point of failure. Loading cycles from experiments and simulations of solder alloy SAC305 were selected and are plotted in Fig 6.6. These cycles were selected from the beginning, middle and end of a test. As the number of cycles increases, there are slight deviations between the experimental and simulation curves around the tensile and compressive yield strengths. However, there is good agreement in terms of maximum flow stresses. In general, the material models provide a reasonable description of the material behaviour under the conditions they were tested. Similar plots for all the solder alloys tested, for their particular test conditions, are provided in Appendix C.

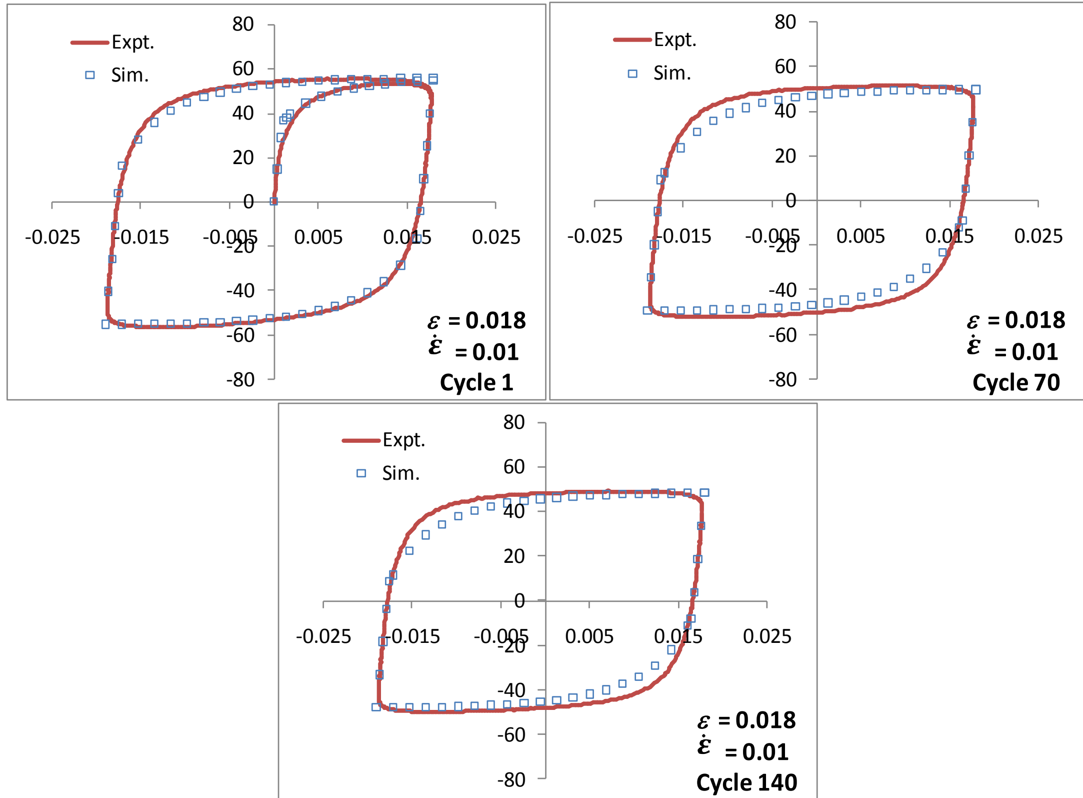

Figure 6.6 Comparison of experimental stress-strain curves with simulations for selected loading cycles

6.5 MODELLING OF VIBRATION OF PRINTED CIRCUIT BOARD

This section demonstrates the application of the material strain-hardening parameters extracted to simulation of board vibration. Experimental data for comparison was obtained from publications by other researchers [55-57].

6.5.1 Details of Model

A printed circuit board with a chip component, both made of FR4 material was modelled using ABAQUS. The component is attached to the board via solder joints. The inner joints are simplified and modelled as cylinders for computational efficiency. The geometry of the critical corner joint was modelled exactly, with its dimensions determined from SEM micrographs of the cross-section of an actual solder joint. Another form of simplification, whereby the critical solder

joint geometry was modelled exactly, while the inner joints were modelled as cuboids instead of cylinders, resulted in only a 1.5% difference in stress values [58, 59]. The quarter finite element model of the board, component and joints, as well as a magnified view of the solder joints are shown in Figs 6.7(a) and (b) respectively. Fig 6.7(c) shows a submodel of the critical corner joint.

The dimensions of the board, components and solder joints are listed in Table 6.3, while the loading and boundary conditions imposed to simulate a 30 Hz vibration of the board are illustrated in Fig 6.8. Quasi-static simulation was undertaken for 10 cycles to compare the effects of using three different material models for the solder – i.e. elastic, elastic-plastic and elastic-cyclic-softening. The material properties for each of these material models are provided in Table 6.4.

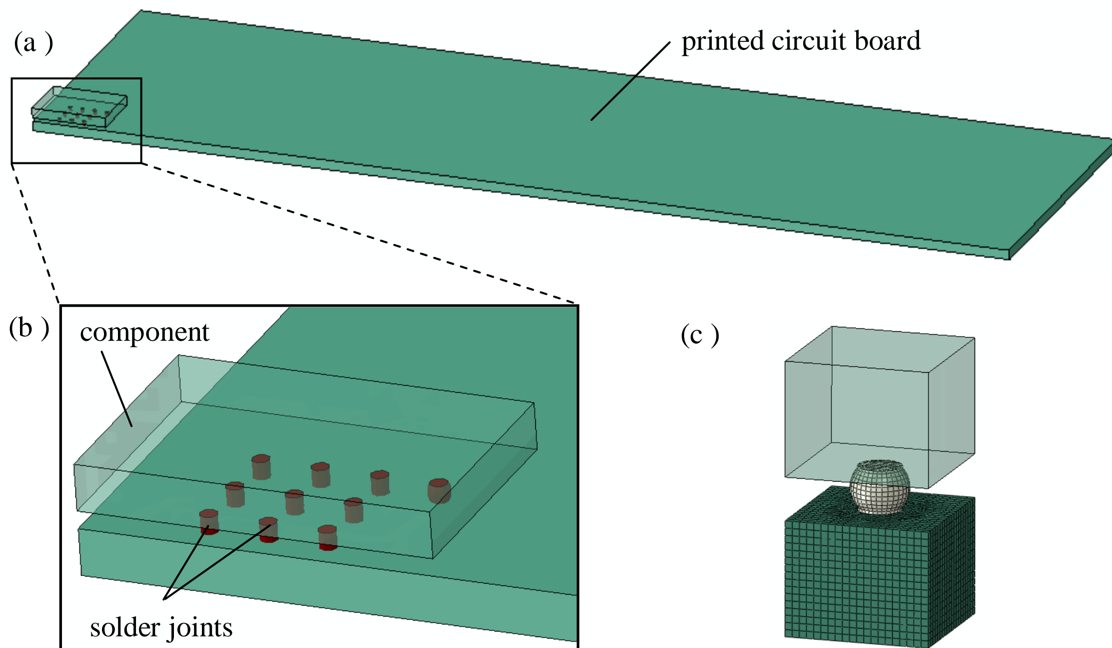

Figure 6.7(a) Finite element model of quarter of printed circuit board with component (b) Magnified view of component, showing solder joints (c) Submodel of critical corner joint

Table 6.3 Dimensions of components in finite element model

Part	Dimensions (mm)
Board	160 x 40 x 0.8
Component	12 x 8 x 0.8
Solder joint	d = 0.4 , h = 0.3

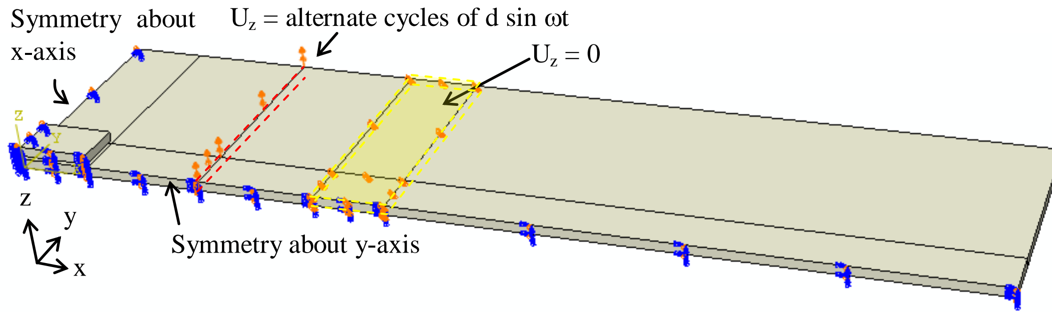

Figure 6.8 Boundary and loading conditions applied to model with d=0.3mm and ω=188.5 rad/s

Table 6.4 Properties for each material model used for SAC305

Material Models		
Elastic	**Elastic-plastic**	**Elastic-cyclic-softening**
E = 54.8 GPa ν = 0.3	E = 54.8 GPa ν = 0.3 σ_y = 40 MPa @ ε_p = 0 σ_y = 43 MPa @ ε_p = 0.01 σ_y = 54 MPa @ ε_p = 0.05 σ_y = 56.5 MPa @ ε_p = 0.1 σ_y = 58 MPa @ ε_p = 0.2	E = 54.8 GPa ν = 0.3 σ_y = 35.1 MPa C_1 = 843.3 MPa, γ_1 = 118.3 C_2 = 1473.8 MPa, γ_2 = 115.1 Q = -9.55 MPa, b = 0.178

6.5.2 Results and Discussion

The loading and boundary conditions applied (see Fig 6.8) resulted in a maximum elastic strain on the board near the critical joint of about 1100 μstrain. The board strain varies with time, as shown in Fig 6.9; this is similar to the experiments with a board strain of 1200 μstrain.

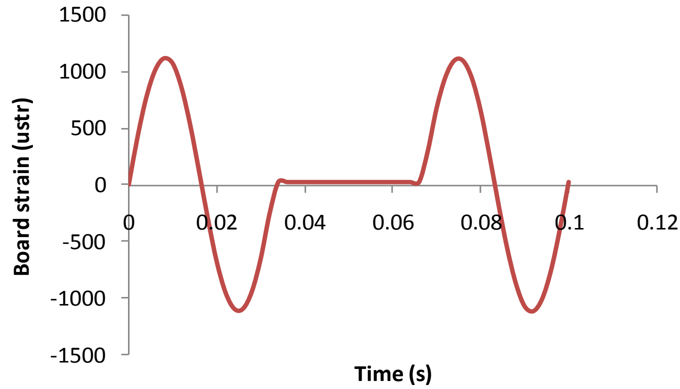

Figure 6.9 Board strain near critical joint, from simulation

When employing submodelling, it is important to ensure that the stress levels between the global model and the submodel are of the same order of magnitude. The von Mises stress contours in the solder joints of the global model and the submodel of the critical joint with elastic-plastic material properties are shown in Fig 6.10. A corresponding contour plot for elastic-cyclic-softening material properties is shown in Fig 6.11. These figures indicate good agreement between the global models and the submodels, with the model based on elastic-plastic material properties having a larger stress compared to the one described by elastic-cyclic-softening.

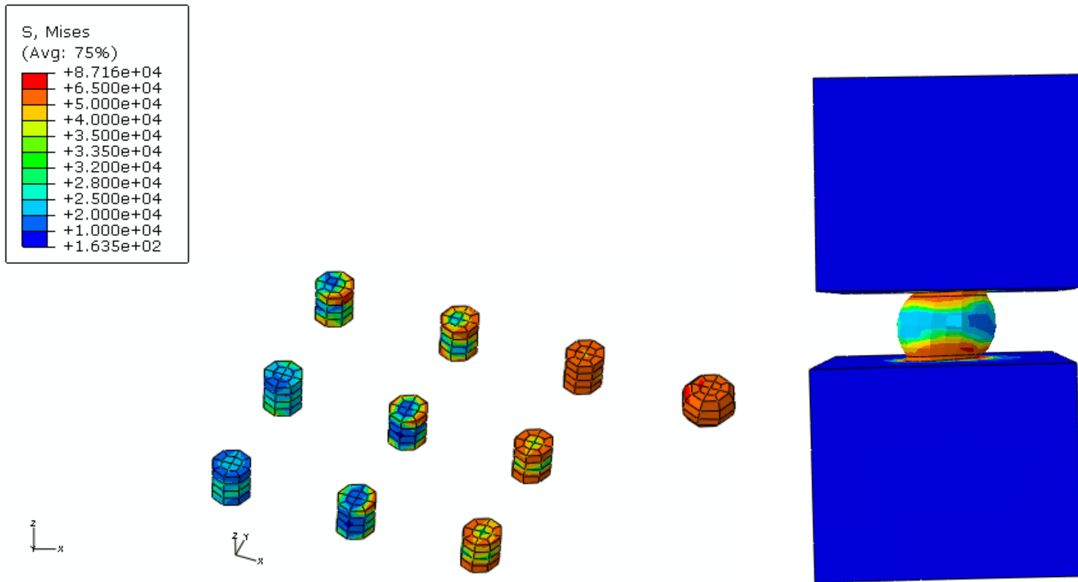

Figure 6.10 von Mises stress in models with elastic-plastic material properties - (a) solder joints of global model and (b) submodel of the critical joint.

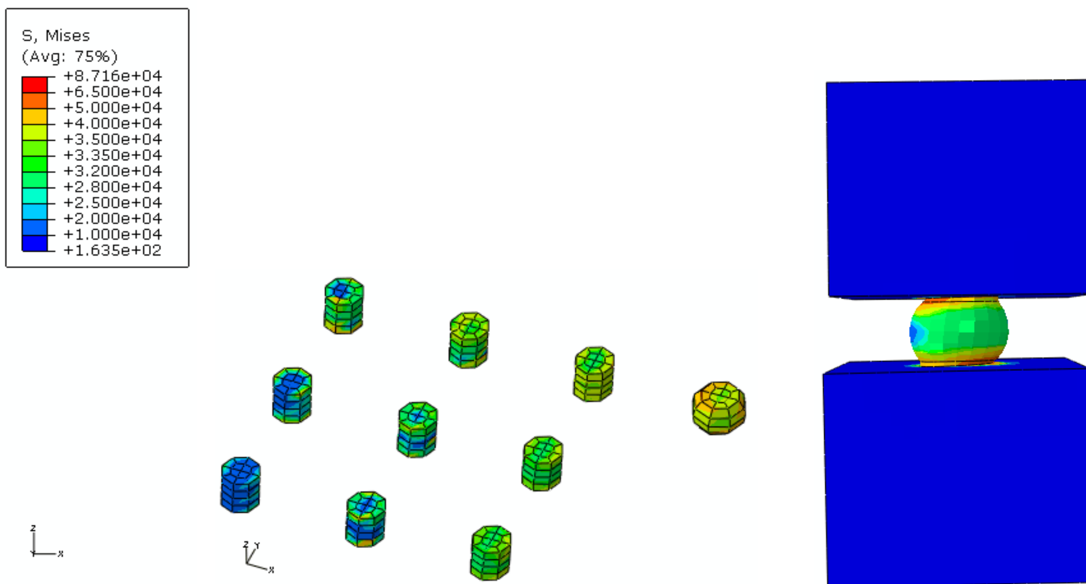

Figure 6.11 von Mises stress in models based on elastic-cyclic-softening material properties - (a) solder joints of global model and (b) submodel of the critical joint.

A comparison of the various stress components obtained from the simulations based on the three material models is shown in Table 6.5. These values were extracted at t=0.667s, which is when the tenth displacement peak occurs. The stress values from the elastic model are significantly

larger than those obtained from the elastic-plastic and elastic-cyclic-softening models. Clearly, this is because of the incorrect assumption that the solder does not yield. A comparison of the stress values obtained from the elastic-perfectly-plastic and elastic-strain-hardening models indicates a percentage difference of about 15-30% for all components of stress, except S13. This difference is significant and increases with time and number of loading cycles, as shown in Fig 6.12, which describes the peeling stress (S33).

Table 6.5 Stress components (MPa) from simulations based on three material models. Percentage difference between values based on elastic-plastic behaviour and elastic-cyclic-softening material properties are also listed

	t=0.667			
Material model	**Elastic**	**Elastic-plastic**	**Elastic-cyclic-softening**	**% diff.**
Mises Stress	786.3	72.3	54.7	-24.3
S11	307.0	93.6	75.1	-19.7
S22	197.2	93.0	74.2	-20.2
S33	633.5	112.1	96.3	-14.1
S12	57.0	23.2	15.6	-33.0
S13	29.8	21.2	23.0	8.3
S23	89.1	25.6	17.7	-31.0

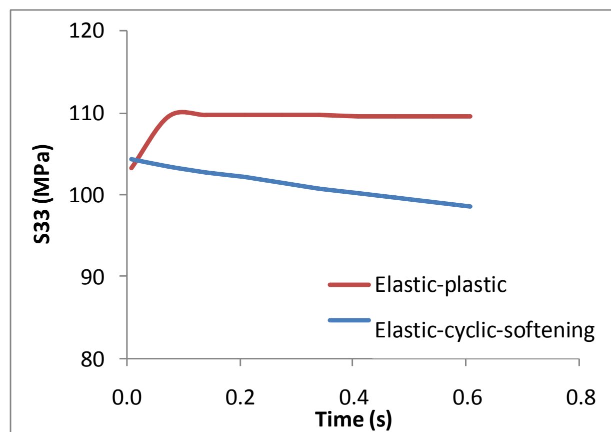

Figure 6.12 Evolution of peeling stress with time and loading cycles for models with elastic-perfectly-plastic and elastic-strain-hardening material properties

In summary, the elastic-cyclic-softening parameters for three solder alloys were extracted from experimental cyclic stress-strain curves and are presented in Tables 6.1 and 6.2. The use of these parameters has been demonstrated via simulation of solder joints in a vibrating board, and a comparison of elastic-plastic and elastic-cyclic-softening materials has been undertaken. A significant difference in stress values, ranging from 15-30%, for results based on the two material models is observed, indicating that the cyclic softening behaviour of solder is significant and should be taken into account in finite element modelling of solder joints.

Chapter 7

CONCLUSION

As set out in the objectives, the strength, stiffness and fatigue properties of three solder alloys (SAC305, Sn100C and SnPb) have been characterised in this study. Subsequently, these properties were incorporated into a finite element model of a vibrating printed circuit board. Some important conclusions from this study are highlighted below.

Solder samples were carefully prepared through a process of melting, casting and quenching, so that the microstructure of the resulting bulk samples was similar to that in solder joints. This was verified qualitatively through comparisons of scanning electron microscope images of these samples with those of actual solder joints. Quantitative comparisons determined from Vickers microhardness test were also carried out. The results indicated that difference in microhardness between solder joints and the cast samples was only 10-15 %, confirming that the microstructure of the cast ingots was similar to that in solder joints.

Dog bone shaped bulk solder samples were subjected to uniaxial tension and compression tests to determine the Young's modulus, yield strength and flow stress. The tensile and compressive material properties were found to be similar. SAC305 is the stiffest alloy in terms of microhardness, Young’s modulus and flow stress; Sn100C and SnPb are generally softer, with

SnPb having the lowest microhardness and Young's modulus. Sn100C has the lowest yield strength and flow stress.

Characterization of fatigue properties was carried out at three strain amplitudes and two strain rates. Unlike most metallic materials which ultimately attain a stable cyclic response, the peak stresses in solder decrease gradually initially, then more sharply once a crack is initiated. It was found that the solder materials studied undergo isotropic softening and kinematic hardening. Both lead-free and eutectic tin-lead solders exhibit cyclic softening, while strain hardening in lead-free solder is more pronounced than that in SnPb solder. The profile and size of the hysteresis curve change in different ways for lead-free solder alloys and SnPb. Comparisons between the solder alloys, on the basis of the Talypov constant to quantify the extent of kinematic hardening in the samples was also carried out. It was found that the extent of kinematic hardening in solder increases with the cyclic strain amplitude applied. It was also ascertained that the hardening properties of solder are rate-dependant. In addition, Sn100C and SAC305 exhibit a larger degree of kinematic hardening than SnPb.

The S-N curves of the solder alloys indicate a longer fatigue life, in terms of number of cycles to failure, for higher strain rates. However, with regard to time to failure, samples loaded at lower strain rates last longer. Sn100C has the longest life, followed by SAC305 and SnPb, for both strain rates examined.

Cyclic stress-strain curves were further analysed to extract isotropic softening and kinematic hardening material parameters. The use of these parameters was demonstrated via simulations of solder joints in a vibrating board, and a comparison of elastic-plastic and elastic-cyclic-softening material properties undertaken. A significant difference in stress values, ranging from 15-30%, for results based on the two different material models was observed, indicating that the cyclic softening behaviour of solder is significant and should be taken into account in finite element modelling of solder joints.

BIBLIOGRAPHY

1. Lee, C.C., et al., *Are intermetallics in solder joints really brittle?*, in *57th Electronic Components & Technology Conference, 2007 Proceedings*. 2007. p. 648-652.
2. Wong, E.H., et al., *Drop Impact Test - Mechanics and Physics of Failure*, in *4th Electronic Packaging & Technology Conference, 2002 Proceedings*. 2002. p. 327-333.
3. Wong, E.H., S.K.W. Seah, and V.P.W. Shim, *A review of board level solder joints for mobile applications.* Microelectronics Reliability, 2008. **48**(11-12): p. 1747-1758.
4. JEDEC, *Board Level Drop Test Method of Components for Handheld Electronic Products*, in *Standard JESD22-B111*. 2003.
5. Newman, K. *Board-level solder joint reliability of high performance computers under mechanical loading*. in *9th International Conf. on Thermal, Mechanical and Multiphysics Simulation and Experiments in Micro-Electronics and Micro-Systems, EuroSimE 2008*. 2008. Freiburg, Germany.
6. Reiff, D. and E. Bradley, *A novel mechanical shock test method to evaluate lead-free BGA solder joint reliability*, in *55th Electronic Components & Technology Conference, 2005 Proceedings*. 2005. p. 1519-25.
7. Varghese, J. and A. Dasgupta, *Test methodology for durability estimation of surface mount interconnects under drop testing conditions.* Microelectronics Reliability, 2007. **47**(1): p. 93-103.
8. Seah, S.K.W., et al. *High-speed bend test method and failure prediction for drop impact reliability*. in *Electronic Components and Technology Conference, 2006. Proceedings. 56th*. 2006.
9. Marjamaki, P., T.T. Mattila, and J.K. Kivilahti. *A comparative study of the failure mechanisms encountered in drop and large amplitude vibration tests*. in *Electronic Components and Technology Conference, 2006. Proceedings. 56th*. 2006.
10. Pringle, T., et al., *Solder joint reliability of BGA package under end-user handling test conditions*, in *57th Electronic Components & Technology Conference, 2007 Proceedings*. 2007. p. 400-406.
11. Luan, J.-E. and T.Y. Tee. *Novel board level drop test simulation using implicit transient analysis with input-G method*. in *Electronics Packaging Technology Conference, 2004. EPTC 2004. Proceedings of 6th*. 2004.
12. Tee, T.Y., J.-E. Luan, and H.S. Ng. *Development and application of innovational drop impact modeling techniques*. in *Electronic Components and Technology Conference, 2005. Proceedings. 55th*. 2005.
13. Tee, T.Y., et al. *Advanced experimental and simulation techniques for analysis of dynamic responses during drop impact*. in *Electronic Components and Technology Conference, 2004. Proceedings. 54th*. 2004.
14. Yeh, C.L. and Y.S. Lai, *Support excitation scheme for transient analysis of JEDEC board-level drop test.* Microelectronics Reliability, 2006. **46**(2-4): p. 626-636.
15. Yeh, C.-L., Y.-S. Lai, and C.-L. Kao, *Evaluation of board-level reliability of electronic packages under consecutive drops.* Microelectronics and Reliability, 2006. **46**(7): p. 1172-1182.

16. Syed, A., et al., *Plastic deformation and life prediction of solder joints for mechanical shock and drop/impact loading conditions*, in *57th Electronic Components & Technology Conference, 2007 Proceedings*. 2007. p. 507-514.

17. Luan, J.E., et al., *Drop impact life prediction models with solder joint failure modes and mechanisms*, in *Proceedings of the 7th Electronics Packaging Technology Conference, Vols. 1 and 2*, Y.C. Mui, et al., Editors. 2005. p. 66-72.

18. Yeh, C.-L., Y.-S. Lai, and C.-L. Kao. *Prediction of board-level reliability of chip-scale packages under consecutive drops*. in *Electronic Packaging Technology Conference, 2005. EPTC 2005. Proceedings of 7th*. 2005.

19. Ma, H. and J.C. Suhling, *A review of mechanical properties of lead-free solders for electronic packaging.* Journal of Materials Science, 2009. **44**(5): p. 1141-1158.

20. Plumbridge, W.J. and C.R. Gagg, *Effects of strain rate and temperature on the stress-strain response of solder alloys.* Journal of Materials Science-Materials in Electronics, 1999. **10**(5-6): p. 461-468.

21. Shi, X.Q., et al., *Effect of temperature and strain rate on mechanical properties of 63Sn/37Pb solder alloy.* Journal of Electronic Packaging, 1999. **121**(3): p. 179-185.

22. Shohji, I., et al., *Comparison of low-melting lead-free solders in tensile properties with Sn-Pb eutectic solder.* Journal of Materials Science-Materials in Electronics, 2004. **15**(4): p. 219-223.

23. Qin, F., et al., *Tensile Behaviors of Lead-Containing and Lead-Free Solders at High Strain Rates.* Journal of Electronic Packaging, 2009. **131**(3).

24. Siviour, C.R., et al., *Mechanical properties of SnPb and lead-free solders at high rates of strain.* Journal of Physics D-Applied Physics, 2005. **38**(22): p. 4131-4139.

25. Wong, E.H., et al., *Stress-strain characteristics of tin-based solder alloys for drop-impact modeling.* Journal of Electronic Materials, 2008. **37**(6): p. 829-836.

26. Cutiongco, E.C., Vaynman, S., Fine, M. E., Jeannotte, D. A., *Isothermal Fatigue of 63Sn-37Pb Solder.* Journal of Electronic Packaging, 1990. **112**: p. 5.

27. Guo, Q., Cutiongco, E. C., Keer, L. M., Fine, M. E., *Thermomechanical Fatigue Life Prediction of 63Sn/37Pb Solder.* Journal of Electronic Packaging, 1992. **114**: p. 7.

28. Kanchanomai, C., Y. Miyashita, and Y. Mutoh, *Low cycle fatigue behavior and mechanisms of a eutectic Sn-Pb solder 63Sn/37Pb.* International Journal of Fatigue, 2002. **24**(6): p. 671-683.

29. Shi, X.Q., et al., *Low cycle fatigue analysis of temperature and frequency effects in eutectic solder alloy.* International Journal of Fatigue, 2000. **22**(3): p. 217-228.

30. Vaynman, S., *Effect of Strain Rate on Fatigue of Low-Tin Based Solder.* Ieee Transactions on Components Hybrids and Manufacturing Technology, 1989. **12**(4): p. 469-472.

31. Kanchanomai, C., Y. Miyashita, and Y. Mutoh, *Strain-rate effects on low cycle fatigue mechanism of eutectic Sn-Pb solder.* International Journal of Fatigue, 2002. **24**(9): p. 987-993.

32. Kanchanomai, C. and Y. Mutoh, *Effect of temperature on isothermal low cycle fatigue properties of Sn-Ag eutectic solder.* Materials Science and Engineering A, 2004. **381**(1-2): p. 113-120.

33. Kanchanomai, C., et al., *Low cycle fatigue test for solders using non-contact digital image measurement system.* International Journal of Fatigue, 2002. **24**(1): p. 57-67.

34. ASTM, *Standard practice for strain controlled fatigue testing*, in *Standard E606*. 1998, ASTM International.

35. Coffin, J.L.F., *A Study of the Effects of Cyclic Thermal Stresses on a Ductile Material.* Trans. Am. Soc. Mech. Eng., 1954. **76**: p. 931.

36. Manson, S.S., *Fatigue: a complex subject-some simple approximations.* Experimental Mechanics, 1965. **5**: p. 193-226.

37. Amagai, M., et al., *Mechanical characterization of Sn-Ag-based lead-free solders.* Microelectronics Reliability, 2002. **42**(6): p. 951-966.

38. Kariya, Y. and M. Otsuka, *Mechanical fatigue characteristics of Sn-3.5Ag-X (X = Bi, Cu, Zn and In) solder alloys.* Journal of Electronic Materials, 1998. **27**(11): p. 1229-1235.

39. Pang, J.H.L., B.S. Xiong, and T.H. Low, *Low cycle fatigue study of lead free 99.3Sn-0.7Cu solder alloy.* International Journal of Fatigue, 2004. **26**(8): p. 865-872.

40. Pang, J.H.L., et al., *Creep and fatigue characterization of lead free 95.5Sn-3.8Ag-0.7Cu solder*, in *54th Electronic Components & Technology Conference, Vols 1 and 2, Proceedings*. 2004. p. 1333-1337.

41. Xiao, W., et al., *Effect of rare earth on mechanical creep-fatigue property of SnAgCu solder joint.* Journal of Alloys and Compounds, 2009. **472**(1-2): p. 198-202.

42. Bonnaud, E.L., Gudmundson, P. *Lead-Free Solder Cyclic Plasticity Characterization for Drop Test Simulations*. in *7th International Conf. on Thermal, Mechanical and Multiphysics Simulation and Experiments in Micro-Electronics and Micro-Systems, EuroSimE 2006*. 2006. Como, Italy.

43. Lauro, P., et al., *Effects of mechanical deformation and annealing on the microstructure and hardness of Pb-free solders.* Journal of Electronic Materials, 2003. **32**(12): p. 1432-1440.

44. Ochoa, F., J.J. Williams, and N. Chawla, *Effects of cooling rate on the microstructure and tensile behavior of a Sn-3.5wt.%Ag solder.* Journal of Electronic Materials, 2003. **32**(12): p. 1414-1420.

45. Wong, E.H., et al., *Stress-strain characteristics of tin-based solder alloys at medium strain rate.* Materials Letters, 2008. **62**(17-18): p. 3031-3034.

46. Sharpe, W.N., *Springer Handbook of Experimental Solid Mechanics*.

47. Kang, S.K., Lauro, P.A., Shih, D.-Y., Henderson,D. W., Puttlitz, K. J. , *Microstructure and mechanical properties of lead-free solder and solder joints used in microelectronic applications.* IBM Journal of Research & Development, 2005. **49**(4/5): p. 14.

48. Seo, S.K., et al., *The evolution of microstructure and microhardness of Sn-Ag and Sn-Cu solders during high temperature aging.* Microelectronics Reliability, 2009. **49**(3): p. 288-295.

49. *ASM Handbook*. Fatigue and Fracture. Vol. 19: ASM International.

50. Kanchanomai, C., Y. Miyashita, and Y. Mutoh, *Low-cycle fatigue behavior of Sn-Ag, Sn-Ag-Cu, and Sn-Ag-Cu-Bi lead-free solders.* Journal of Electronic Materials, 2002. **31**(5): p. 456-465.

51. Kanchanomai, C., et al., *Influence of frequency on low cycle fatigue behavior of Pb-free solder 96.5Sn-3.5Ag.* Materials Science and Engineering A, 2003. **345**(1-2): p. 90-98.

52. Kanchanomai, C. and Y. Mutoh, *Temperature effect on low cycle fatigue behavior of Sn-Pb eutectic solder.* Scripta Materialia, 2004. **50**(1): p. 83-88.

53. Skrzypek, J.J., *Plasticity and Creep - Theory, Examples and Problems*. 1993: CRC Press, Inc.

54. *ABAQUS Documentation Version 6.8 EF1.*

55. Wong, E.H., et al., *High-Speed Cyclic Bend Tests and Board-Level Drop Tests for Evaluating the Robustness of Solder Joints in Printed Circuit Board Assemblies.* Journal of Electronics Materials, 2009. **38**(6): p. 884-895.

56. Wong, E.H., et al., *Advances in the drop-impact reliability of solder joints for mobile applications.* Microelectronics Reliability, 2009. **49**(2): p. 139-149.

57. Zhao, X.J., et al. *Frequency Dependant S-N Curves for Predicting Drop Impact Robustness of Pb-fee Solder Interconnects*. in *Electronic Components and Technology Conference, 2009. Proceedings. 59th*. 2009.

58. Syed, A., *Predicting Solder Joint Reliability for Thermal, Power & Bend Cycle within 25% Accuracy*, in *51st Electronic Components & Technology Conference, 2007 Proceedings*. 2001.

59. Syed, A., Kim., S. B., Lin, W., *Building Accuracies in Finite Element Models for Life Prediction of Solder Joints*, in *9th Electronic Packaging & Technology Conference, 2002 Proceedings*. 2007. p. 184-191.

Appendix A

EXPERIMENTAL CYCLIC STRESS-STRAIN CURVES

A.1 SAC305 SOLDER ALLOY

A.1.1 Low strain amplitude and low strain rate

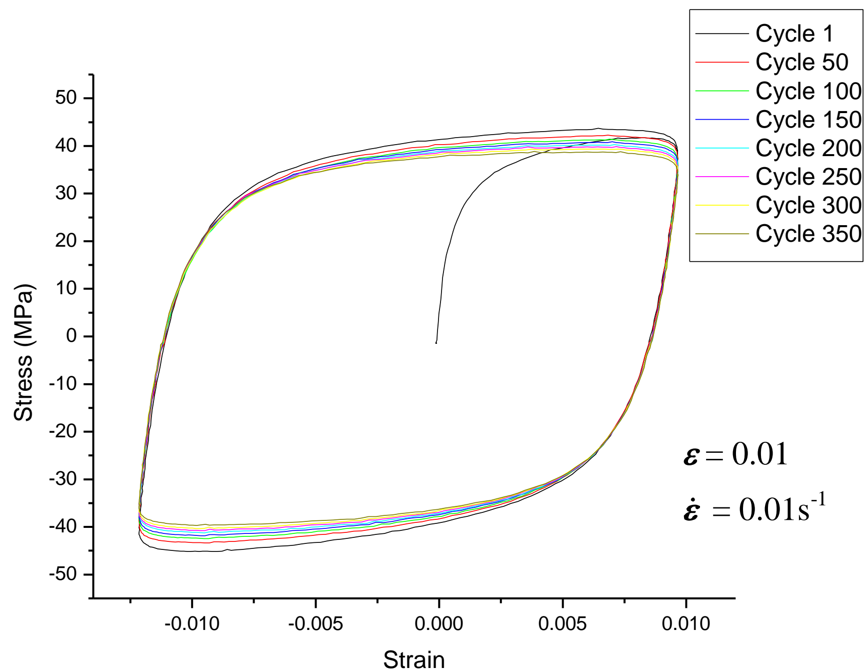

A.1.2 High strain amplitude and low strain rate

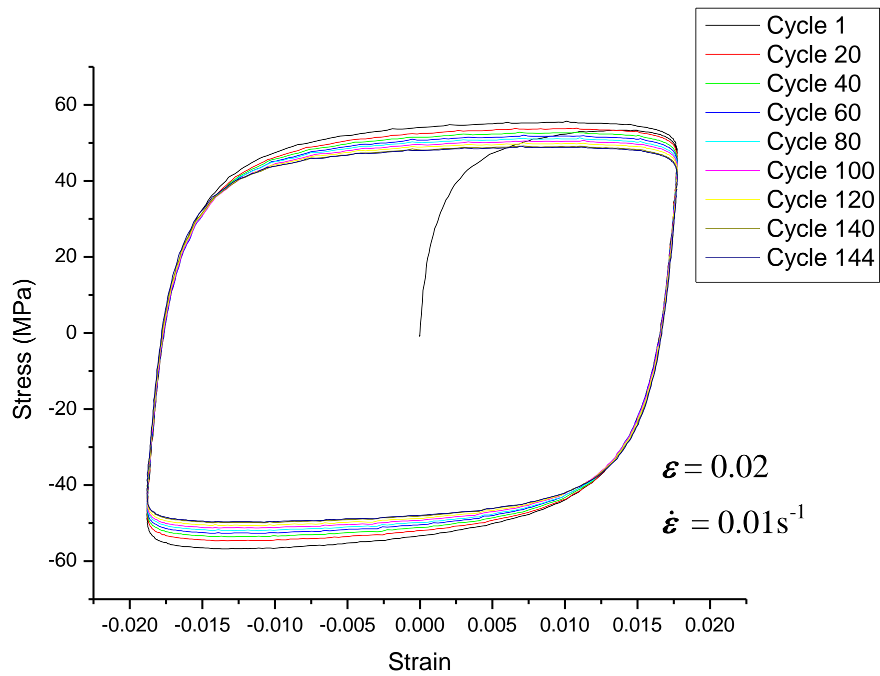

A.1.3 Low strain amplitude and high strain rate

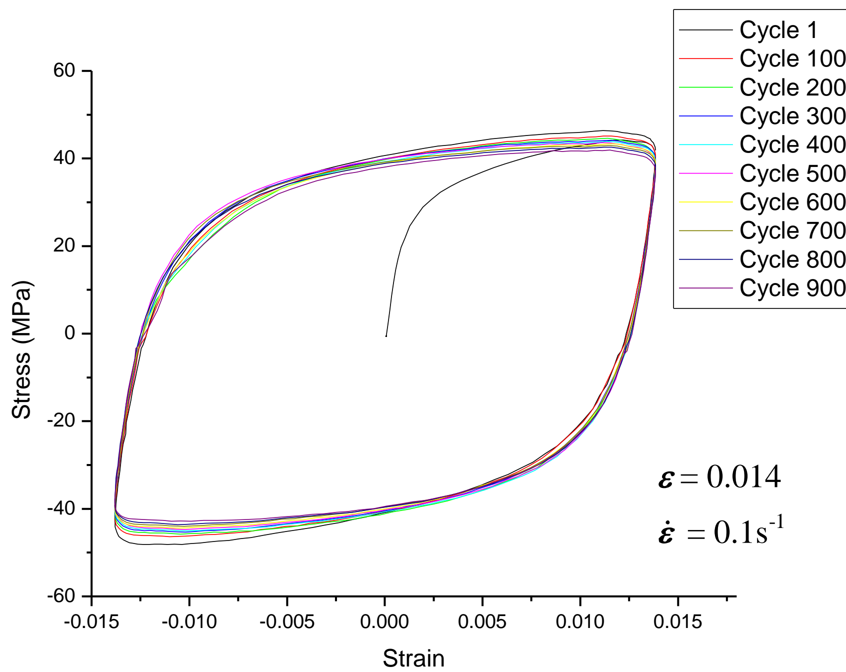

A.1.4 High strain amplitude and high strain rate

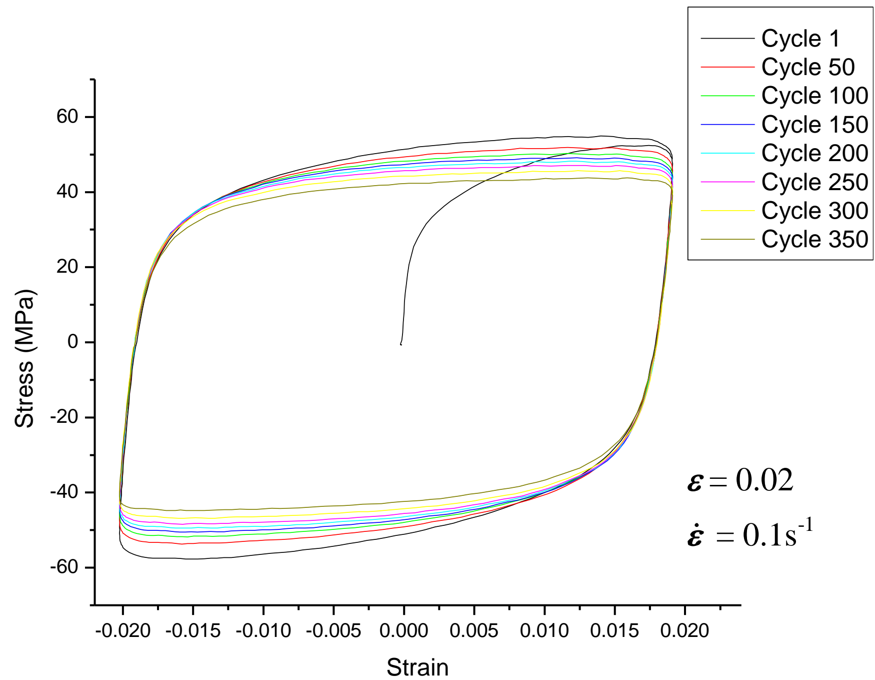

A.2 SnPb Solder Alloy

A.2.1 Low strain amplitude and low strain rate

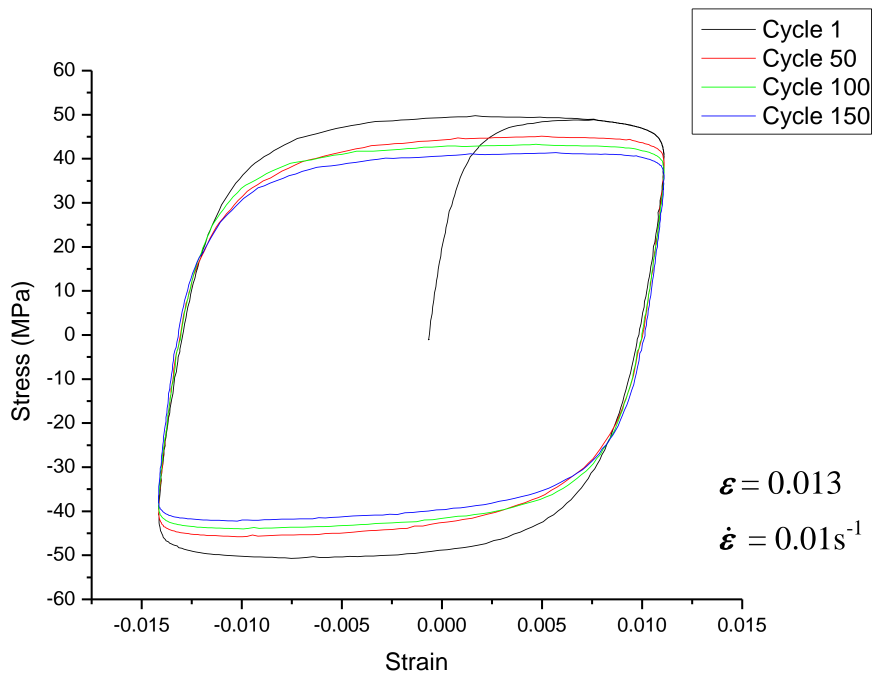

A.2.2 High strain amplitude and low strain rate

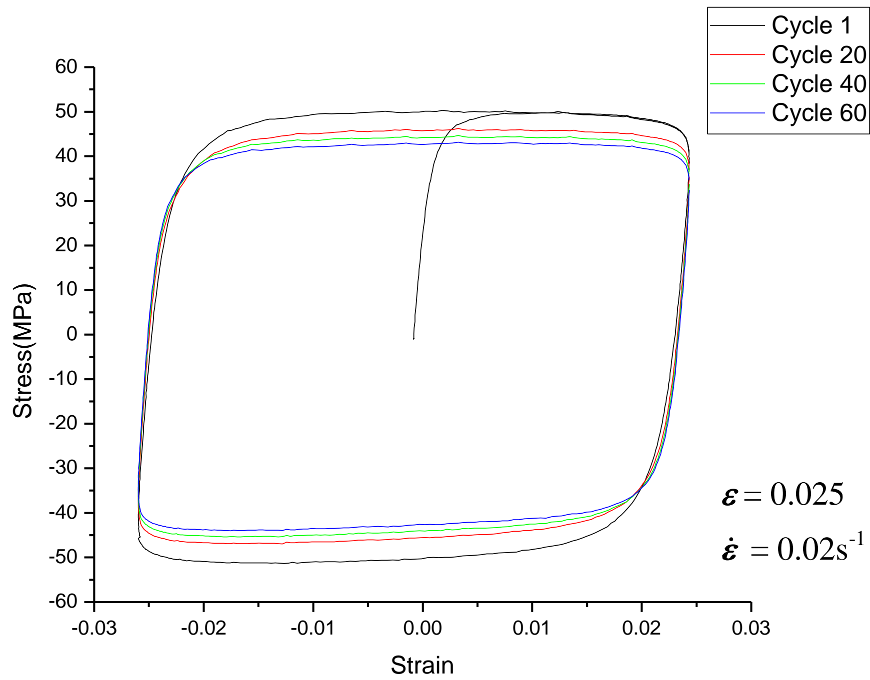

A.2.3 Low strain amplitude and high strain rate

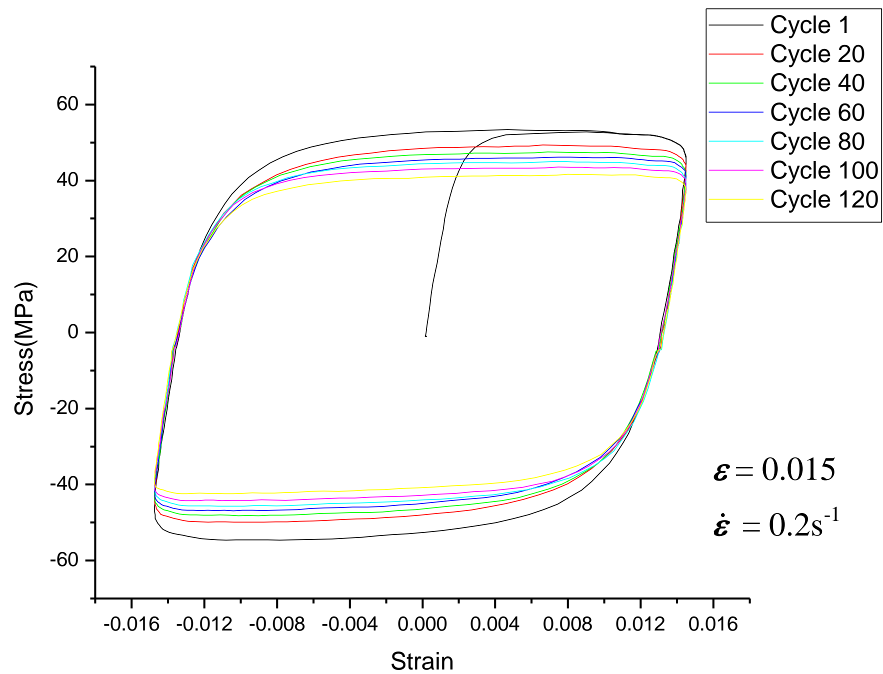

A.2.4 High strain amplitude and high strain rate

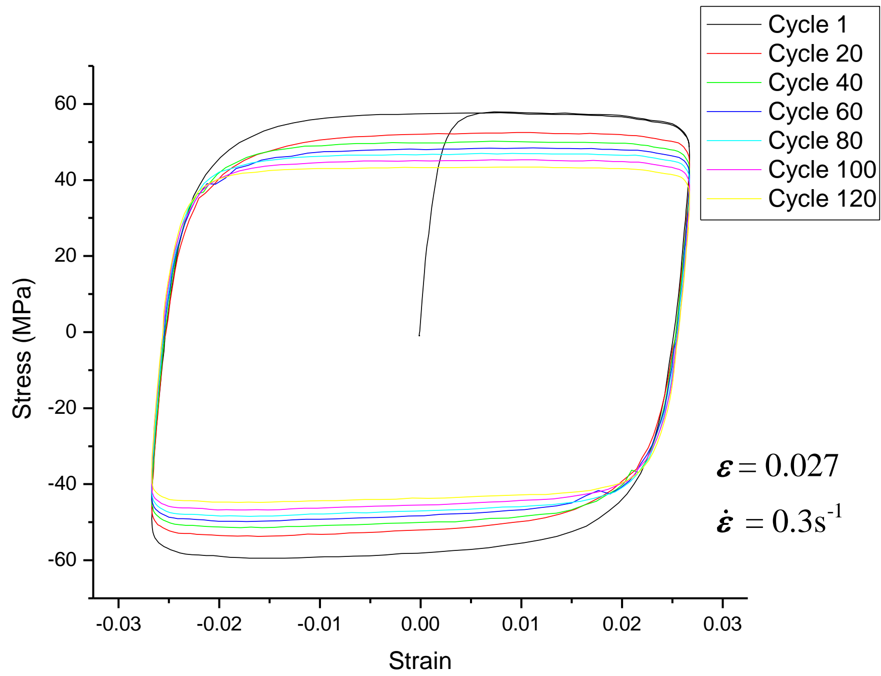

A.3 SN100C SOLDER ALLOY

A.3.1 Low strain amplitude and low strain rate

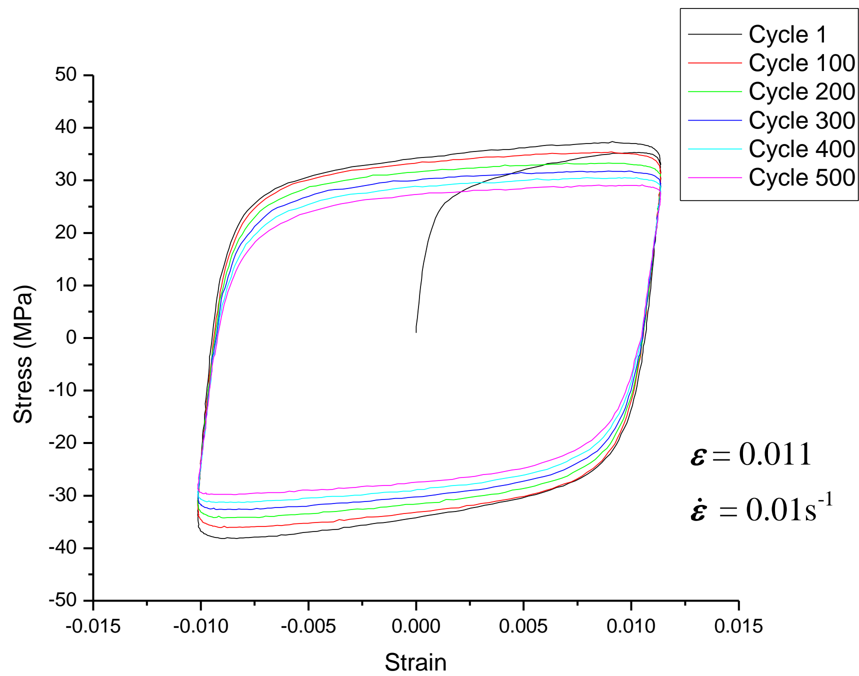

A.3.2 High strain amplitude and low strain rate

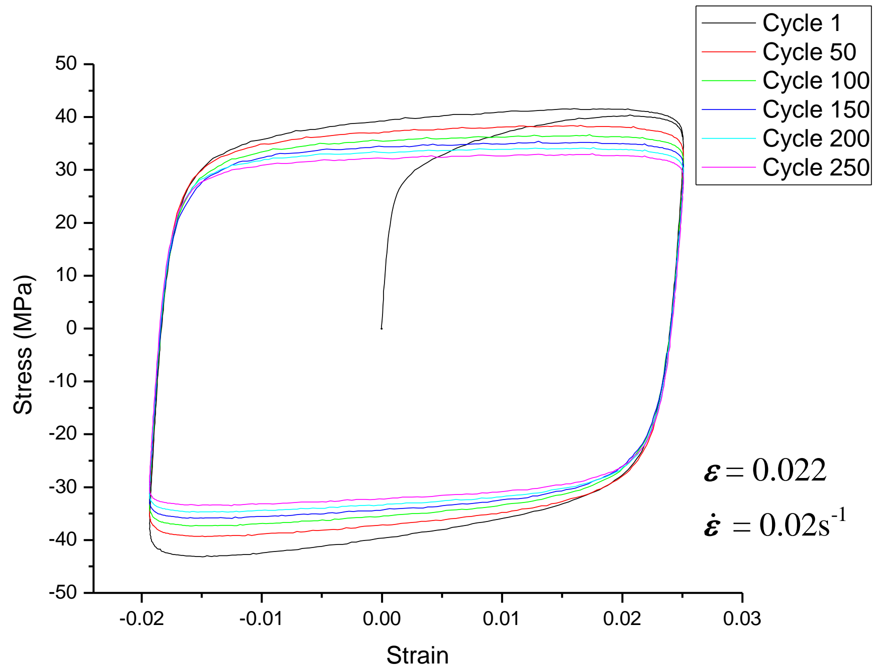

A.3.3 Low strain amplitude and high strain rate

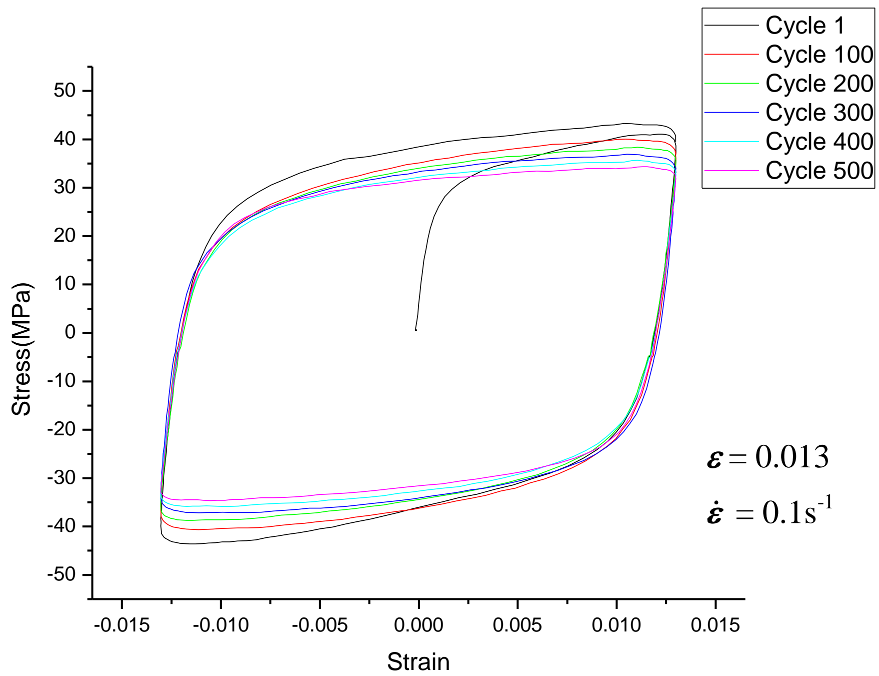

A.3.4 High strain amplitude and high strain rate

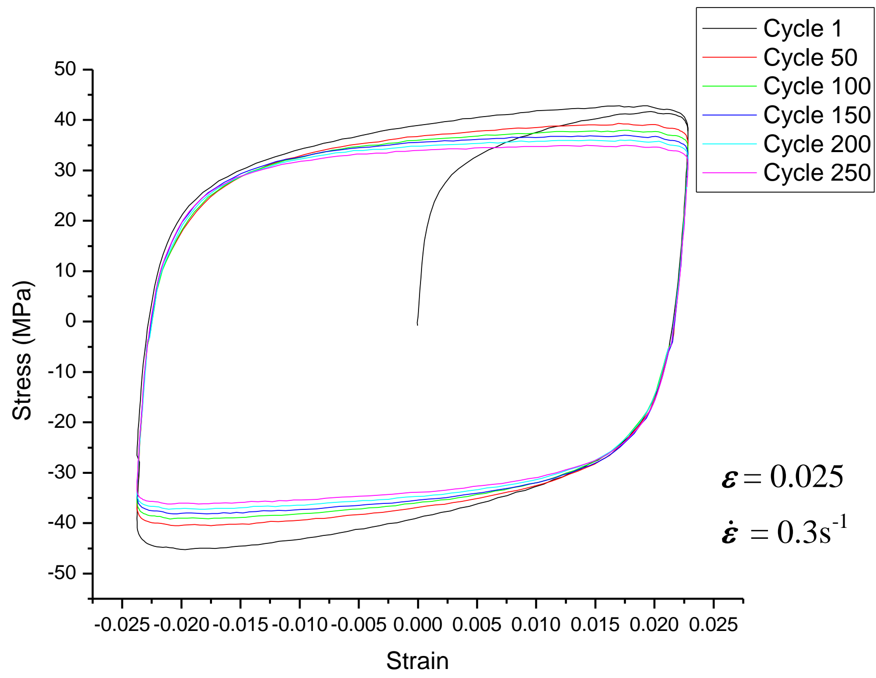

Appendix B

COMPARISON BETWEEN EXPERIMENTAL STRESS-STRAIN CURVES AND FEM SIMULATION RESULTS

B.1 SAC305 Solder Alloy

B.1.1 Low strain amplitude and low strain rate

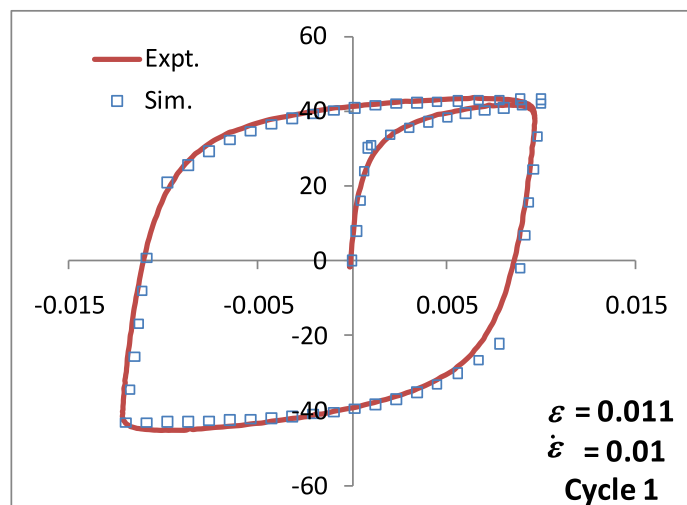

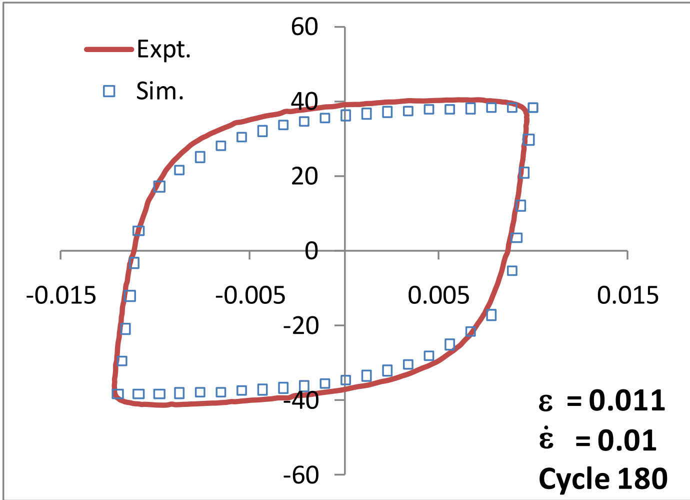
Expt.
Sim.
60
40
20
0
-20
-40
-60
-0.015
-0.005
0.005
0.015
ε = 0.011
ε̇ = 0.01
Cycle 180

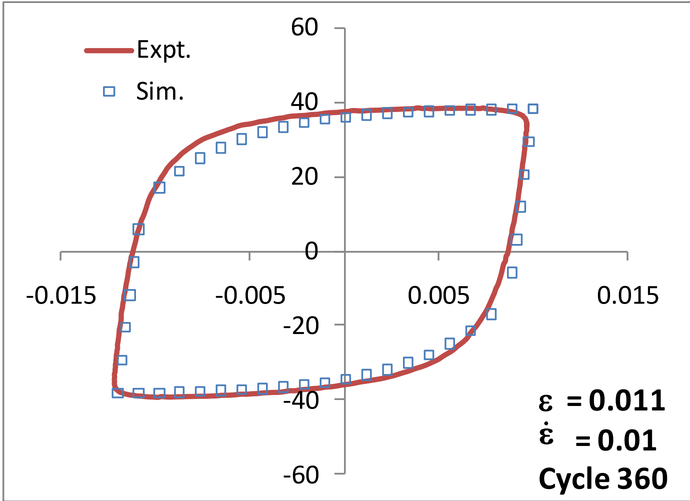
Expt.
Sim.
60
40
20
0
-20
-40
-60
-0.015
-0.005
0.005
0.015
ε = 0.011
ε̇ = 0.01
Cycle 360

B.1.2 Medium strain amplitude and low strain rate

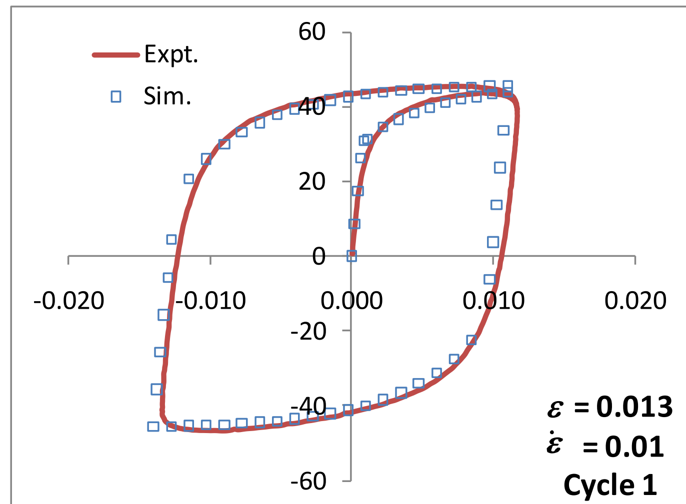

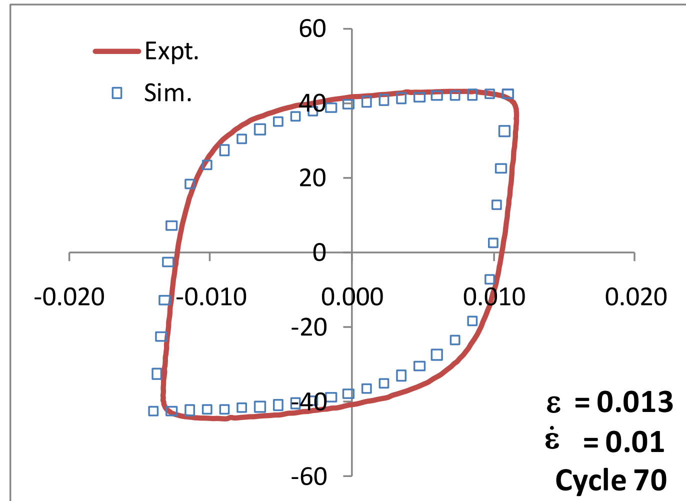

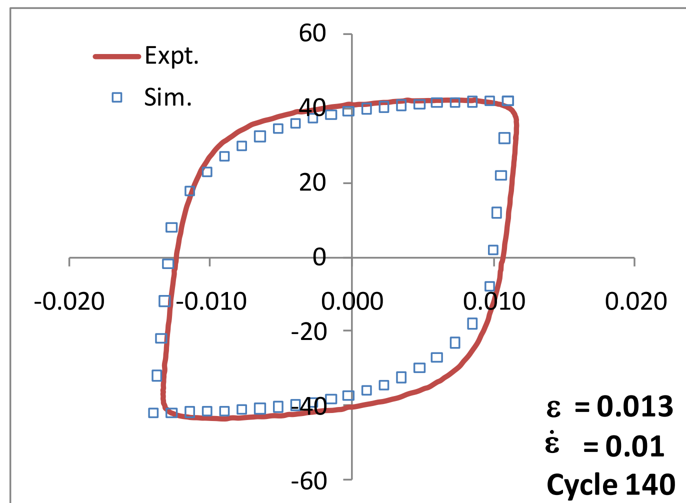

B.1.3 High strain amplitude and low strain rate

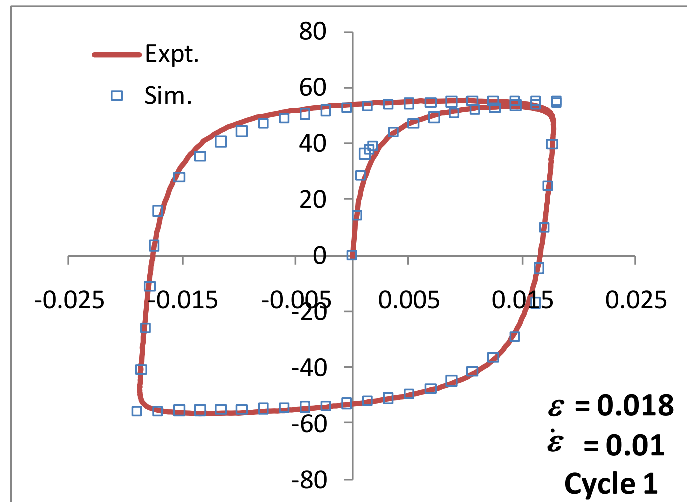

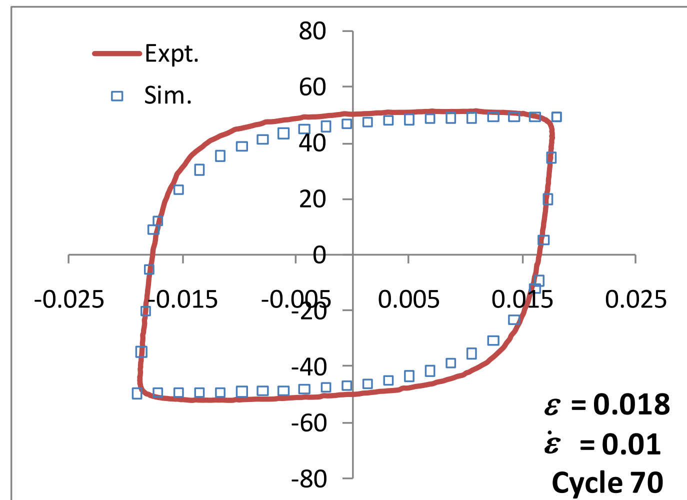

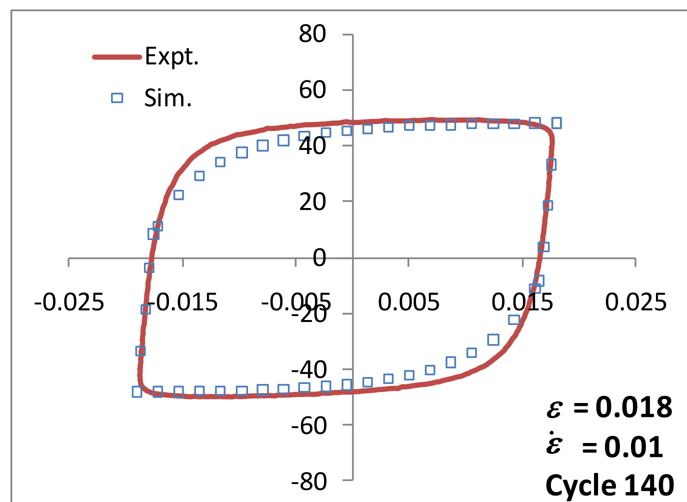

B.1.4 Low strain amplitude and high strain rate

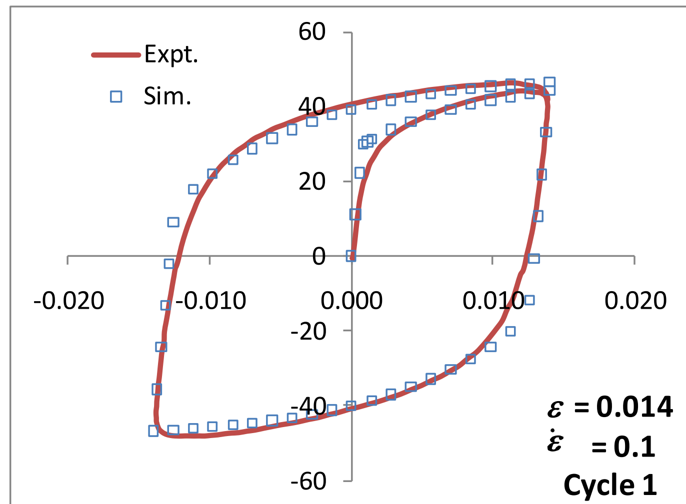

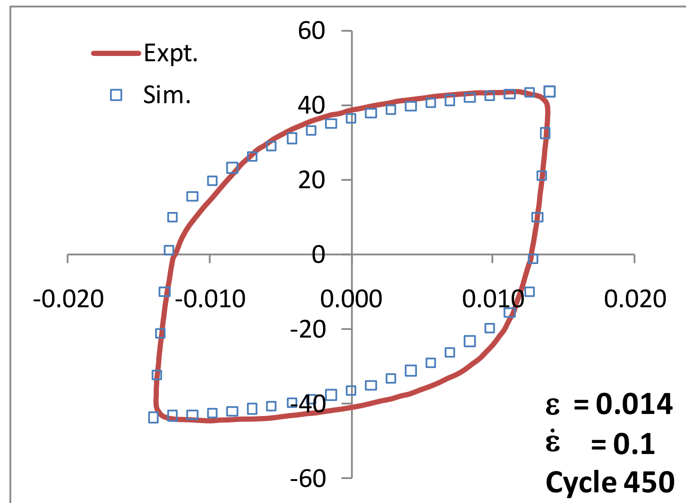

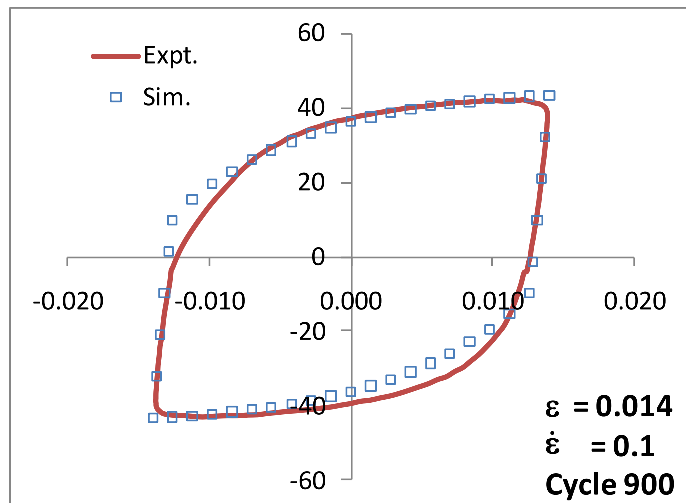

B.1.5 Medium strain amplitude and high strain rate

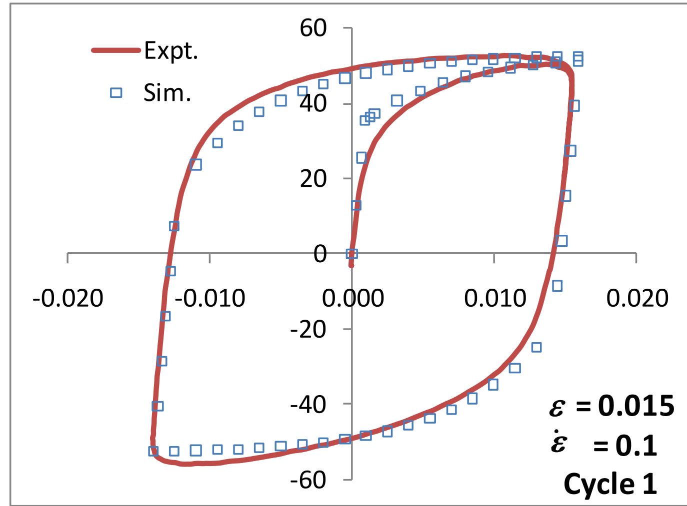

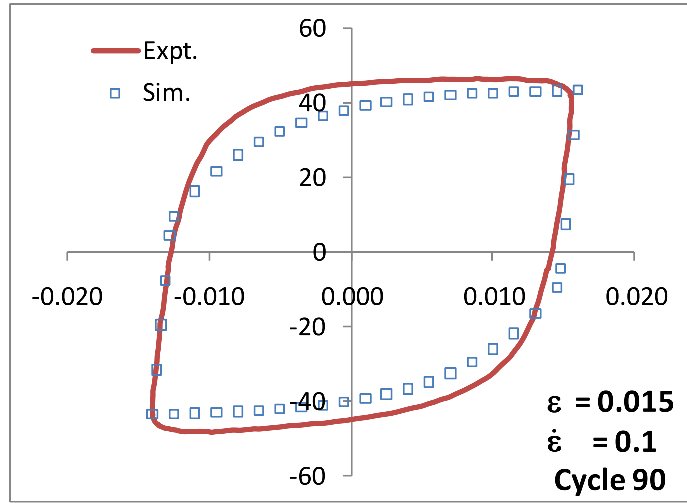

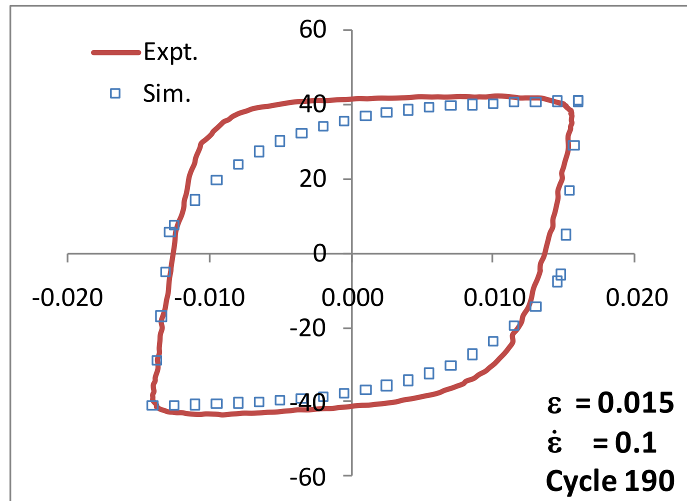

B.1.6 High strain amplitude and high strain rate

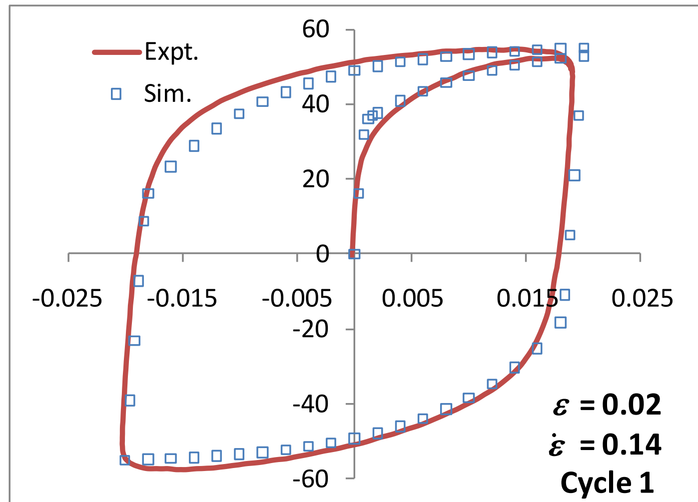

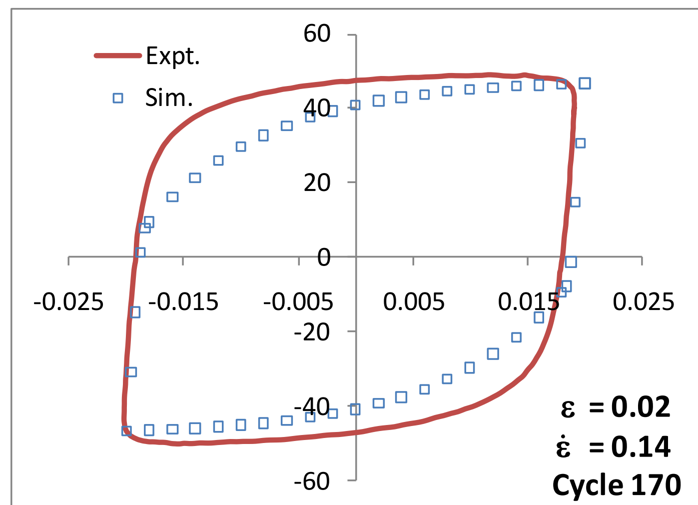

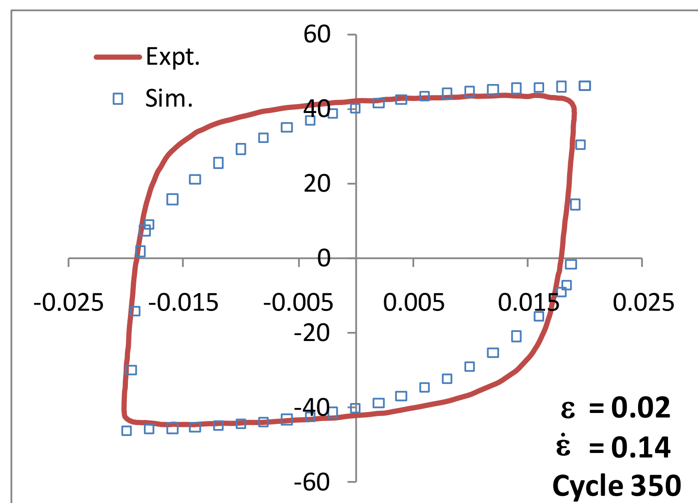

B.2 SnPb Solder Alloy

B.2.1 Low strain amplitude and low strain rate

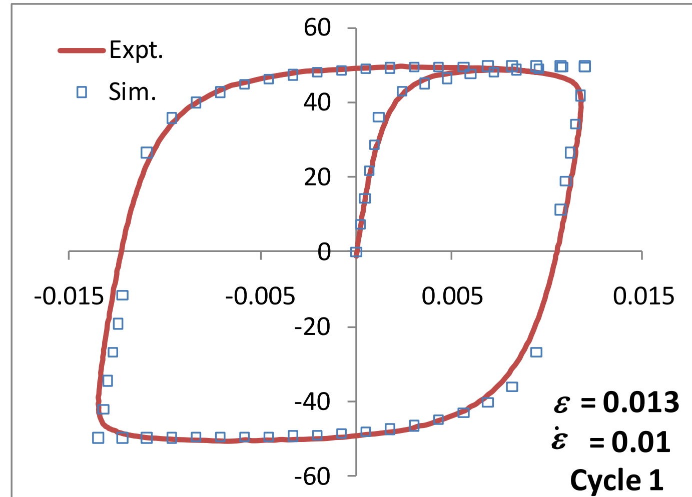

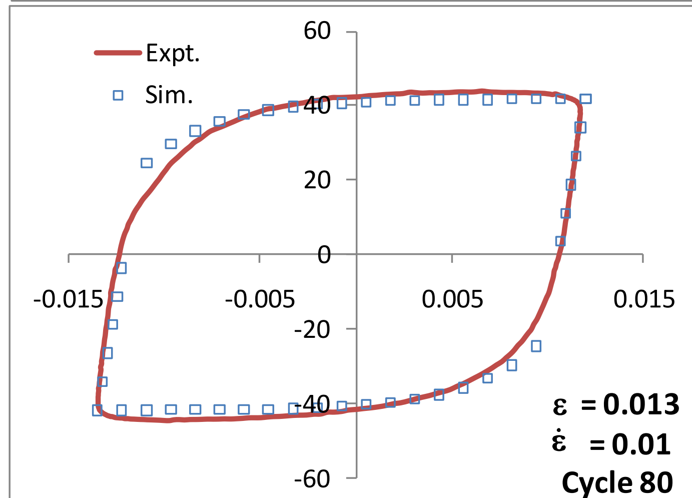

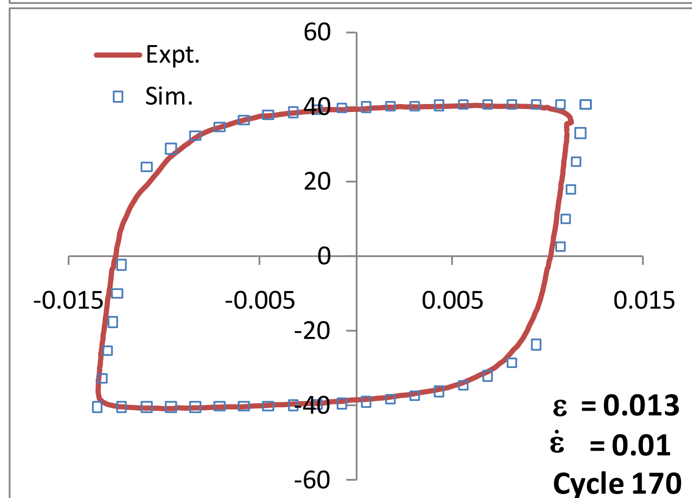

B.2.2 Medium strain amplitude and low strain rate

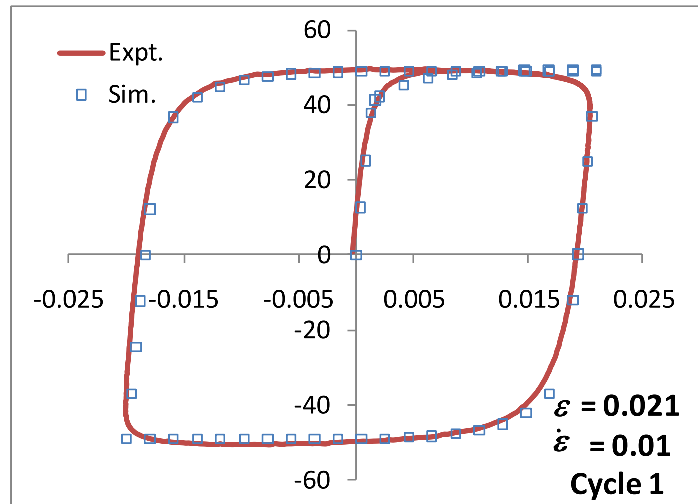

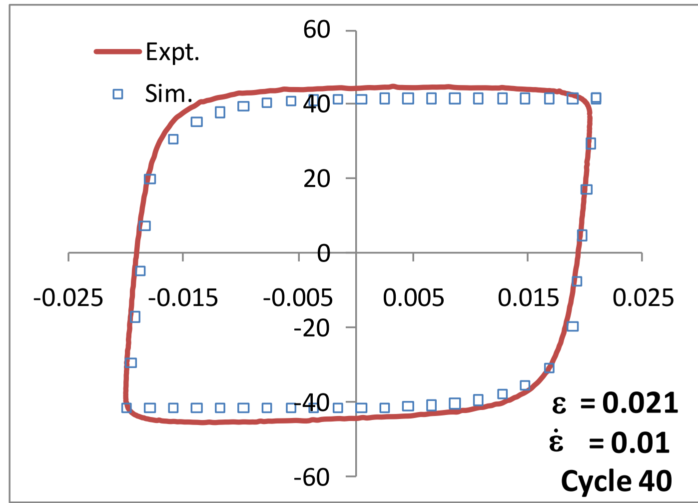

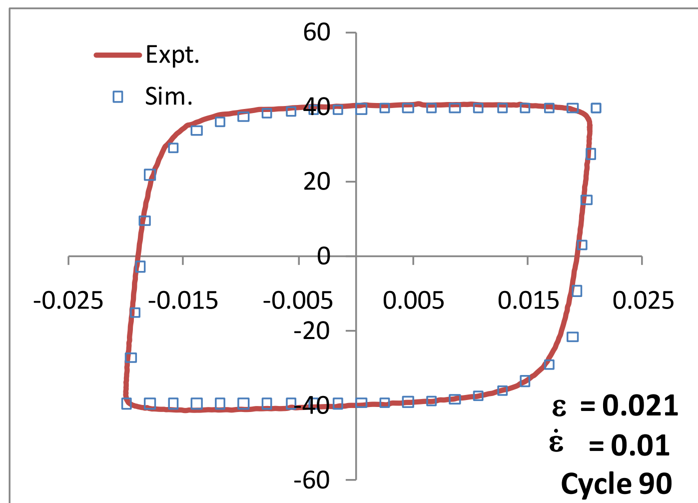

B.2.3 High strain amplitude and low strain rate

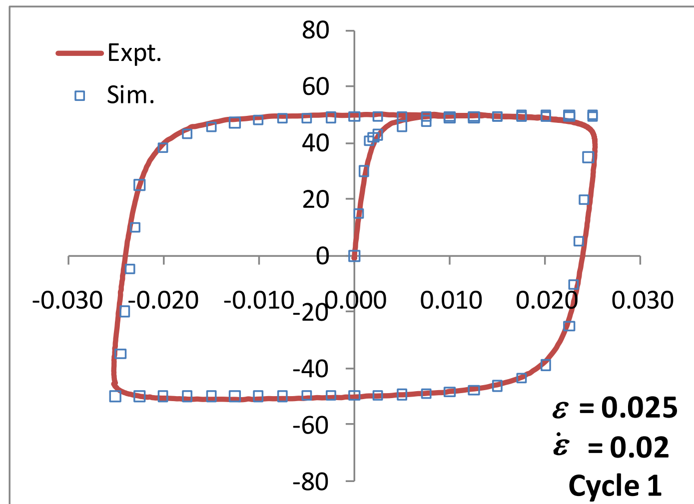

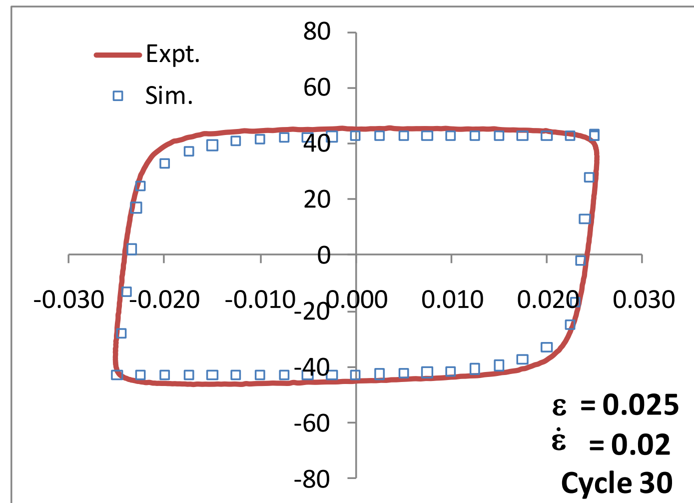

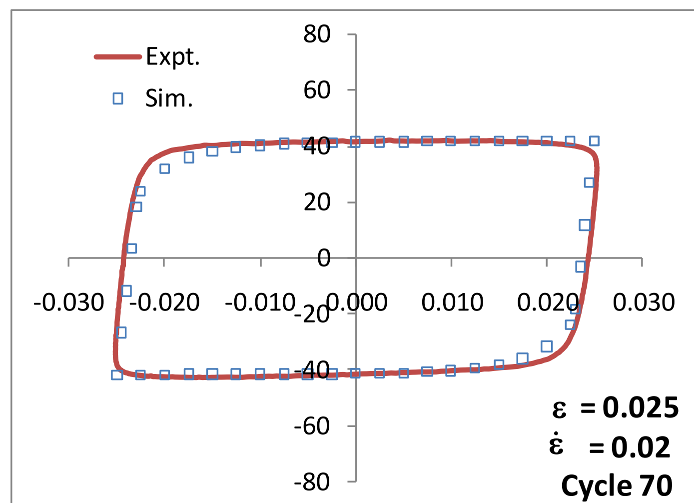

B.2.4 Low strain amplitude and high strain rate

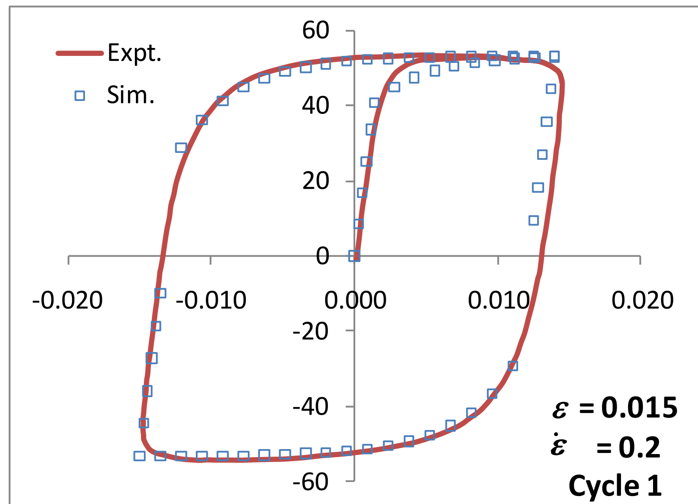

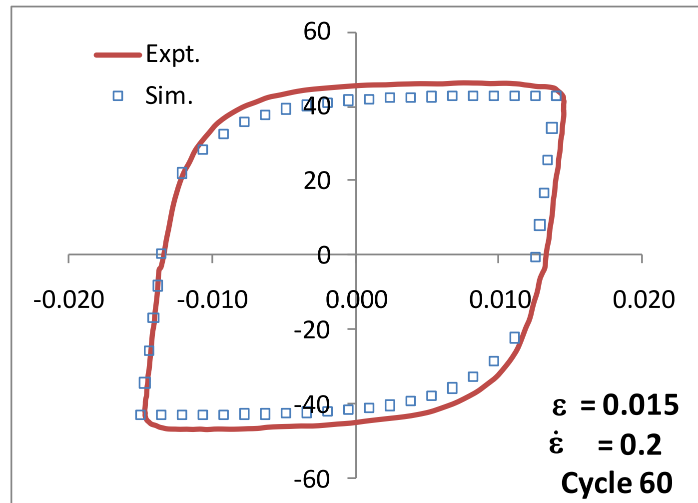

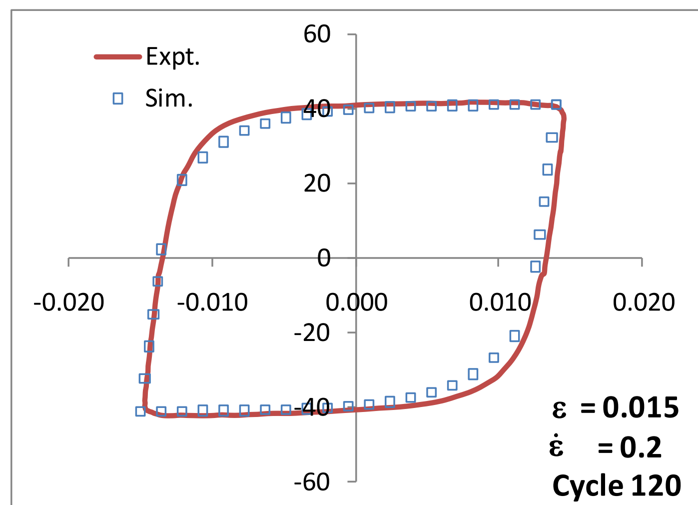

B.2.5 Medium strain amplitude and high strain rate

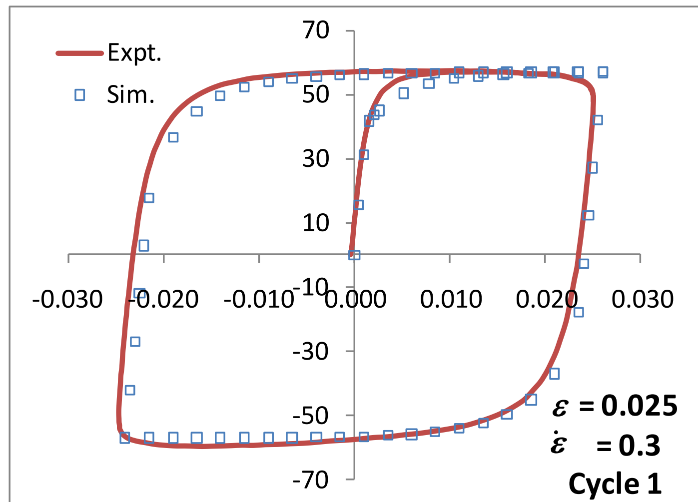

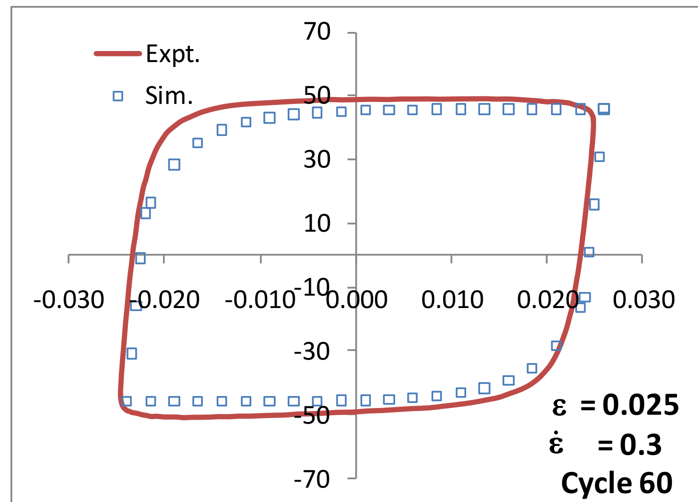

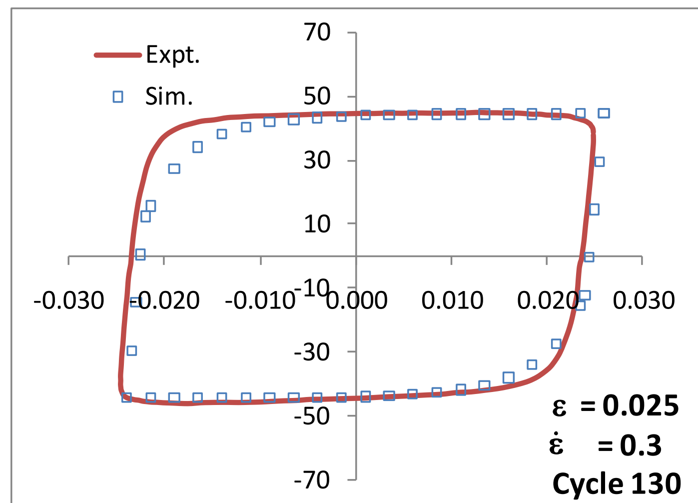

B.2.6 High strain amplitude and high strain rate

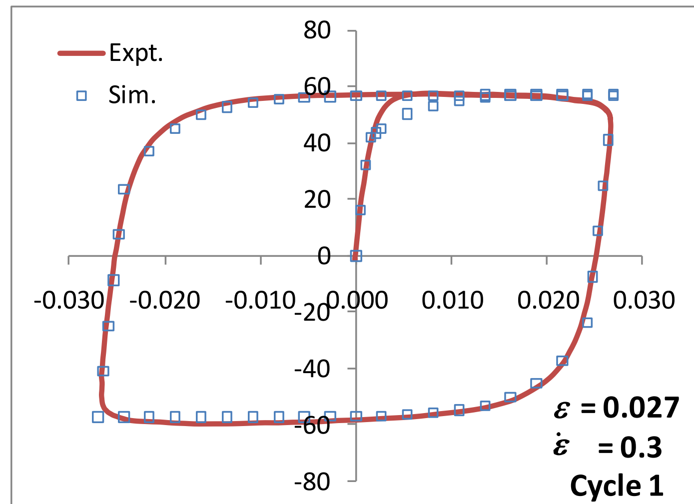

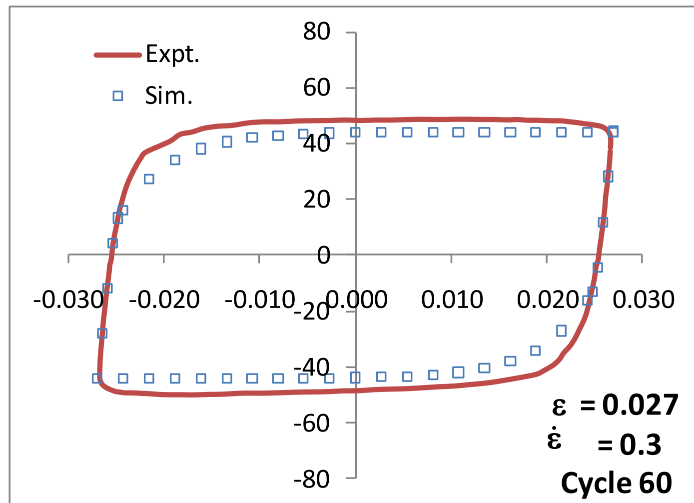

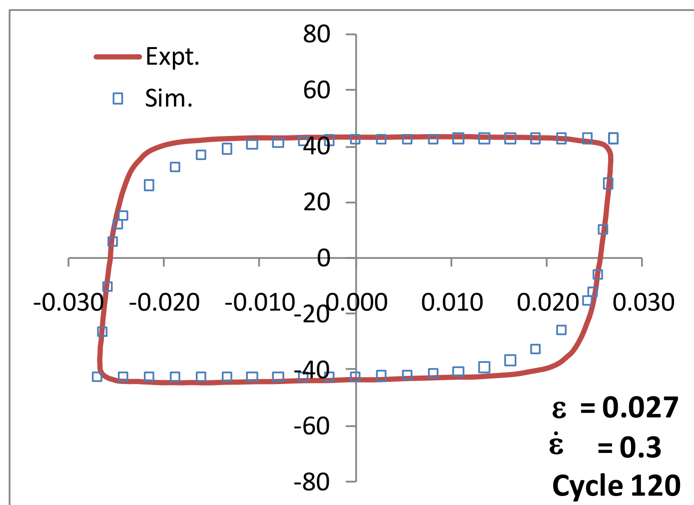

B.3 Sn100C Solder Alloy

B.3.1 Low strain amplitude and low strain rate

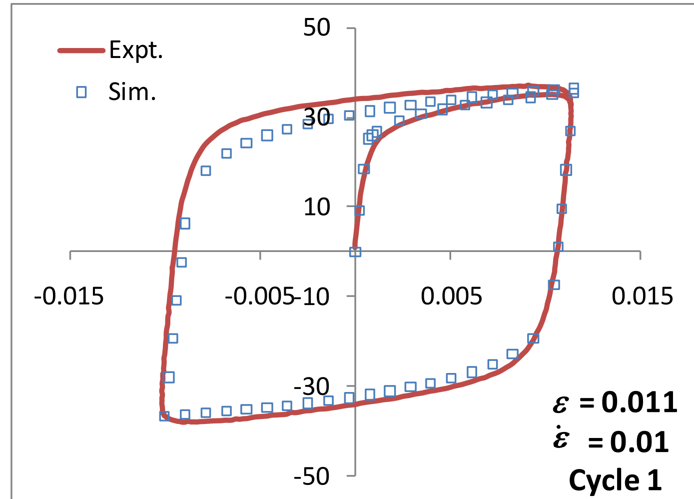

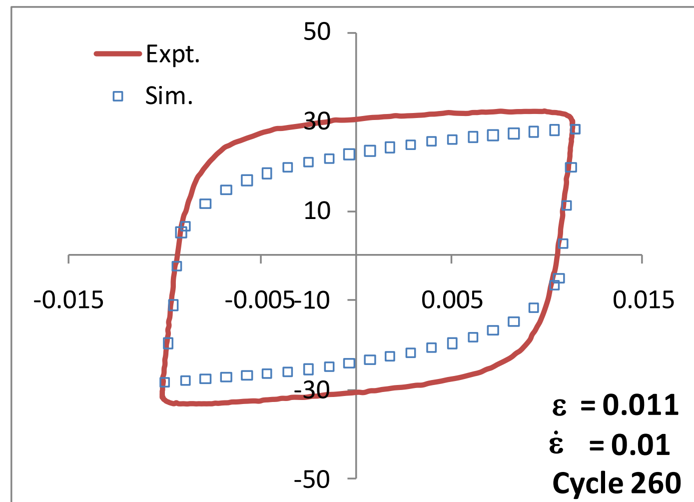

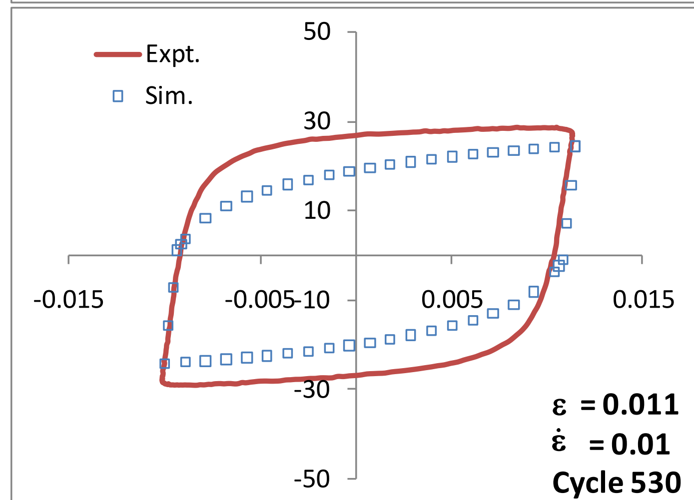

B.3.2 Medium strain amplitude and low strain rate

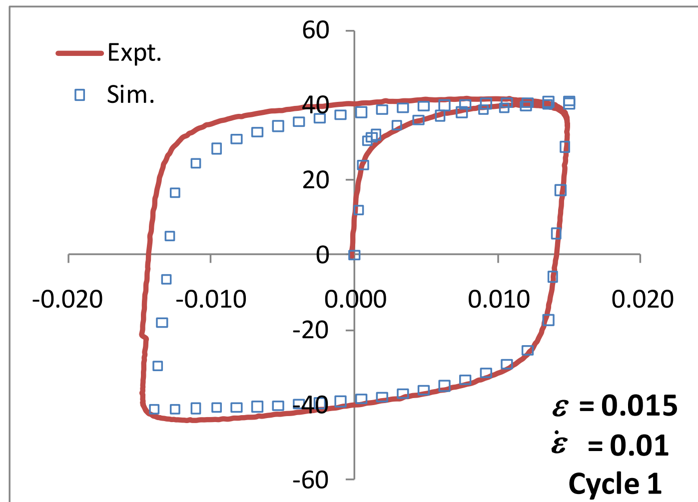

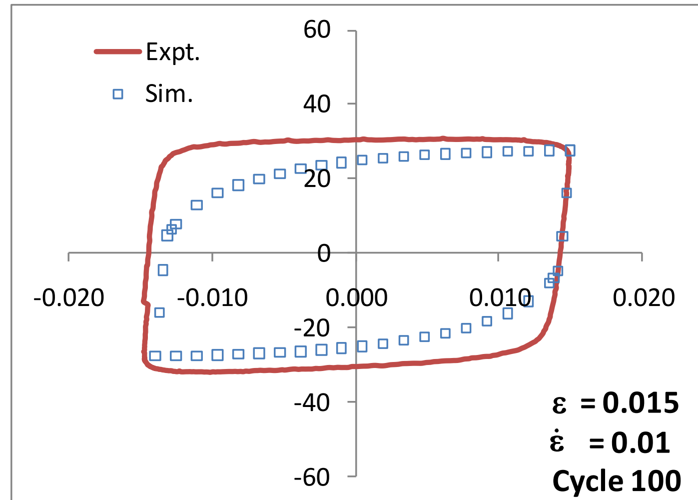

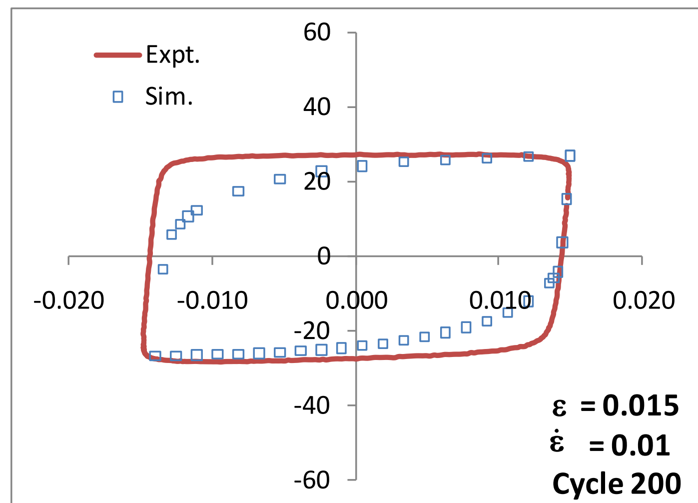

B.3.3 High strain amplitude and low strain rate

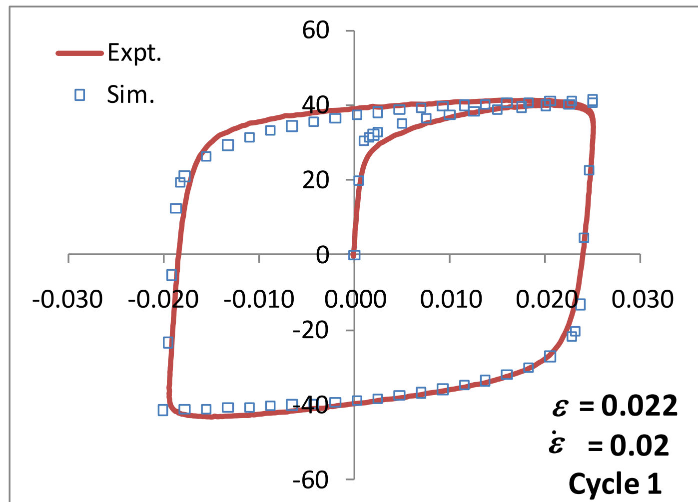

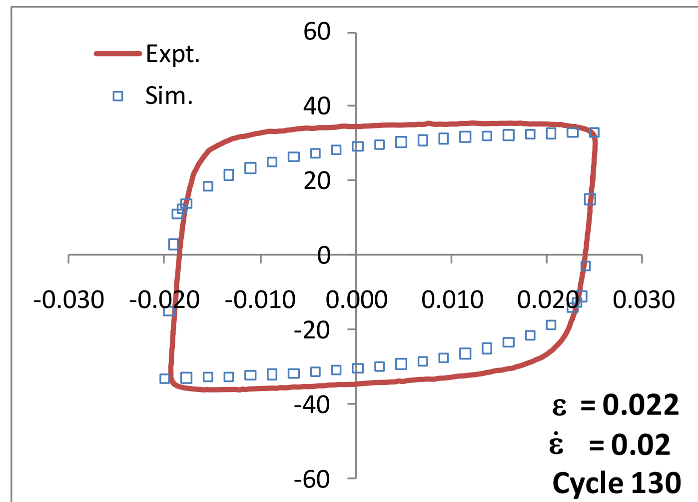

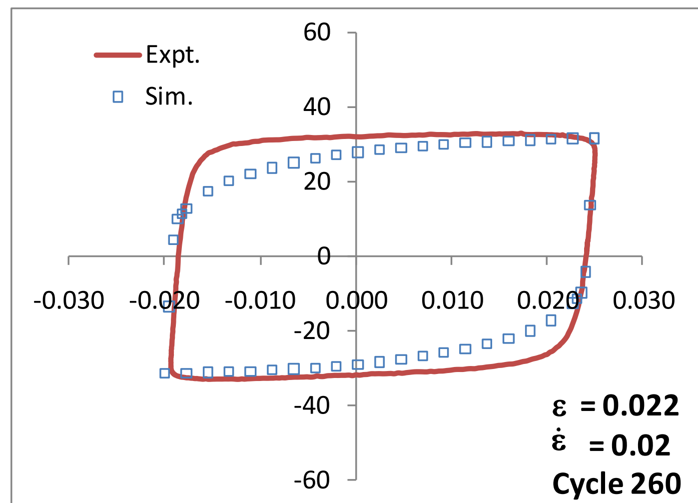

B.3.4 Low strain amplitude and high strain rate

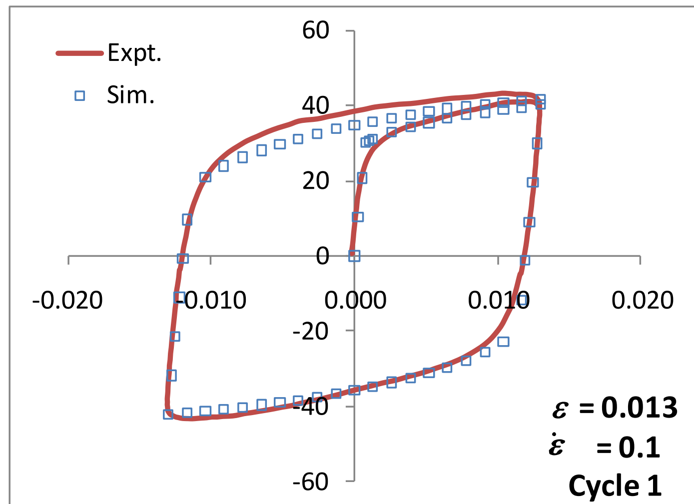

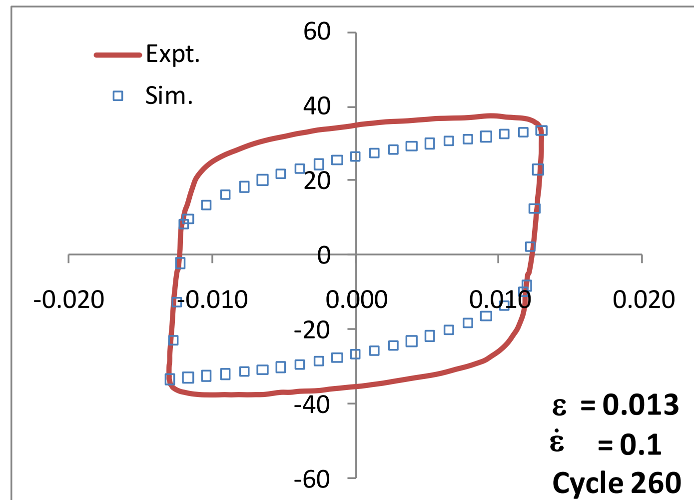

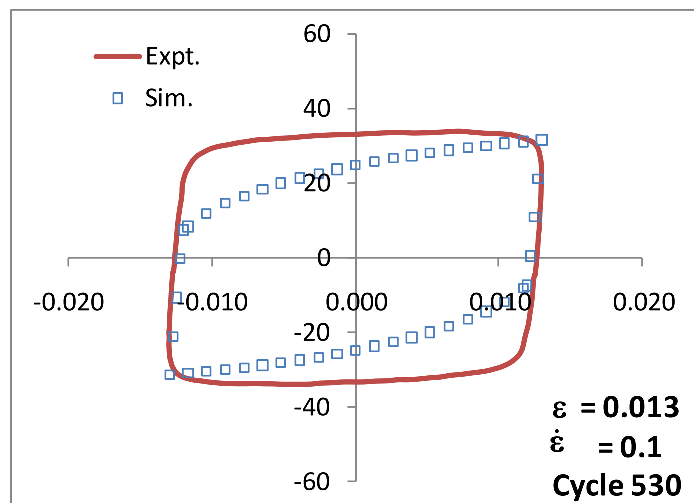

B.3.5 Medium strain amplitude and high strain rate

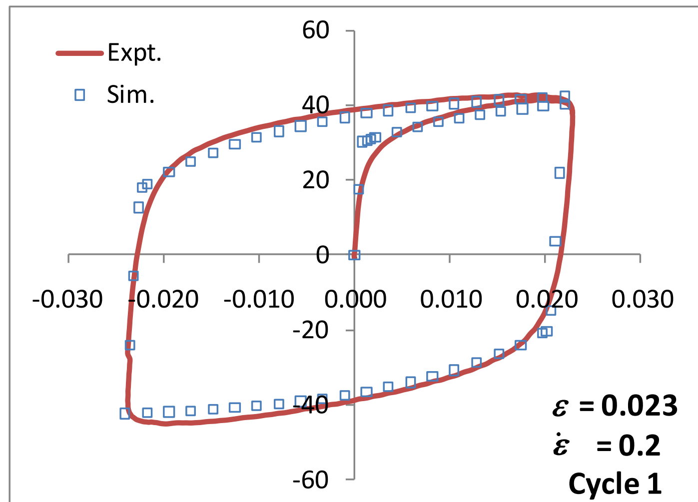

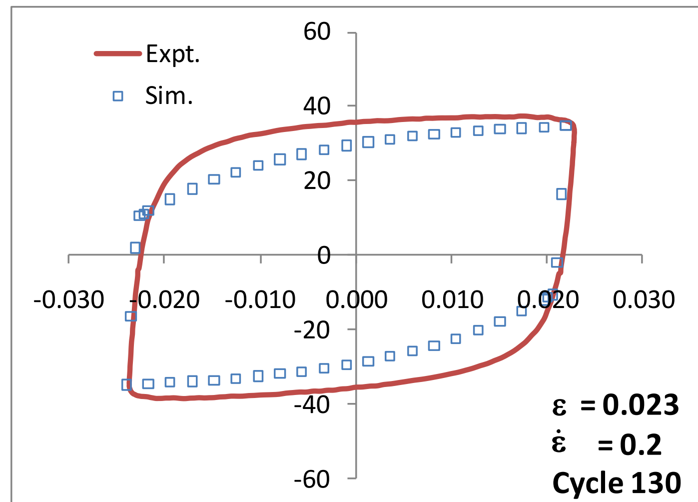

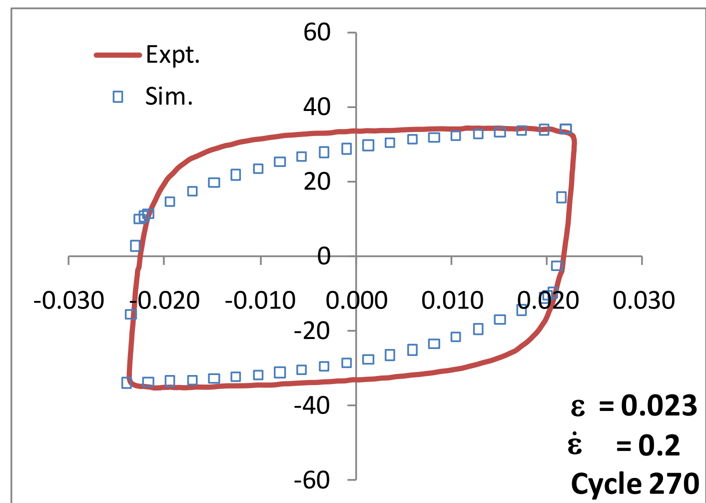

B.3.6 High strain amplitude and high strain rate